High-resolution record of primary productivity and anoxia in the context of the environmental history of Lago di Mezzano, Central Italy, since the Late Glacial

Master thesis
Faculty of Science, University of Bern

handed in by

Luc Hächler

2021

Supervisor

Prof. Dr. Martin Grosjean

Advisors

Dr. Paul Zander

Giorgia Beffa

UNIVERSITÄT BERN

OESCHGER CENTRE
CLIMATE CHANGE RESEARCH

Impressum

Title	High-resolution record of primary productivity and anoxia in the context of the environmental history of Lago di Mezzano, Central Italy, since the Late Glacial
Institution	University of Bern, Graduate School of Climate Sciences
Issue	Master thesis (60 ECTS)
Date	18 November 2021
Author	Luc Hächler, 15-109-812, luc.haechler@students.unibe.ch
Supervisor	Prof. Dr. Martin Grosjean, Oeschger Centre for Climate Change Research and Institute of Geography at University of Bern
Advisors	Dr. Paul Zander, Oeschger Centre for Climate Change Research and Institute of Geography at University of Bern Giorgia Beffa, Oeschger Centre for Climate Change Research and Institute of Plant Sciences at University of Bern
Pages	84
Cover image	Lago di Mezzano, own image (September 2021)
Code and data availability	Used code, data and a description thereof will be made available to the paleolimnology group (Prof. Dr. Martin Grosjean) and to PhD-student Giorgia Beffa (leader project Lago di Mezzano).

Acknowledgements

This thesis has evolved over one year and was only possible because of the support of numerous people. Here, I like to name some of them.

First, thanks to my supervisor Martin Grosjean; he suggested me to do a master in climate sciences and enabled me to gain valuable insights into state of the art, interdisciplinary, paleolimnological research. Thanks to my advisor Paul Zander for his invaluable methodological support. He introduced me to all relevant paleolimnological methods, from the sediment description to hyperspectral imaging and lab work. He helped me in data analysis and interpretation, and had always time for discussions. Many thanks to my advisor Giorgia Beffa. You made it possible that I could do my master thesis about wonderful Lago di Mezzano. I was always welcome at the Birrlihus in the Botanical Garden for valuable exchange on the project. We had many fruitful discussions and you showed me enthusiastic your work. We had a great collaboration and you willingly exchanged data and supported me in the interpretation. Together, we dived into the, to us new, scanning technologies of magnetic susceptibility, X-ray fluorescence (XRF) and micro-XRF (μXRF). I would like to thank the coring teams of the Institute of Plant Sciences (IPS) that retrieved the sediment cores in 2019 and 2020. Without the field work of Giorgia Beffa, Kathrin Ganz, Y. Hunziker, Peter Ruprecht, Carolina Senn, E. Tanner, Willi Tanner, and Yunuen Temoltzin Loranca this thesis would not be possible. Also, many thanks to the paleoecology group of the IPS for their continuous support. Especially to Kathrin Ganz and Lieveke van Vugt, they enabled me to join their field work in Greece and to getting to know everything around lake coring. I really enjoyed the fieldwork. Also, Kathrin introduced me to the processes of core opening and stratigraphic correlation. Thanks to Willy Tinner for his helpful inputs in discussions on excursions and in meetings. Next, thanks to Marina Morlock for scanning the 2019 cores and her help in data interpretation and analysis on these cores. Also, many thanks to Hendrik Vogel, Adrianus Damanik, Nicolas Tournier who introduced me to the ITRAX scanner. They explained me the XRF technique and supported the scanning and data interpretation in 2020 and 2021. Furthermore, I would like to thank Shauna Rainford, she introduced me to the μXRF scanning and left me and Giorgia a lot of freedom to explore the capabilities of that new machine. Thanks to Sönke Szidat for providing age dates and answering questions on Pb-210 modelling. Numerous people supported my thesis by providing essential data. I would like to thank Christoph Schwörer for the chironomid data on summer temperature, Gianni Zanchetta for the stalagmite data on humidity, Julieta Massaferro for her pigment data, and Norbert Nowaczyk and Achim Brauer for providing data on the magnetic susceptibility of the 1995 sediment core. I would like to thank the paleolimnology group for their fruitful inputs and discussions in our numerous meetings. A special thanks to Daniela Fischer and Giulia Wienhues for helping me in the lab an explaining me many things about pigments.

A big thanks to everyone from the master pool room 003 for the supporting work atmosphere. To them, my fellow students, and friends I would like to express my gratitude for the many good discussions during coffee breaks and lunches. In addition, I would like to thank Chantal Hari, Malve Heinz, and Simone Schönenberger for their proof reading, their flexibility, the critical questioning of my thesis, and their valuable support even from a safari in South Africa. Finally, a big thanks to my parents Monika Piehl and Beat Hächler, without their support this work would not have been possible. A big thanks to my twin brother Pascal for his support and especially for cooking delicious food after a dense writing day. In gratitude for the support of all involved people and to highlight the collaborative effort behind this thesis I will use the "we" pronoun throughout my thesis.

18 November 2021, Bern.

Abstract

Current anthropogenic climate change is influencing nature and human societies around the earth. Global warming and direct anthropogenic impacts are now harming lake ecosystems worldwide. A majority of projected (RCP 6.0) lake mixing regime changes will alter lakes from warm monomictic (only mixing in winter) to meromictic (permanent stratification). This puts additional pressure on freshwater ecosystems in the Mediterranean. However, little is known about how lake mixing changed prior to anthropogenic impact. We used, for the first time in the Mediterranean, a high-resolution series of calibrated pigment concentrations based on recently developed hyperspectral imaging (HSI) to provide long-term sub-decadal data on lake stratification and primary productivity. Based on warm-monomictic Lago di Mezzano (Central Italy), we could show that lake mixing and primary productivity were highly variable over the past 18,000 years. Using X-ray fluorescence (XRF) elemental proxies and palynological investigations we related primary productivity and anoxia changes to the catchment's environmental history (erosion, land cover, vegetation changes, fire dynamics, and anthropogenic impact). A comparison with independent climate proxy data on temperature and humidity revealed a tendency to meromixis and high productivity at higher temperatures, supporting model results. We showed that high lake level stands of the highly variable Lago di Mezzano led to low lake productivity and increased mixing behaviour thanks to the lake's special maar morphology. We found that, since the early Neolithic, periodic human induced forest openings promoted lake mixing and a cease of anoxia because of higher wind shear. These oxic conditions favoured sedimentary nutrient trapping and reduced the lake productivity whereas closed forest stands increased anoxia and nutrient recycling. Thus, a present day return to a forested natural state might lead to lake stratification. We therefore highlight that landscape management has an important role in how lake ecosystems react in ongoing climate change.

Keywords:
climate change, warm-monomictic lake, anoxia, lake primary productivity, hyperspectral imaging, X-ray fluorescence, Late Glacial, Holocene

Table of content

List of figures

Appendix

List of tables

Appendix

List of abbreviations

BCE	Before the Common Era
BiM	Biogenic matter
BiO	Biogenic SiO_2
Bphe	Bacteriopheophytin *a* and *b*
CE	Common Era
CONISS	Stratigraphically constrained hierarchical cluster analysis by the method of incremental sum of squares
DD	Dry density
GIUB	Institute of Geography, University of Bern
HI	Hydrogen index
IPS	Institute of Plant Sciences, University of Bern
LOI	Loss-on-ignition at 550°C
MAR	Mass accumulation rate
MAR	Mass accumulation rate
MiM	Total minerogenic matter
MS	Magnetic susceptibility
OI	Oxygen index
PCA	Principal component analysis
RABD	Relative absorption band depths
RDA	Redundancy analysis
SR	Sedimentation rate
TC	Total carotenoids
TChl	Chlorophyll *a* and *b* and diagenetic products
TIC	Total inorganic carbon
TOC	Total organic carbon
XRF	X-ray fluorescence
years BP	Calibrated years before present (before 1950)
µXRF	Micro X-ray fluorescence

1 Introduction

1.1 General problem

Anthropogenic impact is seen as the main cause for current climate change, which is affecting the environment and human societies around the globe (IPCC, 2014). Climate change and direct human impacts are now harming freshwater ecosystems globally, especially from high nutrient loads (Jenny et al., 2016; Woolway et al., 2020). Lakes respond in various ways, including eutrophication and associated algal blooms (Lee et al., 2016), enhanced chemical and thermal stratification (Boehrer & Schultze, 2008), alteration of mixing regimes (Woolway & Merchant, 2019), hypoxia (Jenny et al., 2016), and fish kills (Sayer et al., 2016). This threatens the biodiversity in and around lakes, and also the ecosystem services they provide (Abell et al., 2008; Mills et al., 2017; Rinke et al., 2019).

Observational data have revealed the current state of freshwater ecosystems in great detail (Mills et al., 2017). That gives researchers a better understanding of the now extensively studied biogeochemical cycle (Gulati et al., 2017; Lerman, 1978; Lerman et al., 1995; Wetzel, 2001). However, most observational data cover the short-term, and span no more than the last century (Mills et al., 2017). This is insufficient data coverage to address the challenges ahead, e.g. via lake restoration or management. For future management to be effective, long-term data are needed to give an insight into anthropogenic impacts prior to the current time period. Such data would help researchers to assess pre-disturbance conditions, disentangle the influence of natural variability and human pressure, predict possible reactions in the future, and clarify the achievability and consequences of different lake management plans. Furthermore, such data may aid experts to place current lake ecosystem degradation into a wider context (Bennion et al., 2011; Friedrich et al., 2014; Mills et al., 2017).

Without long-term observational data available (Friedrich et al., 2014), a paleolimnological approach using proxy data can provide valuable information instead (Bennion et al., 2011; Dearing, 2013; Mills et al., 2017). A variety of conventional methods has been used to reconstruct past changes; however, most of them are time-consuming and costly (Rothwell & Croudace, 2015; Zander et al., 2021). This shortage of effective methods limits our understanding of past lake productivity and anoxia at sub-decadal resolution on multi-millennial scales spanning the Holocene (Makri et al., 2021b). Recently, Butz et al. (2015) made advances with hyperspectral imaging (HSI), a rapid, non-destructive scanning technique with sub-mm resolution. Their newly developed method uses spectral indices based on the spectral signature of sedimentary pigments. Thanks to proxy-proxy calibration, HSI enables the quantitative reconstruction of bacteriopheophytin *a* and *b* (Bphe) and total chloropigments (chlorophylls and diagenetic products, TChl) in lake sediments. These pigment groups were used as proxies for anoxia and lake production. Thanks to the high spatial resolution, this new method offers insights even into seasonal variations in varved sediments (Butz et al., 2015, 2016, 2017). Since then, the method has been applied in multiple case-studies to Holocene-long records in temperate, dimitic lakes.

State-of-the-art, multi-proxy, Holocene-long quantitative reconstructions of sedimentary pigments provided unprecedented insights into the complex effect that human pressure and natural variability have on anoxia and lake production (Makri et al., 2020; Sanchini et al., 2020; Zander et al., 2021). However, in the Mediterranean area, little is known about sub-decadal variations of anoxia and lake productivity over the Holocene. Two recent multi-proxy studies with a focus on vegetation dynamics used the uncalibrated spectral indices as a proxy for the sedimentary pigments mentioned above. Gassner et al. (2020) studied the shallow and eutrophic Limni Zazari in northern Greece, which is polymictic (Kagalou & Leonardos, 2009). A second study investigated the shallow, brackish, and eutrophic Lago di Baratz in Sardinia, with its specific island climate (Pedrotta et al., 2021).

As these recent studies provide only uncalibrated, semi-quantitative data, there is a lack of quantitative reconstructions of sedimentary pigments in the Mediterranean area. Also, there is a paucity of knowledge about sub-decadal oscillations of anoxia and primary productivity in warm-monomictic lakes, specifically over the Holocene. Such long-term data are needed to improve short-term perspectives on observational data. This is especially relevant, as most of the lakes projected to undergo a change in mixing regime (under RCP 6.0) transform from warm-monomictic, only mixing in winter; to meromictic, with permanent stratification (Woolway & Merchant, 2019).

1.2 Research motivation, questions, and study design

1.2.1 Motivation

This master thesis project provides a holistic, multi-proxy environmental reconstruction of Lago di Mezzano since the Late Glacial on sub-decadal scale. The aim of the thesis is to overcome the paucity of reliable long-term data on primary productivity and anoxia on warm-monomictic lakes in the Mediterranean. We present, for the first time in the Mediterranean, a sub-decadal record of calibrated pigment concentrations (TChl and Bphe) based on hyperspectral imaging (HSI) since the Late Glacial. This allows us to reconstruct the evolution of in-lake primary productivity and anoxia in great detail. Furthermore, we aim to disentangle influences from either natural variability or human pressure on primary productivity and anoxia by linking these in-lake processes to the catchment's environmental history and postglacial climate change. Hence, this work will lead to a better understanding of relevant processes at work in a present day warm-monomictic lake. These freshwater ecosystems are threatened by anthropogenic climate change. Therefore, our study may guide the development of sound restoration and management strategies for similar lakes, ultimately helping to save these ecosystems.

Furthermore, the present master thesis supports the project of PhD-student Giorgia Beffa at the University of Bern's Institute of Plant Science (IPS), who is doing her thesis on Lago di Mezzano. She investigates the paleoecology in the Neolithic and Iron Age (changed from the Bronze Age) with very high chronological precision (10 - 20 years) and resolution (5 mm or 5 - 10 years). This enables her to study the effects of fire, land use, and abrupt climate changes on vegetation communities. Also, it allows her to access synchronicity of anthropogenic land use phases in central and southern Europe and to test competing land use and climate impact hypotheses. Her work is part of the ECSE project (Exploring Prehistoric Vegetation and Agriculture Dynamics Using Annually Laminated Records from Central and Southern Europe), funded by the Swiss National Science Foundation (project number: 182084).

1.2.2 Research questions

To guide our research, we addressed the following research questions based on the example of Lago di Mezzano:

- How has lake productivity (trophic state) and anoxia developed since the Late Glacial? In the varved sections, can we distinguish between seasonal anoxia and (multi)decadal meromixis?
- How does the lake's postglacial history of productivity and anoxia relate to the environmental history (erosion, hydrology, land cover, vegetation changes, fire dynamics and anthropogenic impact) and postglacial climate change (temperature and humidity)?

1.2.3 Hypotheses

The following hypotheses frame the expected results.

- Higher lake productivity (trophic state) is expected during warmer times.
- HSI-inferred TChl is an indicator for lake productivity and shows seasonal algae blooms in varved sections.
- The XRF-(Fe/Ti)/Mn ratio is a good redox proxy and shows anoxic conditions.
- The HSI-R850/R900 spectral ratio is a good clastic input indicator.
- HSI-inferred Bphe allows to distinguish seasonal anoxia and (multi)decadal meromixis in varved sections.
- Anoxia is expected at high lake levels or/and closed forest stands because of reduced mixing
- Decreasing human pressure can be observed at around 800 CE, which coincides with higher lake levels as indicated by increased *Alnus* (Sadori, 2018).

1.2.4 Study design

To answer the research questions, we used a paleolimnological approach (Smol, 2008) based on proxy data. Our analysis is mainly based on non-destructive, high-resolution scans of lake sediments derived from Lago di Mezzano in the years 2019 and 2020 (see Fig. 1). To reconstruct the evolution of primary productivity and anoxia we used the sedimentary pigments TChl and Bphe as a proxy. These pigments have a specific spectral fingerprint in the sediment. We inferred their concentration from calibrated hyperspectral indices using hyperspectral imaging (HSI) scans with ~83 μm spatial resolution, a method similar to the one developed by Butz et al. (2015). To disentangle influences from either natural variability or human pressure, we related our data on lake productivity and anoxia to the lake catchment's environmental history and postglacial climate change. Information on the environmental history (erosion, land cover, vegetation changes, fire dynamics and anthropogenic impact) was derived from X-ray fluorescence (XRF) elemental proxies and palynological investigations. A lower resolution palynological overview was taken from Sadori (2018) whereas high-resolution data on the Neolithic was counted by Giorgia Beffa (unpublished data). These palynological data sets will get published. The scanning data obtained here were validated with conventional geochemical analysis done by researchers two decades ago (Brandt et al., 1999; Ramrath et al., 1999a, 1999b, 2000; Wilkes et al., 1999). Their results were tied to our master core by correlating high-resolution (5 mm) magnetic susceptibility records. The effect of climate variability was assessed using independent climate proxy data on temperature and humidity (Regattieri et al., 2014; Samartin et al., 2012; 2016; 2017). This linkage was possible thanks to our new high-precision chronology based on Cs-137, C-14, and tephra age dates. In addition, we established for the laminated Bronze Age case-study section an ultra-high-resolution record based on HSI (25 μm resolution) and μXRF (50 μm resolution). This helped us to verify the presence of varves, assess their preservation and detect seasonal variations in the proxy data.

2 Study site

Lago di Mezzano (42°36'42" N, 11°46'12" E, 452 m a.s.l.) is a small and deep maar lake in central Italy. The volcanic lake is situated in northern Latium, ~100 km north-west of Rome, about 30 km away from the Tyrrhenian Sea, and lies eccentrically in the Caldera di Latera (see Fig. 1). The 31-m-deep lake has an area of 0.5 km^2 and is mainly fed by precipitation and groundwater. Some very small and short inflows originate on the steep slopes in the south-west of the catchment (1 km^2). The water discharges over an artificially regulated man-made outlet (Fosso delle Volpi) into the Olpeta river, which in turn leaves the caldera at the deepest point of the crater ridge in the north-east. Today, this outlet limits lake level fluctuations to about half a meter (Ramrath, et al., 1999a; Sadori, 2018).

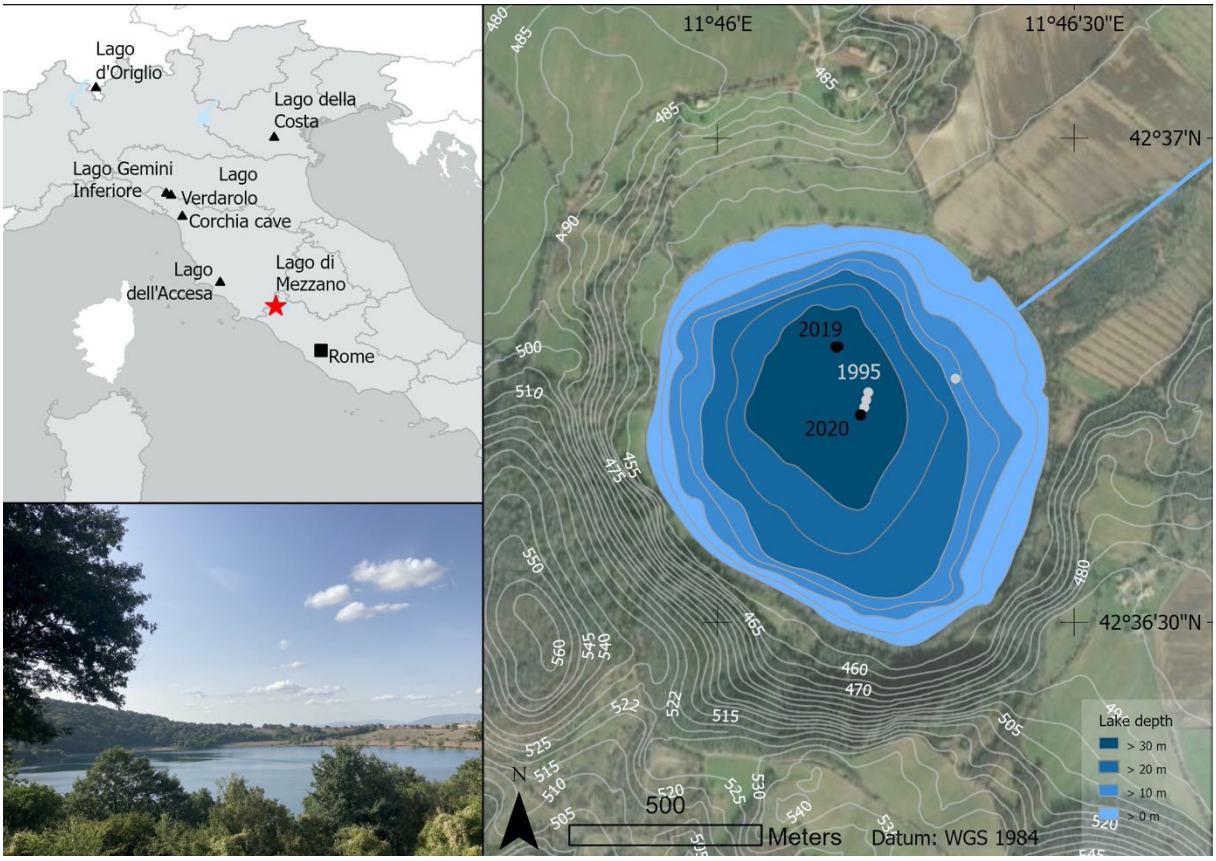

Fig. 1: Map of Lago di Mezzano. Upper left panel: Overview with location of Lago di Mezzano (red star) and sites of climate data (back triangle). Administrative areas from GADM (gadm.org). Lower left panel: image of Lago di Mezzano (view from south-east shore, picture taken in September 2021). Right panel: Lake with 1995 (Ramrath, 1997), 2019, and 2020 coring sites. The position of a surface core taken in 1991 (Massaferro, 1994) is not known. Water depths are from Ramrath (1997), satellite image from ESRI, and contour lines from Latium's geoportal (geoportale.regione.lazio.it).

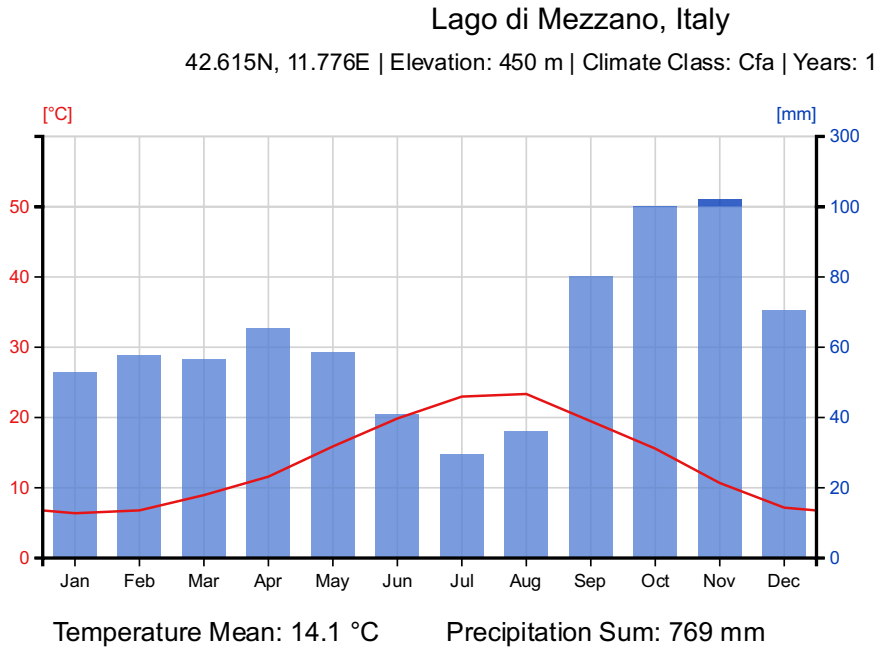

Month	Temp	Precip
Jan	6.4	52.9
Feb	6.8	57.7
Mar	9.0	56.6
Apr	11.6	65.2
May	15.9	58.5
Jun	19.9	40.9
Jul	23.0	29.6
Aug	23.3	35.9
Sep	19.5	80.2
Oct	15.6	100.0
Nov	10.7	121.0
Dec	7.2	70.4

Fig. 2: Climate diagram of Lago di Mezzano based on the CHCN, CAMS and CPCC v2018 model described in Fan & van den Dool (2008). The reference period is 1987-2016. Graph from ClimateCharts.net (Zepner et al., 2021).

The lake is mesotrophic to oligotrophic (moderate to low primary productivity) and warm-monomictic (only mixing in winter) (Ramrath, 1997; Ramrath et al., 2000). Spring diatom blooms end before May and take up all available nutrients. At this time the chemocline is between 15 and 20 m deep; this depth is expected to shrink in summer with an expansion of the hypolimnion. Prior to land reclamation works in 19th century, the larger lake (1.36 km^2) was fed by inflows coming from the entire Caldera di Latera (3.57 km^2). In a geomorphological study, Giraudi (2004) revealed that there were much larger lake level variations in the past changing the lake several times from endorheic (closed lake with no outflow) to exorheic (open lake with an outflow) during the past millennia (see Fig. 20). These changes followed the hydrological balance of the lake. At periods with sufficient water supply the lake was exorheic and discharged over the depression in the crater ridge. In phases with a lower water supply the lake was endorheic and the lake level changed to meet the water balance (Giraudi, 2004).

Lago di Mezzano formed during a phreatomagmatic eruption around 100,000 years ago (Metzeltin & Vezzoli, 1983; Nappi et al., 1995). The bedrock is of volcanic origin and dominated by olivine latites and trachy-andesites (Brai et al., 1979; Pichler, 1989). A strong precipitation gradient from the Apennine to the Tyrrhenian sea defines the climate of the region (Sadori, 2018). Model results (Fan & van den Dool, 2008; Zepner et al., 2021) show that Lago di Mezzano has a mean annual precipitation of 769 mm (1987-2016 CE), falling mainly in autumn and early winter. Mean annual temperature is 14.1°C while mean July and January temperatures are 23°C and 6.4°C (Fig. 2).

Lago di Mezzano is framed by a rural landscape with cereal crop cultivation and pastureland. The few deciduous mixed oak forests in the catchment are dominated by *Quercus cerris* with *Quercus pubescens*, *Acer campestris*, *Carpinus betulus*, *Ostrya carpinifolia*, *Fraxinus ornus*, *Fagus sylvatica* and *Castanea sativa*. Along the lake shore the vegetation is dominated by *Alnus glutinosa, Populus alba*, and *Salix* species.

While human presence since the Palaeolithic age has been documented (Conti et al., 1993; Petitti & Rossi, 2012), rich archaeological data indicate significant human activity since the Bronze Age (time period according to Stoddart et al., 2019). Pile dwellings and many bronze axes suggest that the lake shore was inhabited from 3700 - 3300 years BP (years before 1950). After a short abandonment, probably due to higher lake levels, a second phase of human occupation is documented at around 3000 years BP. However, this time findings suggest a perilacustrine settlement which was used for cultural purposes (Conti et al., 1993; Pellegrini, 1993; Petitti, 2000; Petitti & Mitchell, 1993; Sadori et al., 2004). Next, around 2500 years BP, Etruscans settled in the area which is evidenced by historical and archaeological data. In the third century BCE, Roman lake regulation started and transformed the catchment (Ramrath et al., 2000; Sadori, 2018). At 900 CE the fortified village Mezzano was founded. It lasted until 1348 CE (Luzi, 1990; Sadori, 2018). In the eighteenth century and during the beginning of the twentieth century reclamation works led to a lowering of the lake level to today's 452 m a.s.l. (Giraudi, 2004; Ramrath et al., 2000).

The past environmental history of Lago di Mezzano was extensively studied for the last 34,000 years. The sediment from 30-m-long cores retrieved in 1995 (Fig. 1) has been examined and its geochemical properties described using a variety of conventional methods. Furthermore, diatoms, pollen, and charcoal were counted on these cores (Brandt et al., 1999; Ramrath et al., 1999a, 1999b, 2000; Sadori, 2018; Sadori et al., 2004; Wilkes et al., 1999). Also, an 80-cm-long surface core from 1991 was analysed for pigments (Massaferro, 1994). And finally, a geomorphological study investigated lake level changes for the past 23,000 years (Giraudi, 2004). However, there are several limitations involved. The studies on the 1995 sediment cores all rely on a chronology established by Ramrath et al. (1999a). Ramrath et al. used AMS radiocarbon dates obtained from the bulk sediment, making them susceptible to reservoir effects (Philippsen, 2013). Hence, Sadori et al. (2004) suggested an offset of 100-200 years (too old) for varved sections constrained by a varve-based floating chronology. However, in the sections with no varves, dates are probably even less

reliable, or just indicative, making comparison with other sites problematic. Another limitation is that most proxies only have centennial scale resolution. This makes short-term sub-decadal scale events hard to constrain. However, with our more precise chronology, this wealth of data is very valuable to validate our high-resolution scanning data. Hence, Lago di Mezzano is a perfect study site to explore the possibilities of high-resolution scanning techniques such as HSI and XRF. Details about the data used from past research are presented in the data chapter.

3 Material and methods

3.1 Sediment cores

In two campaigns in 2019 and 2020, long and surface cores were retrieved from the deepest point and the centre of Lago di Mezzano (Fig. 1, Table A 1). A Niederreiter piston corer was used to get the long cores (ø 6 cm and 9 cm), whereas the surface cores (ø 6 cm) were retrieved by using a UWITEC short corer. Parallel cores were split into two halves and stratigraphically correlated to a 12-m-long master core using XRF data (5 and 0.2 mm resolution). The stratigraphy was validated by lithological marker horizons as well as HSI and MS logs. Table A 2 shows the stratigraphic correlation with the core depth and the master depth of each core used in the master core. The core depth is defined for each core section with zero depth at the beginning of the sediment at the time of the XRF scan. Zero depth of the entire master core is defined at the beginning of the surface core sediment at the time of the XRF scan.

For the Bronze Age case-study section, we extracted thirteen 18-cm-long U-channels from the core halves. These fresh sediment blocks (framed by an aluminium U-channel) were first measured by HSI and μXRF (three line-scans – 25 μm). We then embedded these blocks in resin. These resin blocks were polished and hence, they are no longer in the U-channel. We scanned the resin blocks again with μXRF (2 mm wide map scan – 50 μm) and stratigraphically corelated them using that data. Depths for each block are given in the block depth. This depth was then translated to the core depth and the master depth which allows the aggregation of the individual datasets. The beginning of the block depth is defined as the start of the resin blocks. For the fresh blocks this is different because they are shorter than the resin blocks. Therefore, the zero depth of the fresh blocks was defined as the inner end of Al frame of the U-Channel. Next, we had to stratigraphically correlate the fresh blocks to the resin blocks. We followed a simplified approach to do this and centred the fresh blocks on the resin blocks.

This simplified approach could be improved by searching for marker horizons in the μXRF data. Using these marker horizons, the μXRF data of the fresh blocks and the resin blocks could be combined. However, such a stratigraphic correlation presents two main challenges. First, the μXRF line scan data on the fresh blocks is just available as percentages and not as absolute counts. Hence, averaging of the line-scans per block to reduce noise is not possible as the percentages of each line-scan refer to different absolute values. Second, the resin embedding led to the formation of cracks which changed the sediment structure. An approach to correlate the two block types using dynamical time warping in R (dtw package v. 1.22-3; Giorgino, 2009) was not satisfying. Therefore, we assumed that the polishing of the resin blocks removed the same amount of material on both sides of the block. Table A 3 shows the stratigraphic correlation of the U-channels with a distinction between resin blocks (μXRF) and fresh blocks (with μXRF and HSI). Details on the μXRF method can be found in the methods chapter.

3.2 Methods

3.2.1 Chronology

The chronology is based on Cs-137 chronological markers, C-14 dates, and tephra layers. This preliminary chronology is solely used for this master thesis. The final chronology will be done by Giorga Beffa and improved with even more dates.

Cs-137, Pb-210, Ra-226 and Am-241 activities were measured at the University of Bern's Department of Chemistry and Biochemistry using gamma spectrometry. For this purpose, we sampled continuous 1.5 cm slices from the surface core (MZZ Sur W 2019, see Table A 2) to a depth of 60 cm. The 40 freeze dried samples (4-10 g $_{\text{dry weight}}$) were packed into polystyrene petri dishes (68 mm O.D., 11 mm height) together with a polystyrene disk of a fitting height to replace most of the air above the sediment. After four weeks, an equilibrium between total Pb-210 and in situ Ra-226 was assumed. Only the first 21 samples were measured because of too high background radiation values resulting from the catchment geology of Lago di Mezzano. We estimated the unsupported Pb-210 activity by subtracting the Ra-226 activity from the total Pb-210 activity level by level. This removed the effect of background radiation coming from the sediment (supported Pb-210). To calculate calendar years we used a constrained constant-rate-of-supply (CRS) model (Appleby, 2001). We constrained our model with the chronological marker (Cs-137 and Am-241) of the peak fallout from nuclear weapons testing in CE 1963. For validation we used the Chernobyl incident (CE 1986) chronological marker. Furthermore, we corrected for the missing inventory effect (Binford, 1990; Tylmann et al., 2014). To calculate the missing inventory, we established an exponential regression of the cumulative dry mass and unsupported Pb-210 activities based on all measured samples (n=21). That missing inventory of unsupported Pb-210 is defined mathematically as the fitted value on the calculated exponential regression for the deepest cumulative dry mass value. The age dates from the CRS model were not used in the preliminary chronology of the master thesis. However, that data might be useful for further studies on the surface core. Results are presented in the appendix (Fig. A 1, Table A 4).

Fig. 3: Volcanic glass shard from the Randazzo/Polverello tephra (at 1161 cm). Microscope picture from Giorgia Beffa.

For the chronology in the present study, we just selected the Cs-137 chronological markers which we used to constrain and validate the CRS model. Their uncertainty is defined as the product of half a sampling distance (0.75 cm) and the mean sedimentation rate calculated in CRS model. Additionally, we used 44 radiocarbon ages provided by Giorga Beffa. AMS radiocarbon ages of taxonomically identified terrestrial plant macrofossils were measured at the University of Bern's Laboratory for Radiocarbon Analysis. Finally, we used two identified tephra layers as chronological markers. Ages of the Avellino tephra (524 cm depth) are available from various sources. We selected the following ages: 3550±20 C-14 years BP (Passariello et al., 2009), 3838±20 years BP (Sevink et al., 2011) and 3530±40 C-14 years BP (Zanchetta et al., 2011). For an age date of the Randazzo/Polverello tephra (1161 cm depth, Fig. 3) published by Albert et al. (2013) we used a recalibrated version from Ramsey et al. (2015) based on the more recent IntCal13 calibration curve. This tephra was previously misinterpreted as being from the Biancavilla eruption (Albert et al., 2013; Del Carlo et al., 2017; 2020).

C-14 age dates were calibrated to calendar years using the IntCal20 curve (Reimer et al., 2020). All ages in this master thesis are given in calibrated years before present (before 1950, BP), if not indicated elsewise.

We calculated the age–depth model based on all dates (Cs-137, C-14, tephra) using Bacon in R v. 4.1.1 (rbacon package v. 2.5.7; Blaauw & Christen, 2011). The following parameters were used: d.by = 0.5, thick = 8, acc.mean = 16, acc.shape = 1.5, mem.mean = 0.5.

The chronology allowed us to infer the sedimentation rate (mm/a). To calculate the mass accumulation rate (MAR [$g*cm^{-2}*a^{-1}$]), we multiplied dry density (DD) with the sedimentation rate. The MAR is needed to convert pigment concentrations to flux rates. However, dry density values were only available on a low resolution from studies on the 1995 core (Ramrath, 1997). To estimate flux rates and MAR at 5 mm resolution we inferred DD from XRF based Ti counts. We did this by training a linear regression model on the DD values from Ramrath (1997) with our Ti counts (1 cm average, same location). Next, we multiplied that DD proxy with the sedimentation rate. The resulting MAR proxy is highly correlated with the MAR ($r = 0.98$, $p < 0.01$). Results of that calibration can be found in the appendix (B2).

3.2.2 Sediment description

The sediment was described following Schnurrenberger et al. (2003) and by following internal guidelines of the paleolimnology group (annex H1). We determined a variety of parameters for the sediment description including the presence, colour, composition, and preservation of laminations.

Directly after opening the cores, the colour of the fresh sediment was estimated by using a camera image scanner (smartcube® - smartCIS) at the Institute of Plant Science (IPS) in the University of Bern. Images were acquired for each core with a resolution of 500 dpi. Colour analysis was done in R v. 4.1.1 (R Core Team, 2021). We combined the images (magick package v. 2.7.3; Ooms, 2021) to represent the master core and resampled the composite to 1 mm resolution. We used the clara cluster technique (cluster package v. 2.1.2; Maechler et al., 2021) to estimate the eight dominant colours in the core (significant clusters). In a next step, we estimated continuously, for each 1 cm depth section, the most abundant colour cluster. These colours were translated to the Munsell colour notation using Munsell package v. 0.5.0 (Wickham, 2018). Additionally, to facilitate interpretation, we noted their ISCC-NBS colour name (Kelly & Judd, 1976) using the munsellinterpol package v. 2.6-1 (Centore et al., 2020).

Sediment composition was analysed using smear slides at selected locations (see Table A 6) and following the University of Minnesota tool for microscopic identification (https://tmi.laccore.umn.edu/). We put 1-2 mm^3 material on a distilled water droplet on a microscope slide and smeared it to a very thin film. After drying, a glass cover slip was glued with an optical glue (Norland Optical Adhesive 61) on the microscope slide to cover the sample.

Unconstrained clustering on the XRF, HSI, and MS dataset was used to define the dominant lithotypes (phases of similar geochemistry). Furthermore, published geochemical data on Lago di Mezzano (Ramrath et al., 1999a, 1999b, 2000; Wilkes et al., 1999) was attached to these lithotypes. This information on the lithotypes was then used to guide the sediment description. The statistical method is described in the statistical method chapter (3.3) whereas the external geochemical data is described in the data chapter (4).

3.2.3 Hyperspectral imaging (HSI)

Hyperspectral imaging (HSI) was conducted at the University of Bern's Institute of Geography (GIUB) by using a Specim PFD-CL-65V10E line-scan camera, following the methodology of Butz et al. (2015). This camera works at a spectral resolution of 2.8 nm, ranging from 400 to 1000 nm (visual to near infrared spectrum), with 784 bands. Scans were performed on the oxidised core halves with a spatial resolution of 83 µm and an exposure time of 160 ms (Aperture: 1.9, Spectral bin: 2, FOV: 109.3333 mm, speed 0.5, fr: 6 Hz). We used the same settings to scan the entire master core to ensure comparability between the core

sections. The fresh blocks of the Bronze Age case-study section were scanned with a spatial resolution of 25 µm. This is the highest resolution possible given the camera focus and core movement precision. It is the highest resolution that has ever been scanned with this machine. Exposure was set to 160 ms as well (Aperture: 1.9, Spectral bin: 2, FOV: 32.8 mm, speed: 0.15, fr: 6 Hz). We processed the spectral data in ENVI (v. 5.4). Scanned spectral raw data were normalised to a white standard ($BaSO_4$ ceramic plate) whereas background camera noise was removed using a dark standard (closed camera shutter). Thus, the data is placed on a scale from zero to one, where one is the reflectance of the white standard and zero is the reflectance of the dark standard.

Subsequently, relative absorption band depths (RABD) were calculated as proxies for sedimentary green pigments (chlorophyll *a* and *b* and diagenetic products, TChl) and bacterial pigments (bacteriopheophytin *a* and *b,* Bphe) as developed by Butz et al. (2015; 2016; 2017). The $RABD_{655\text{-}685max}$ index (formula 1), a proxy for TChl, is representative for algae bearing this pigment, including blue-green algae. TChl indicates primary productivity (and eutrophication) in a lake. The $RABD_{845}$ index (formula 2) represents Bphe, a biomarker indicating purple sulphur bacteria that live at the chemocline in stratified lakes, and require both light and reduced sulphur (Yurkov & Beatty, 1998). Therefore, this index is used as an indicator of hypolimnetic anoxia reaching the photic zone. Furthermore, we use the R850/R900 ratio as a proxy for lithogenic influx. That index was developed in a study on Emerald lake on Macquarie Island, a landmass in the Southern Ocean (Saunders et al., 2018). This sub-Antarctic island has a volcanic catchment similar to Lago di Mezzano. For the depth profiles we averaged the indices over a 2-mm-wide subset. We masked areas that are either very dark or bright or have cracks by applying core specific reflectance thresholds. The RABD indices were calculated with the following equations.

$$(1)\ \mathrm{RABD}_{655-685\mathrm{max}} = \frac{X * R590nm + Y * R730nm}{X + Y} / Rmin655 - 685nm$$

With the X and Y changing for each pixel depending on the trough position (Rmin655-685nm):

X = number of spectral bands between Rmin655-685nm and R730.66nm

Y = number of spectral bands between Rmin655-685nm and R590.2nm

$$(2)\ \mathrm{RABD845nm} = \frac{34 * R790nm + 34 * R900nm}{68} / R845nm$$

Beside the spectral indices, we mapped vivianite using ENVI's spectral angle mapper algorithm (threshold 0.08 rad) inspired by work of Butz et al. (2017). We trained the algorithm on 13 vivianite minerals on the core MZZ-F 3-4W. The algorithm assigned each pixel to the most similar vivianite reference spectra or left the pixel unclassified if the spectral angle threshold was exceeded. In some cores the vivianite type 2 and 3 included dark sediment parts. Therefore, these types were excluded in the noisy sections (see Table A 7). We then continuously summed up the classified vivianite pixels for each 5 mm depth section (constant width of 55 mm). Hence, a data point in the depth profile is the sum of classified vivianite pixels in an area of 5x55 mm.

The two RABD indices were proxy-proxy calibrated to pigment concentrations ($\mu g/g_{dry\ sediment}$) following Butz et al. (2015, 2017). We took 38 samples from specific sites in the sediment with a minimum dry weight of 1 g. We optimised sampling in order to cover the full range of both RABD indices while maintaining a record through time. We extracted the pigments from the freeze-dried and ground sediment using HPLC grade acetone (SOP in the appendix H2). The pigment concentrations of the extract were measured by a spectrophotometer (Shimadzu UV1800, SOP in the appendix H3). Beside TChl and Bphe, we measured total carotenoids (TC) by this method as well. They are a proxy of total phosphorus in lake water (Guilizzoni

et al., 2011). However, as we haven't done a loss-on-ignition analysis on these samples, we give the concentration per gram dry sediment ($g_{dry\ sediment}$) and not per gram of organic matter (g_{LOI}). This is different to the standard procedure reported in the SOP (Annex H3). Furthermore, based on TC and TChl of these samples we calculated the TC/TChl ratio. High ratios may indicate the presence of cyanobacteria or anoxic conditions as TC is more abundant in cyanobacteria and better preserved under anoxia (Swain, 1985). The spectrophotometrically measured pigment concentrations are presented in the appendix D2.

To calibrate the two RABD indices, we used a linear regression model between measured sedimentary pigment concentrations and mean RABD index values on sample locations. In the model we ignored TChl values <5 μg/g and Bphe values <1 μg/g, as they are too close to the detection limit of the spectrophotometer. We detected that the TChl was underestimated in dark areas of the core. Therefore, we tested a shape constrained additive model (SCAM) using the $RABD_{655\text{-}685max}$ index and the brightness (Rmean) as explanatory variables. We used the simpler pigment calibration model for subsequent analysis, as the non-linear model did not truly improve the calibration over the entire core. The models were calculated in R v. 4.1.1 (R Core Team, 2021). Results of the SCAM are shown in the appendix D2. Furthermore, we calculated pigment flux rates based on the mass accumulation rate (MAR) and the pigment concentration. For our 5 mm resolution datasets we used our MAR proxy (see chronology chapter 3.2.1). We use flux rates in the analysis as they are not affected by the dilution effect.

3.2.4 X-ray fluorescence (XRF)

To acquire semi-quantitative information on the elements present in the sediment, XRF-core scans on oxidised core halves were conducted with an ITRAX-XRF scanner at the University of Bern's Institute of Geological Sciences. A chromium(Cr)-target X-ray was used to accelerate electrons over an exposure time of 30 s (scans in 2019) or 20 s (scans in 2020 and 2021) at 30 kV and 50 mA. Unlaminated segments were scanned with a resolution of 0.5 cm, while continuously laminated areas were scanned with a resolution of 200 μm. We scanned with an overlap of 40 cm between the core segments of different retrieval years to ensure comparability. During scanning, the core was covered with a thin and resistant plastic film to prevent desiccation, which may affect elemental counts of atomic numbers below Ca (Jarvis et al., 2015). XRF spectrum data were re-evaluated by using 20 iterations to obtain better elemental counts. Table 1 shows the elemental proxies tested and further investigated.

XRF elemental counts were postprocessed in R v. 4.1.1 (R Core Team, 2021). First, we set elemental counts below the detection limit (100 cts) to zero. The first and last 5 mm at the top and bottom of the sediment of each core segment were masked to remove edge effects. Second, we checked the XRF and SmartCIS optical images for obvious cracks. These visible cracks were classified to three groups (Table A 8). As Ar is present in the air, this element was additionally used as a method to detect cracks that formed during scanning. Based on tests, we then defined an Ar peak as the exponential derivative of the Ar counts which are larger than $1.5*10^7$. Cracks in turn were detected by the following argument. *Crack = Ar peak | Class 2 crack from the optical images | all crack classes from optical images with a visible increase in Ar counts.* We masked the 5 mm above and below the position of these cracks. In the future, it might be useful to take a second picture directly after the XRF scan to facilitate crack detection. This is an important lesson learned and could avoid such complicated procedures for crack detection.

Third, scanning results from 2019 and 2020/2021 differed systematically. The lower sensitivity in the scans from 2020 and 2021 can be explained by the shorter exposure time and the Cr-tube aging of the ITRAX scanner. To correct for that effect, we standardised the data from 2020 and 2021 to the level of 2019. We used the overlap between the core segments scanned in 2019 and 2020 to estimate their respective mean and standard deviation. This information was used to homogenise the entire core. For the core segment

MZZ-D 8.5-9.5W (scanned in 2021) we had to apply a second, similar homogenisation using the overlap given by the respective 20 cm sections centred around the upper and lower jump point. A possible explanation for this systematic deviation is that the power generator of the XRF machine broke after completing the scan. A few elements displayed negative values after the standardisation. We shifted these profiles so that the minimum is zero and no longer negative. Finally, we tested a normalisation by the Inc/Coh-scatter ratio to account for the influence of water content (Davies et al., 2015). A comparison with the resin blocks (Bronze Age case-study section, Fig. A 9) showed that there is no substantial improvement and that the water content is not a big problem in that section. This is a good sign as the water content (data from Ramrath, 1997) varies a lot throughout the Bronze Age. Indeed, it covers nearly the entire water content range. Details can be found in the appendix (chapter E2).

Table 1: Tested (grey) and further investigated (black) elemental proxies.

Proxy	*Process*
Ti	erosion (Davies et al., 2015)
K	abundant catchment mineral: erosion
Si	abundant catchment mineral: erosion or diatoms (Davies et al., 2015)
Fe	abundant catchment mineral: erosion or oxic conditions (Davies et al., 2015)
Ca	increased evaporative concentration (lake level) and endogenous calcite precipitation or biogenic production (Davies et al., 2015)
Ca/Ti	increased evaporative concentration (lake level) or endogenous calcite precipitation (Davies et al., 2015). However, calcium precipitation might also be driven by increased pH levels, e.g. as a reason of higher aquatic primary productivity (Wetzel, 2001).
S	gypsum, low lake level, but S also from other processes as soil leaching (Davies et al., 2015)
Br	organic material, lake production (Davies et al., 2015)
Si/Ti	increased biogenic silica (Davies et al., 2015)
P	nutrient enrichment (Corella et al., 2012; Davies et al., 2015), anoxia and reduced mixing (Boehrer et al., 2017). However under anoxia reduced P-trapping due to reductive dissolution (Tu et al., 2019)
Fe/Mn	reducing conditions and anoxia (Davies et al., 2015; Makri et al., 2021a), in dimictic lakes only working under reduced erosion and holomixis (Makri et al., 2021a)
(Fe/Ti)/Mn	anoxia, corrected for catchment input / erosion (own development)
Cu/Rb	copper mining and use (Davies et al., 2015; Guyard et al., 2007)
Pb/Rb	lead mining and use (Davies et al., 2015; Guyard et al., 2007)
Fe/Ti	smaller grain size, but also redox conditions (Davies et al., 2015)
Zr/Rb	larger grain size, however, not working in areas with k-Feldspars (Davies et al., 2015)
Ti/K	larger grain size (Davies et al., 2015)
K/Al	physical weathering (Davies et al., 2015)
K/Ti	physical weathering (Davies et al., 2015)
Rb/K	chemical weathering (Davies et al., 2015)
MS/Ti	Magneto tactic bacteria, anoxia (own interpretation)

3.2.5 Micro X-ray fluorescence (µXRF)

Micro-XRF scans were performed at the Institute of Plant Sciences (IPS) using the Tornado M4 µXRF scanner. First, scans were applied on the laminated Bronze Age case-study section using fresh (no resin treatment) 18 cm subsections cut out as U-channels from half cores. These aluminium framed U-Channels were scanned in three line-scans at the position of the 2-mm-wide HSI subsets (middle and edges, spaced 1 mm apart) with a resolution of 25 µm. That is the same resolution as the HSI block-scans and should ensure data comparability. A rhodium(Rh)-target X-ray was used to measure the sediment for 100 ms at 50 kV and 300 µA in a helium flushed chamber. For the resin blocks, we applied a map-scan on the 2 mm wide subset defined by HSI. Here, we used the same target-tube to accelerate electrons. However, we reduced the resolution to 50 µm and the exposure time to 20 ms. We scanned under vacuum at 50 kV and 600 µA.

On the stratigraphically correlated dataset we applied the following corrections for the resin blocks. First, we aligned the individual lines of the map-scan to the centre line (the laminations are bended) using dynamical time warping in R (dtw package v. 1.22-3; Giorgino, 2009). Testing showed that a window size of 20 data points (1 mm), with a "symmetricP2" step pattern and a "Sakoe Chiba" band works best. From this aligned dataset we calculated the average of each depth section (50 µm). Second, we detected cracks (pure resin) by applying the following rules which proved best in testing: We scaled the elemental ratio (Mn/Fe)/Ti and took the inverse (*-1). Every value above -0.5 was defined as a crack. Additionally, Ca counts above 150 were also defined as cracks. High Ca counts are related to the adhesive putty that holds the blocks in place during scanning. The line-scan data on the fresh blocks were not postprocessed or analysed further because we exported the data in percentages instead of elemental counts. Therefore, the averaging of the three line-scans was no longer useful. This error is due to incorrect software settings and limited export options for line-scan data in the Bruker software. We suggest using the map-scan mode (creates element maps) which is much more user-friendly and allows to export all the element maps as *.txt file processable in R. The µXRF scans were used in the following to verify the presence/ absence of varves. We found that most varves are very badly preserved and hence, seasonal analyses were not further investigated in detail.

3.2.6 Magnetic susceptibility (MS)

Magnetic susceptibility was measured over 1 s in continuous 5 mm intervals over the entire core. Sediment was left covered with one layer of plastic film used for packing the cores. We did this by using a Bartington MS2E spot-reading sensor connected to the MS3 magnetic susceptibility meter at the IPS. Measurements were drift corrected against the magnetic background in the air. We masked the first and last centimetre of the measurement on each core segment to remove edge effects. These cleaned data were used in our analysis. Furthermore, we stratigraphically correlated the data of Lago di Mezzano from the 1995 sediment core (Brandt et al., 1999; Ramrath et al., 1999a; 1999b; 2000; Sadori, 2018; Sadori et al., 2004; Wilkes et al., 1999) to our master core using magnetic susceptibility. Details on this procedure are presented in the data chapter.

3.3 Statistical methods

For our analyses we worked with a variety of multi-proxy datasets with changing resolutions, proxies, and time periods. Table 2 shows the used datasets and the proxies they contain. All our analyses were done in R v. 4.1.1 (R Core Team, 2021). For visualisation we used the R packages ggplot2 v. 3.3.5 (H. V. Wickham, 2016), cowplot v. 1.1.1 (Wilke, 2020), tidypaleo v. 0.1.1 (Dunnington, 2021), and factoextra v. 1.0.7 (Kassambara & Mundt, 2020). We log-transformed and scaled all datasets prior statistical analyses.

First, we averaged our scanned HSI, XRF, and MS proxy data for each 5 mm depth section continuously. Next, based on the obtained chronology, we added the sedimentation rate, and the pigment flux rates. The result is a first multi-proxy dataset with a resolution of 5 mm covering the entire core. We name it the scanning-proxy dataset. Here, we applied a stratigraphically constrained hierarchical cluster analysis by the method of incremental sum of squares (CONISS) using euclidian distances (rioja package v. 0.9.26; Juggins, 2020). We selected eight significant CONISS zones based on a broken-stick model to distinguish between similar time periods (units). These units help to structure our results chronologically. In a next step, unconstrained hierarchical clustering was performed using euclidian distances and ward.D2-linkage. With this linkage-method we were able to obtain the best cluster structure (agglomerative coefficient of 0.995, cluster package v. 2.1.2; Maechler et al., 2021). We selected five clusters based on an elbow and average silhouette test. Similar results were achieved using the kmeans method (1000 iterations) meaning that the selected clusters are robust. These lithotypes highlight phases of similar interactions between the different processes in the lake ecosystem and support the sediment description. Principal component analyses (PCA)

were applied to two time periods. One under human influence (CONISS 5-8) and another with minimal human interference (CONISS 1-4). Furthermore, we calculated individual PCAs for each unit. A broken-stick model identified the number of significant principal components (vegan package v. 2.5.7; Oksanen et al., 2020). These PCAs show the relationships between the geochemical proxies and reveal changing interactions over time in the lake-ecosystem.

Second, we combined our scanning data (HSI, XRF, MS) with the published data of Lago di Mezzano and with climate data from other sites. Both external datasets were tied to our master core. Details about this procedure and the data itself can be found in the data chapter. To aggregate the data, we averaged our scanning data continuously for each 1 cm section. Next, we selected from the scanning data all the 1 cm depth sections that are present in the discrete Mezzano and Climate dataset. Hence, both datasets use the same interval based on the geochemical data of Ramrath (1997). In a next step, we calculated the MAR and pigment fluxes based on Ramrath's dry density values, the sedimentation rate, and the pigment concentrations. This resulted in a second dataset, which we call the full multi-proxy dataset. Again, PCAs were conducted on two time periods to understand the lake-catchment-climate relationships. A first one with likely no human interference (units 1-4) and a second one under clear human influence (units 5-8). For the first time period, we excluded human indicator pollen as they are not associated with human activity in the Late Glacial, as well as the humidity indicator, as there is only very little data available for that section (see data chapter). The significant number of PC's was identified by a broken stick model. On the same time periods and variables, we conducted two redundancy analyses (RDA) using the vegan package v. 2.5.7 (Oksanen et al., 2020). As explanatory variables we selected proxies on erosion, hydrology, land cover, vegetation changes, fire dynamics, anthropogenic impact, and climate. In turn, dependent variables are restricted to in-lake processes. The two sets of variables are indicated in Table 2. This configuration helped us to better understand how the catchment and climate are influencing the lake. Also, it helped us to disentangle the influence of human pressure from that of natural variability for the lake ecosystem of Lago di Mezzano. This assists us in making inferences about the future behaviour of warm-monomictic lakes in the Mediterranean region.

For the Neolithic case-study section, we combined our scanning-proxy dataset, the sedimentation rates, and the high-resolution pollen counts of Giorgia Beffa to one record of 5 mm resolution (see Table 2).

For the Bronze Age case-study section we do not provide any statistical analysis because of the insufficient varve preservation. However, we present the available data and discuss the potential of such ultra-high-resolution data (50 μm resolution).

Table 2: Datasets and proxies used in the statistical analysis. Explanatory variables used in the RDA are indicated in grey.

Dataset	***Proxies***	***Resolution***
Scanning-proxy dataset	Ti, R850R900, K, Si, Fe, MS, SR, Rb/K, K/Al, TChl flux, Si/Ti, Br, P, Bphe flux, (Fe/Ti)/Mn, vivianite	5 mm continuous
Full multi-proxy dataset	Ti, OI, MAR, TChl flux, Si/Ti, P, Bphe flux, (Fe/Ti)/Mn, vivianite, AP, NAP, charcoal, human indicator pollen*, Mezzano lake level, CC26 hydro index*, Chironomid Jul temp	1 cm discrete (interval Ramrath, 1997) * not used in the natural time period
Neolithic case-study section	Ti, Rb/K, SR, TChl flux, Si/Ti, P, Bphe flux, (Fe/Ti)/Mn, vivianite, AP, NAP, human indicator pollen	5 mm continuous

4 Data

4.1 Biogeochemical and palynological data from Lago di Mezzano

Several published and unpublished datasets from Lago di Mezzano were used in our analysis. First, we examined the pollen, fungal spores, and charcoal data counted by Giorgia Beffa on the master core. These data will be presented in more detail in a later stage (unpublished data). Second, most published datasets (Brandt et al., 1999; Ramrath et al., 1999a, 1999b, 2000; Sadori, 2018; Sadori et al., 2004; Wilkes et al., 1999) rely on three parallel sediment cores (LMZ A, B, and C) that were retrieved from the centre of Lago di Mezzano in 1995. The researchers from GFZ Potsdam used a modified Livingston corer called an Usinger piston corer. Third, one study used geomorphological evidence (Giraudi, 2004).

Extensive palynological investigations were conducted by Giorgia Beffa on the master core used in this thesis. She established only a low-resolution overview (ca. 30 cm, n = 38) as a higher resolution overview (8 or 16 cm, n = 120) of such data has already been published by Sadori (2018). Therefore, we use the data of Sadori for analyses of the entire core. Both data sets were compared and have been found to be sufficiently similar (see annex F2). The project of Giorgia Beffa focuses on two new high-resolution sections in the Iron Age and the Neolithic. The latter case-study section is already counted (5 mm resolution, n = 185). Therefore, it is used in this master thesis. The data cover pollen, fungal spore percentages and concentrations. In the future, that dataset will be expanded to include older times in order to precisely catch the advent of farming. We aggregated that pollen data to relevant proxies of land use and human impact. Table 3 shows the proxies we used as well as the underlying data.

Table 3: Pollen data and derived proxies.

Proxy	*Beffa (unpublished, overview and Neolithic)*	*Sadori, 2018 (overview)*
Human indicator (since Neolithic)	Cerealia-indet, Hordeum-type, Secale, Plantago lanceolata-type, Urtica	Avena/Triticum, Hordeum, Secale, Plantago, Urticaceae
Arboreal pollen (AP)	Trees and shrub (percent terr. pollen)	Arboreal pollen
Non arboreal pollen (NAP)	Herbs (percent terr. pollen)	Non arboreal pollen
Charcoal	Charcoal conc.	Charcoal 10-50 μm, 50-125 μm and >125 μm

On LMZ-A and LMZ-B a variety of biogeochemical properties were analysed. They include dry density (DD), water content, total organic carbon (TOC), total inorganic carbon (TIC), total carbon, loss-on-ignition at 550°C ($LOI_{550°C}$, organic matter), biogenic SiO_2 (BiO), total sulphur, total biogenic matter (BiM), total minerogenic matter (MiM), hydrogen index (HI), and oxygen index (OI) (Brandt et al., 1999; Ramrath, 1997; Ramrath et al., 1999a, 1999b, 2000; Wilkes et al., 1999). HI indicates hydrogen rich organic matter (aquatic source) whereas OI indicates oxygen rich organic matter (terrestrial source, detrital input). The biogeochemical properties were analysed in 5 cm^3 samples covering a depth of 1 cm in an interval of up to 5 cm (60 -15 yr with SR 0.8-3 mm a^{-1}) depending on the proxy and depth. All the biogeochemical data could be obtained from the annexes in Ramrath (1997) and Wilkes et al. (1999). Furthermore, Ramrath (1997) established a varve-based chronology tied by AMS radiocarbon dates obtained from the bulk sediment. It has its limitations (see study site chapter). This chronology, as well as calculated sedimentation rates, mass accumulation rates, and flux rates are available in Ramrath's (1997) annex (to a depth of 1115 cm – 5 cm resolution). Furthermore, different components of the sediment (siderite, pyrite) and diatom species (benthic and planktonic) were identified semi-quantitatively under the microscope using 407, 10-cm-long, resin-embedded, thin sections on LMZ-A and LMZ-B (Ramrath, 1997; Ramrath et al., 2000). These data were digitised from Fig. 12 and 13 in the doctoral thesis of Ramrath (1997, pp. 40, 44) using the digitalisation software WebPlotDigitizer v. 4.4. All that data is referenced to Ramrath's composite depth on the master core LMZ-B. We aggregated all the values to the discrete interval of the TOC values (resolution of 10 cm in the section of interest).

Magnetic susceptibility has been logged in 5 mm resolution on the core LMZ-C. This core is reported to be exactly parallel to the master core LMZ-B. Brandt et al. (1999) used a Bartington MS2F spot-reading sensor with a MS2 magnetic susceptibility meter. Data were kindly shared by the co-authors Norbert Nowaczyk and Achim Brauer from the GFZ Potsdam.

We stratigraphically correlated the above datasets, which use the master core of Ramrath as reference, to our master core. Therefore, we compared our magnetic susceptibility record to the one of Brandt et al. (1999) which uses Ramrath's master depth. This allowed us to tie all the data from the 1995 cores to our core with very high precision (ca. 1 -3 cm). This included the master depth of Ramrath. Therefore, all reported depths referring to Ramrath's depth are directly comparable to our master depth. We used this to access the accuracy of the stratigraphic correlation at the positions of the reported tephra layers. The reported depth of the Avellino tephra (T1) was exactly placed where we found it. Hence, we have a perfect alignment in this section. For the Randazzo/Polverello tephra we detected an offset of 3 cm between the reported depth (there interpreted as Biancavilla tephra, T2) and the position in our core. Fig 7 in Ramrath's doctoral thesis (1997, p. 24) shows that this is potentially because of a slight mismatch between the cores LMZ-C to LMZ-B after 1200 cm Ramrath depth (1055 cm master depth).

Furthermore, records of pollen and charcoal were counted up to a depth of 1200 cm on the core LMZ-B (Sadori, 2018; Sadori et al., 2004). However, this data has not been shared with us. Therefore, we digitised our pollen proxies (Table 3) from Sadori's pollen percentage (Fig. 4) and the concentration diagram (Fig. 5) using again WebPlotDigitizer v. 4.4 (Sadori, 2018, pp. 35, 36). These datasets were plotted against time. Hence, we derived Sadori's (2018) age depth model (see appendix F3) based on the location of her pollen assemblage zones and the depth scale of Fig. 4 in her paper (Sadori, 2018, p. 35). Next, Sadori's age depth model was used to translate Sadori's ages to Ramrath's master depth and subsequently to our master depth. Thus, this indirect stratigraphic correlation is less precise than the direct stratigraphic correlations over Ramrath's master depth. This data was then aggregated to relevant proxies of land use and human impact. The used proxies and the underlying data are presented in Table 3.

The geomorphological study by Giraudi (2004) presents past lake levels variations. Due to the good documentation in the study, data retrieval from the paper was possible. However, there were also obvious gaps concerning the timing of lake level changes. This is why we improved the dataset based on information on timings and extents of lake level fluctuations documented at Lago Fucino (Giraudi, 2004) and in the biogeochemical data of Ramrath et al. (2000). Our improved curve together with the original record of Giraudi (2004) are presented in the annex F1.

4.2 Paleoclimate data

We used published independent climate proxy data on temperature and humidity from central and northern Italy to support our analysis. For temperature, we used reconstructed chironomid-based July air temperature. These data come from Lago di Origlio (Samartin et al., 2012), Lago della Costa (Samartin et al., 2016), as well as Lago Gemini Inferiore and Lago Verdarolo (Samartin et al., 2017). The locations of these lakes are shown in Fig. 1. Data was kindly shared by Christoph Schwörer (IPS). To ensure data comparability, we adjusted the temperatures of all lakes to the altitude of Lago di Mezzano (452 m a.s.l.) assuming an altitudinal lapse rate of 0.6 °C/100 m (Livingstone et al., 1999; Livingstone & Lotter, 1998). In a next step, we applied a moving average filter (window size = 3) on the combined dataset. This temperature record was stratigraphically correlated to our record using the Bacon age depth model.

Hydroclimatic variability for the Holocene in Italy was inferred from the CC26 stalagmite in the Corchia cave in central Italy. We used the mean anomaly index (resolution <10 years) published by Regattieri et al. (2014). This index is based on trace elements (Mg/Ca) obtained in that study as well as isotope data ($d^{18}O$ and $d^{13}C$) investigated earlier (Zanchetta et al., 2007). Higher values indicate a drier hydroclimate (Regattieri et al., 2014). Data was kindly shared by Gianni Zanchetta. We stratigraphically correlated that data to our record using our chronology.

5 Results

5.1 Chronology

Our preliminary chronology (v. 02.10.2021) reveals an extrapolated basal age of 18,393 years BP (17,660 - 18,946 years BP). We detected no outliers in our age-depth model. The MCMC iterations do not show any structure and the posterior distributions for the accumulation rate and memory fit well to the prior assumption (Fig. 4, top panel). The mean age error (95% confidence interval) over the entire core is 582 years. However, the mean age error changes considerably throughout the core (5 - 1380 years). The lowest mean age errors are in the topmost 20 cm (5 - 30 years). Below the error increases and stays until the beginning of Neolithic between 100 and 600 years. The three age dates of the Avellino tephra layer were used as chrono-markers and substantially reduced uncertainty. In the Neolithic period we have a high precision thanks to the high density of C-14 dates (100 - 300 years). Thereafter the age error gradually increases and stays in the range of 500 - 1380 years.

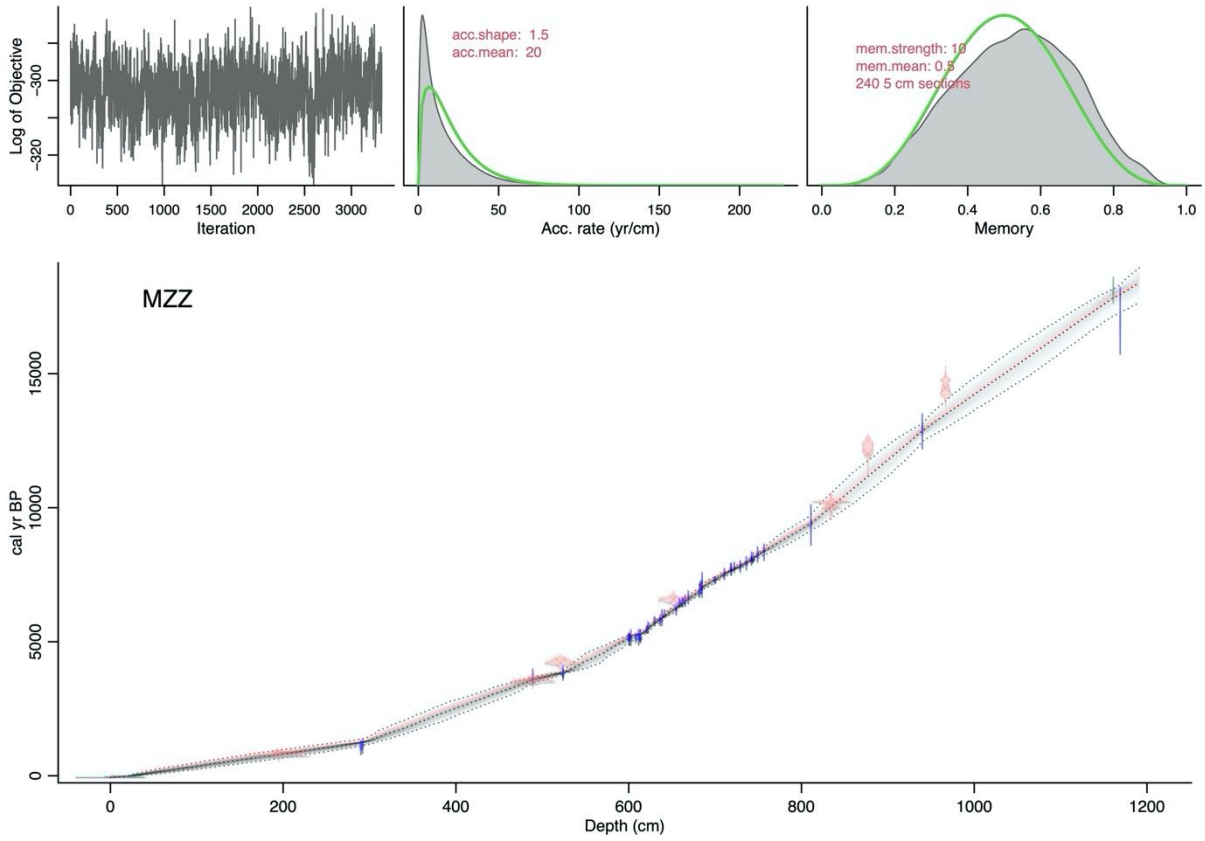

Fig. 4: Preliminary age-depth model (v. 02.10.2021). The upper panels show MCMC iterations (left) as well as the prior (green) and posterior (grey) distributions for the accumulation rate (middle) and the memory (right). The lower panel depicts our age-depth model (mean age in red, 95% confidence interval in grey) with here calibrated C-14 age dates (blue), calibrated chrono-markers (green), and bulk dated C-14 AMS dates influenced by the reservoir-effect from Ramrath (1997), Ramrath et al. (2000) and Sadori (2018).

Calibrated radiocarbon dates of Ramrath and Sadori (Fig. 4, lower panel, in red) are either in the 95% confidence interval or older than our estimates. Thus, confirming a varying C-14 reservoir-effect (too old ages) of their bulk-dated chronology (Ramrath, 1997; Ramrath et al., 2000; Sadori, 2018). Furthermore, none of Ramrath's and Sadori's age dates are younger than our estimates, which highly supports the validity of our chronology. We observe a very high sedimentation rate (SR) at the very top (4 mm/a), it remains at high levels (2 mm/a) until 3 m. Then the SR stabilises at 1 mm/a, gradually decreases to 0.5 mm/a until 6 m to remain on that level until the bottom. These rates are comparable to Ramrath's (1997) reports.

5.2 Sediment description and lithotypes

The sediments are mostly composed of silty clay (a clastic sediment) dominated by feldspars. However, there are also a few sections with a high content of biogenic matter (BiM>50%). We identified these sections as diatomaceous ooze (a biogenic sediment). Biogenic matter is composed of organic matter and diatoms. Fig. 5 shows the main results of the sediment description combined with statistical evidence. The presence, colour, composition, and preservation of laminations change throughout the core and are described in the next section from the bottom to the top.

Unit 1 (1191-993 cm, 18.4-14.1 ka BP) has at the base (18.4 ka BP, 1191 cm) a massive greyish green silty clay which is bedded (5 - 12 cm). That clastic sediment (BiM < 50%) was clustered to lithotype 3. Feldspar, quartz, iron oxides and vivianite are the dominant minerals. At 1161 cm is a coarse dark silt layer. It was identified as the Randazzo/Polverello tephra and contains volcanic glass shards. From 1095 to 993 cm the massive sediment is no longer bedded. A first section (until 1063) has organic detritus in dark layers every 2 - 4 cm whereas the following section is homogenous silty clay. Thus, the sediment remains clastic with frequent feldspar and iron oxides.

Unit 2 (993-879.5 cm, 14.1-11.2 ka BP) begins with bedded silty clay (3- 8 cm) which ends at 926 cm. The first section (until 942 cm) is darker (dark greyish green) than the second (greyish green). Also, it has a BiM content of up to 40% compared to 20% before and after. After 926 cm the massive greyish green silty clay is no longer bedded and gets gradually darker (dark greyish green).

In unit 3 (897.5-812.5 cm, 11.2-9.4 ka BP) we observe from 879 cm on a poorly preserved laminated dark greyish green diatomaceous ooze (BiM > 50%). That sediment is classified as lithotype 4. Ramrath (1997) identified these dark laminations as biogenic varves with two layers (varve type 1). The spring/summer layer is formed by diatoms whereas the autumn / winter layer consists of organic material (Ramrath, 1997). This pattern was confirmed by smear slide analysis. At 836 cm the preservation of the 0.5-2 mm thick laminations improves.

In unit 4 (812.5-708.5 cm, 9.4-7.4 ka BP) the laminations remain in moderate preservation until 771 cm. However, the biogeochemistry changes at 812 cm to lithotype 5. After 771 cm follows a short section of poorly preserved laminations. At 753 cm the diatomaceous ooze changes to moderately to well preserved laminations (0.5 - 5 mm thick), also the colour is a bit brighter with more greyish green components. The laminations and lithotype 5 end at 706 cm at a massive bed (3-5 cm thick).

Unit 5 (708.5-528 cm, 7.4-3.9 ka BP) starts with a 6 cm massive section. In the following, the biogeochemical properties switch to lithotype 4, and the sediment to dark greyish green - very dark bluish green laminated ooze until 610 cm. This is only interrupted by a massive section from 679 to 669 cm. From 610 cm the colour changes to greyish green and the laminations deteriorate and vanish after 596 cm. This section is classified as lithotype 2. From 596 cm on follows a 47 cm-long massive section with similar biogeochemical

properties as the laminated part before (lithotype 4). At 549 cm the diatomaceous ooze gets again laminated, however only poorly preserved.

Unit 6 (528-442.5 cm, 3.9-3 ka BP) begins with the Avellino tephra (524 cm). Next, the sediment changes to massive greyish green silty clay (BiM < 50%) and to the lithotype 2. The light grey layer of the tephra deposit is at the position reported by Ramrath (1997) and contains volcanic glass shards. From 507 cm on the sediment has moderate preserved laminations (0.5 - 2.5 mm thick).

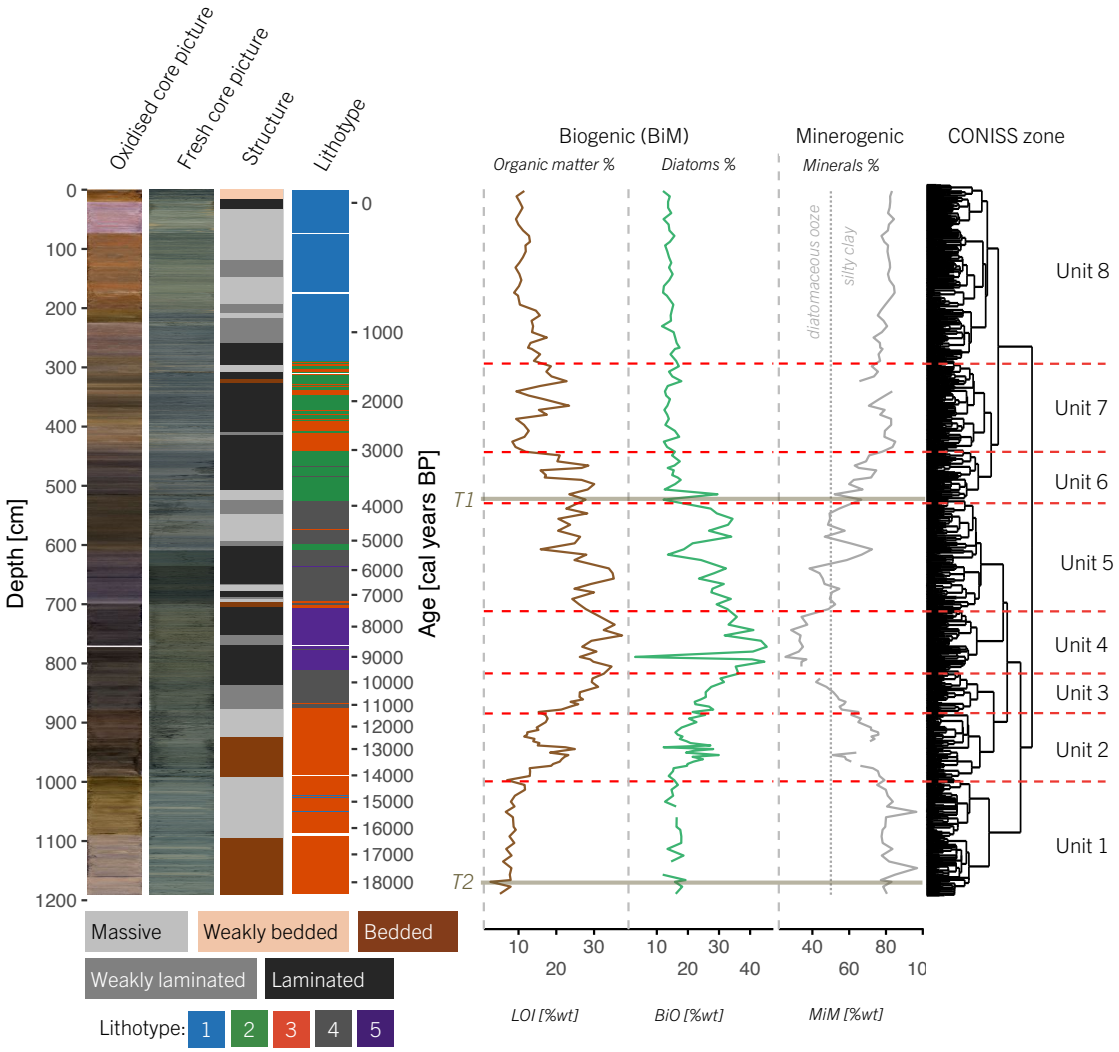

Fig. 5: Sediment description with oxidised sediment colour, fresh sediment colour, laminations, lithotype, sediment composition, and CONISS zones. The sediment composition is given in percentage wet weight [%wt]. We use the following proxies from Ramrath (1997): LOI indicates organic matter, BiO indicates diatoms and MiM indicates the percentage of minerals. Smear slides were used to confirm the sediment composition. T1 is the Avellino tephra and T2 the Randazzo/Polverello tephra.

At the start of unit 7 (442.5-294.5 cm, 3-1.3 ka BP) the dark laminations are replaced by brighter laminations with a higher clastic content. These laminations were identified by Ramrath (1997) as biogenic varves with a minerogenic competent (varve type 2). These varves have up to three layers. A spring/summer layer is formed by amorphous organic matter and few planktonic diatoms. Sometimes that layer contains fine silt or vivianite. Interbedded comes occasionally a layer of siderite. The autumn/winter layer is formed by organic material, benthic diatoms and silt and clay minerals (Ramrath, 1997). We could confirm the higher clastic content of these brighter laminations by smear slide analysis. These brighter laminations are first moderately to well preserved and between 1 and 5 mm thick. That change is also reflected in altered

biogeochemical properties (now lithotype 3). The preservation of these laminations gets worse between 424 and 392 cm. At 392 cm the biogeochemical properties change to lithotype 2 and remains similar until 310 cm (with some lithotype 3 sections). Also, a 6 cm thick bed interrupts the laminations at 327 cm. The laminations are only moderately preserved thereafter, and vivianite is very abundant for the next 40 cm. From 310 to 297 cm a massive section of greyish green silty clay is present (lithotype 3).

In unit 8 (294.5-0 cm, 685-2019 CE) the biogeochemical properties change to lithotype 1. From the start to 195 cm, the laminations are poorly to moderately preserved and show in the first 15 cm occasional beds. Also, a massive section interrupts the laminations (218 – 209 cm). Thereafter, follows massive greyish green silty clay until 34 cm. This is interrupted by a 27 cm long section of poorly preserved bright laminations. From 34 cm the sediment is laminated (3-10 mm thick). At 17 cm the laminations get thicker and are replaced by weak beds (1 cm thick). At the top the sediment is a weakly bedded dark greyish green silty clay.

Over the entire core, we identified five lithotypes based on unconstrained clustering of the scanning-proxy dataset (see statistical methods). Lithotypes are sediments with similar biogeochemical properties and underline time periods of similar interactions between the different processes in the lake ecosystem.

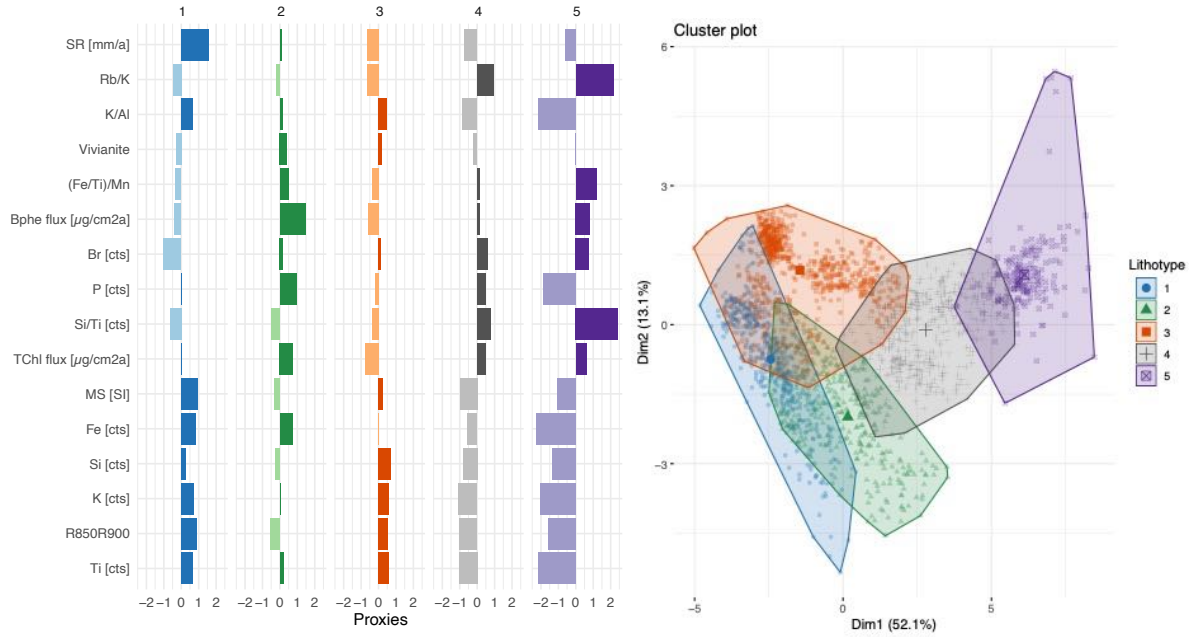

Fig. 6: Results from unconstrained clustering. The left panel shows the mean values for each lithotype whereas the right panel depicts the lithotypes in the PC1–2 space (the PCs are explained in chapter 5.4).

Lithotype 1 (Fig. 5 and Fig. 6, blue) stands out with its high SR. We observe high physical weathering (high K/Al and OI, low Rb/K and HI) as well as elevated erosion indicators (MS, Fe, Si, K, Ti, R850R900). Anoxia indicators (Bphe flux, (Fe/Ti)/Mn) and productivity indicators (Si/Ti, Br, TChl flux) are mainly low. The TChl flux varies in this lithotype. Most values are low whereas they are very high in the last century resulting in a mean value slightly above average. Furthermore, that lithotype is highly clastic (very low BiM) and shows elevated values of siderite (an iron carbonate formed under anoxia). We interpret this lithotype as representative of periods with a very high sedimentation rate and erosion and low in-lake primary productivity.

Lithotype 2 (Fig. 5 and Fig. 6, green) has an intermediate SR and erosion indicators are near average (with Fe above average). Here, vivianite (an iron phosphate formed under anoxia) and P are highest together with above average anoxia indicators. TChl flux is above average, however diatoms remain low (Si/Ti, BiO). Other indicators of aquatic productivity (HI, Br) stay on average as well as LOI, TOC, and BiM. Hence, this lithotype is interpreted as time periods of elevated SR, rather non-diatomaceous primary productivity, and anoxia.

Lithotype 3 (Fig. 5 and Fig. 6, red) is constrained by high erosion indicators (except Fe) and physical weathering (high K/Al and OI, low Rb/K). SR, productivity indicators and anoxia indicators are low. However, we observe frequently the presence of vivianite, siderite, and pyrite (an iron sulphide) which are all formed under anoxia. Diatoms show average values; however, benthic diatoms are abundant whereas planktonic diatoms are not frequent (Ramrath, 1997). We interpret this lithotype as indicative for phases of low SR and productivity. Sediment is dominated by clastic material and anoxia is likely at the very lake bottom.

Lithotype 4 (Fig. 5 and Fig. 6, black) shows a low SR and erosion indicators while chemical weathering is dominating (high Rb/K). Productivity proxies (TChl flux, Br, Si/Ti, BiO, HI) are high, P is above average, and the sediment is biogenic (high TOC and BiM). Also, anoxia indicators are above the mean. Thus, we understand that lithotype as a phase of low SR and erosion with high chemical weathering and productivity. Anoxia might have reached the photic zone.

Lithotype 5 (Fig. 5 and Fig. 6, purple) is dominated by very high productivity indicators, chemical weathering, and very low erosion indicators. P is lowest and diatoms (Si/Ti, BiO) are highest. Anoxia proxies show an elevated level together with pyrite. Therefore, that lithotype shows us time periods with high diatomaceous productivity, under low erosion and persistent anoxia, reaching the photic zone. Sedimentary P is very low indicating poor preservation and possibly a high P content in the water (processes are discussed in chapter 6.2).

5.3 Proxy-proxy calibration and lake evolution

Primary productivity and lake stratification are important processes in lakes. We inferred these processes based on sedimentary pigments. Therefore, we used proxy-proxy calibrated RABD indices based on HSI. We measured the pigment concentration of 38 samples as well as the RABD index at these locations. For Bphe we measured concentrations from 0 to 19.1 $\mu g/g_{\text{dry sediment}}$ in these samples. The Bphe proxy-proxy linear regression model ($Bphe = 508.94 * RABD_{845} - 503.62$) showed an R^2 of 0.69 ($p < 0.01$) and a 10-fold cross-validated root mean square error of prediction (RMSEP) of 3.38 $\mu g/g_{\text{dry sediment}}$ (19.06%). For TChl we measured concentrations from 0.3 to 305.2 $\mu g/g_{\text{dry sediment}}$ in these samples. The TChl proxy-proxy linear regression model ($TChl = 1527.7 * RABD_{655\text{-}685max} - 1625.7$) showed an R^2 of 0.79 ($p < 0.01$) and a 10-fold cross-validated RMSEP of 47.3 $\mu g/g_{\text{dry sediment}}$ (15.88%). This model underestimates the TChl concentrations in dark areas (low Rmean). Therefore, we calculated TChl over a shape constrained additive model (SCAM) as well. This model was more accurate than the linear regression model in areas of a low Rmean. However, over the entire core it did not improve the calibration. Therefore, we used the linear regression model. A comparison of the two models is shown in the annex D2. Shapiro–Wilk and the Kolmogorov–Smirnov tests show that residuals of both linear regression models are most likely normally distributed ($p>0.05$ on test for non-normality).

We identified eight CONISS zones (units) in the entire core based on our scanning-proxy dataset. The units help us to structure the results in time. In the following, we present the evolution of our scanning proxies

from the bottom to the top. This allows us to make inferences about the evolution of the lake ecosystem at very high resolution (5 mm).

Unit 1 (1191-993 cm, 18.4-14.1 ka BP) is the oldest CONISS zone and represents the Late Glacial. This unit has a low SR (0.5 mm/yr). Erosion indicators and catchment minerals are high (Ti, R850R900, K, Si, Fe, MS). The MS peak is related to the Randazzo/Polverello tephra. Physical weathering is dominant (high K/Al, low Rb/K). TChl concentrations and fluxes bellow the detection limit as well as very low Br counts indicate nearly absent in-lake primary productivity. Interestingly, Br counts are slightly elevated where organic detritus layers are visible (between 1095 cm and 1050 cm) and clastic input is slightly higher. Probably a few diatoms were supported in this time period (low Si/Ti, sediment description). Anoxia indicators (Bphe, (Fe/Ti)/Mn) show very low values. In contrast, diagenetically formed vivianite is quite abundant in the lowermost, part of this unit. That might indicate anoxic conditions in the sediment. Thus, the Late Glacial is shaped by a low SR, clastic sediment, and very low productivity.

Unit 2 (993-879.5 cm, 14.1-11.2 ka BP) contains a first section (until ca. 13 ka BP) with reduced erosion proxies and catchment minerals. Here, production indictors (TChl, Si/Ti, Br) increase and the sediment gets more organic but stays a silty clay (sediment description). Anoxia indicators elevate slightly and vivianite is present. However, Bphe remains below the detection limit. A second section (after ca. 13 ka BP) shows again higher erosion and catchment indicators, elevated physical weathering, and reduced productivity. Vivianite is less abundant and anoxia indicators reduce but stay at a higher level as before. The first section is the Bølling/Allerød with reduced clastic material, elevated productivity and possibly anoxia which, however, stays bellow the photic zone. In the Younger Dryas (the second section), we observe a return to more clastic material and low productivity.

Unit 3 (897.5-812.5 cm, 11.2-9.4 ka BP) shows a clear trend. Erosion indicators and catchment minerals decrease steadily whereas increasing chemical weathering is indicated by rising Rb/K (and low K/Al). Throughout the section production indicators (TChl and Si/Ti) progressively elevate. Interestingly, Br peaks at the start of the unit and shows next a downward trend. Also, P shows a similar behaviour. P peaks first to very high levels and then decreases as Bphe increases clearly over the detection limit. Laminations are present throughout the unit (varve type 2) and are better preserved where Bphe is high. Thus, in the early Holocene, anoxia was present and certainly reached the photic zone in the Boreal (after 10.2 ka BP). Meanwhile, clastic materials decreased, and productivity increased.

Unit 4 (812.5-708.5 cm, 9.4-7.4 ka BP) has a unique biogeochemical signature (lithotype 5). Here, erosion proxies and catchment minerals are lowest. The unit shows the highest Rb/K and lowest K/Al ratios, indicating strong chemical weathering. Production indicators (TChl and Br) are high and Si/Ti is peaking. P shows very low values whereas Bphe reaches peak concentrations (max 24 $\mu g*g^{-1}$). Flux rates only show a weak peak and reflect still low SR. Sediments are continuously laminated. Thus, unit 4 is characterised by prolonged anoxia while diatomaceous production is dominating over catchment input.

Unit 5 (708.5-528 cm, 7.4-3.9 ka BP) starts with a short section of high catchment input (erosion indicators and catchment minerals) and low productivity. Similar patterns, with different magnitude, are observed seven other times in that unit. Overall, erosion indicators and catchment minerals are quite low. TChl concentrations peak in the Neolithic case-study section (until 598 cm). Also, Br and Si/Ti show an increased production compared to the section after 598 cm. This is less pronounced in the TChl fluxes. Throughout the unit Bphe fluxes and concentrations are increasing and mostly above the detection limit. (Fe/Ti)/Mn shows a similar behaviour and vivianite is increasingly present in the second section. The unit has a high

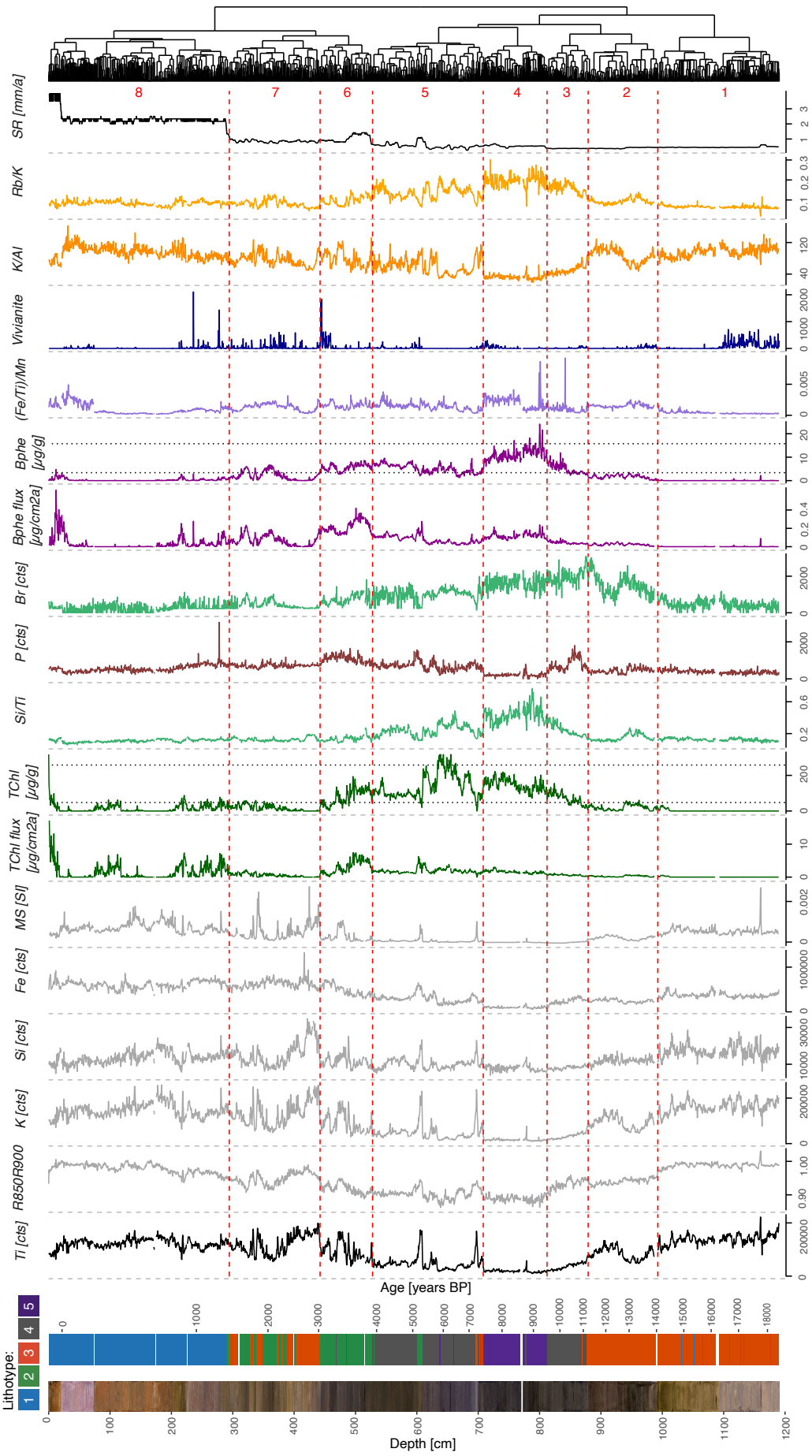

Fig. 7: Evolution of scanning-proxies. Red numbers and red dashed lines indicate the unit. Black dotted lines show the TChl and Bphe calibration range. Ages are given in calibrated years BP (before 1950). The depth refers to the sediment depth of the master core (masterdepth).

productivity, low catchment input and anoxia that possibly reached the photic zone. However, there are distinct phases of high catchment input where anoxic and productivity indicators drop.

Unit 6 (528-442.5 cm, 3.9-3 ka BP) begins with the Avellino tephra (524 cm) and is characterised by an increasing trend of P and highly variable catchment input. In contrast, mean flux rates for TChl and Bphe are highest at the start of this unit and decline thereafter. This feature is well visible in the other production indicators. Bphe concentrations and (Fe/Ti)/Mn remain, however, rather stable; laminations persist and vivianite is very abundant at the end of the unit. Thus, the unit is shaped by increasing catchment input, decreasing productivity and anoxia reaching the photic zone. Superimposed on these trends are phases of high catchment input like in unit 5.

Unit 7 (442.5-294.5 cm, 3-1.3 ka BP) is dominated by high clastic input (erosion proxies and catchment minerals). However, the unit has two distinct biogeochemical signatures. There are phases of high clastic input, low production indicators, and low Bphe values (lithotype 3) and vice versa (lithotype 2). Hence, the section contains a high clastic share. However, in phases of reduced clastic input we observe anoxia up to the photic zone. Interestingly, the 6 cm thick bed at 327 cm is quite low in clastic material.

Unit 8 (294.5-0 cm, 685-2019 CE) is dominated by high SR of over 2mm/a and high values for erosion indicators and catchment minerals (clastic input). Also, physical weathering is most common (high K/Al, low Rb/K). Clastic input drops in the last 25 cm. TChl stays bellow the detection limit. However, this is different from the unit start to 219 cm, from 117 to 75 cm, and in the topmost 17 cm. Here, TChl concentrations stay around 40 μg/g. Furthermore, at the very top (0-1 cm) we spectrophotometrically measured a concentration of 38.2 μg/g TChl. This contradicts with the HSI estimate (over 100 μg/g). The very high water content in the last 6 cm is a possible explanation for the too high TChl estimate. The elevated values before seem to be a real feature and agree with work from Julieta Massaferro (1994). Bphe follows the pattern of TChl until 219 cm. Afterwards, it remains very low and only peaks at 12 cm to then decrease again. This is in line with spectrophotometer results (0.4 μg/g Bphe at 0-1 cm). (Fe/Ti)/Mn and vivianite show a similar pattern as Bphe. Laminations are present from 30 cm on. At 17 cm, they get thicker (when TChl increases) and change to 1-cm-thick beds. We therefore propose that anoxia was present until 219 cm and after 70 cm. However, it probably only reached the photic zone from 25 to 7 cm (1938-1997 CE).

5.4 Lake, catchment and climate interactions

5.4.1 Lake ecosystem

We identified the main interactions in the lake ecosystem for different time periods by applying a principal component analysis on the scanning-proxy dataset. First, we analysed interactions before the Neolithic with unlikely human interference (CONISS zones 1-4). The PCA of the natural state (Fig. 8) revealed one significant PC that explains 71.7% of the variance. PC1 shows a positive loading for all proxies connected with clastic input (Ti, R850R900, K, Si, Fe, MS) and physical weathering (K/Al). They are mainly associated with lithotype 3. Proxies connected to productivity (TChl, Si/Ti, Br), chemical weathering (Rb/K), and anoxia (Bphe, (Fe/Ti)/Mn) show negative loadings for PC1. They are dominating in lithotype 5 and, to a lesser degree, in lithotype 4. SR stays very low and stable in this section. Hence, it is not impacting the variance. Vivianite and P are more associated with catchment input but they cannot be explained well by PC1; there are other more relevant processes (e.g. visible in PC2, not significant) guiding their variation (28.3% of the variance is not explained by PC1).

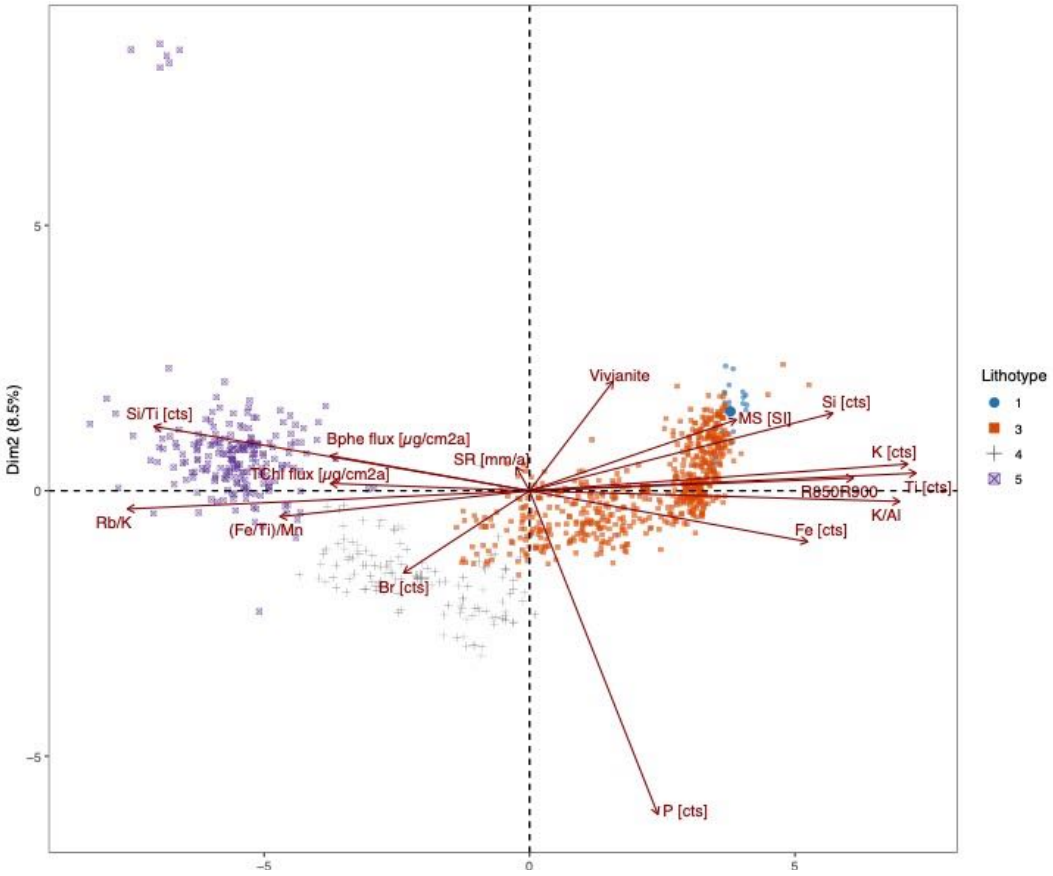

Fig. 8: PCA biplot (axis 1 and 2) on the natural time period based on the scanning-proxy data set.

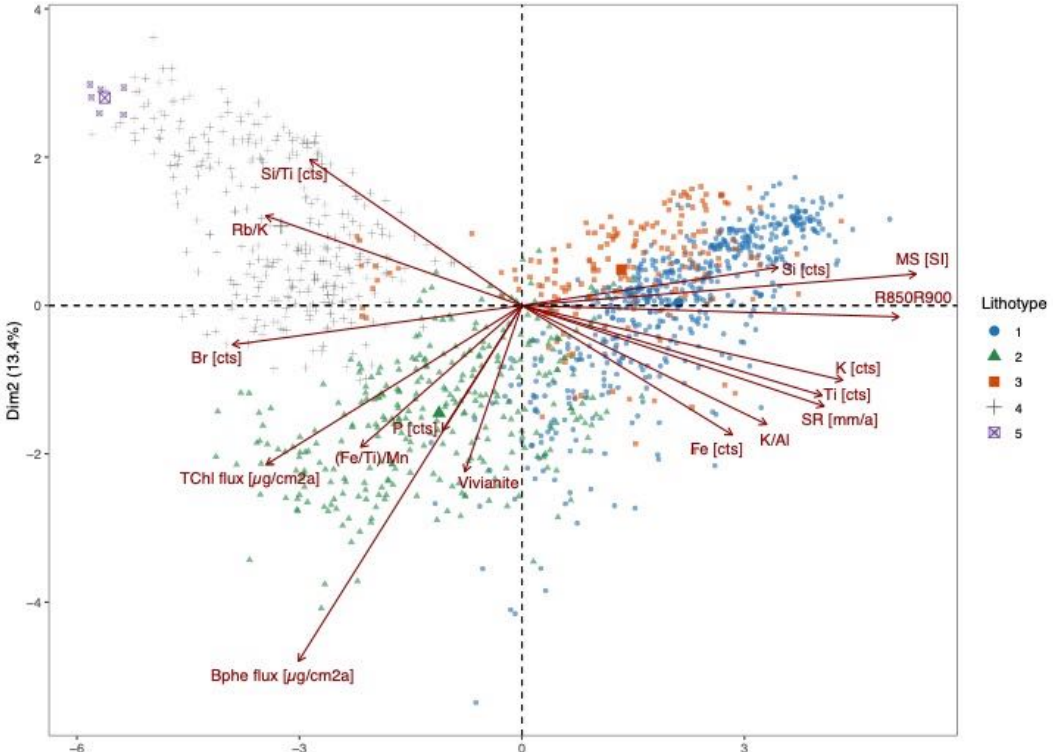

Fig. 9: PCA biplot (axis 1 and 2) on the human time period based on the scanning-proxy data set.

Second, we analysed the relationships in the lake ecosystem since the Neolithic, where human influence was detected (CONISS zones 5-8). This PCA (Fig. 9) revealed one significant PC that explains 48.3% of the variance. All indicators for clastic input and physical weathering show positive loadings with PC1. Furthermore, the SR is as well positively correlated with clastic input. These processes dominate lithotype 1 and 3. All other proxies show negative loadings with PC1. Here, things are more complex. Variations in Br are best explained by PC1, followed by chemical weathering (Rb/K) and the other productivity indicators (TChl and Si/Ti). However, TChl and Si/Ti are nearly uncorrelated. Also, anoxia indicators, P and vivianite are not well caught by PC1. Especially, Bphe is connected to PC2 (not significant). Hence, non-clastic input indicators are heavily influenced by other processes (51.7% of the variance is not explained by PC1). Thus, the interactions got more complex with the presence of humans.

5.4.2 Lake-catchment-climate

The lake-catchment-climate interactions were accessed for the same two time periods by applying a principal component analysis on the full multi-proxy dataset. However, the first PCA (natural state) only covers the section from 1096 cm to 708 cm (n=59). Below 1096 cm not all datasets are available. Also, human indicator pollen (different meaning in this section) and dryness (CC26 hydro index, only available above 907 cm) are excluded (explanations in chapter 3.3. and 4). The second PCA (under human influence) has a reduced extent as well. It covers only the section from 708 to 145 cm (n=62). There is no information on dryness above 148 cm. Used variables are given in Table 2.

The first PCA (natural state, Fig. 10) has only one significant principal component (PC) which explains 59% of the variance. It shows positive loadings for erosion indicators (Ti, OI), non-arboreal pollen (NAP) and high lake levels. In contrast arboreal pollen (AP), July temperatures, as well as production (Si/Ti and TChl) and anoxia (Bphe, (Fe/Ti)/Mn) indicators have negative loadings. The PC1-PC2 space confirms above image. However, P is anticorrelated with charcoal and anoxia indicators. MAR (mass accumulation rates) and vivianite do not have much influence on the variance of the PCA.

The second PCA (Fig. 11 and Fig. 12) covers the section since the Neolithic (human interference) and has three significant PCs. PC1 explains 38.2% of the variance. Production and anoxia indicators show positive loadings whereas catchment input, MAR, human indicators, and high lake levels show negative loadings. PC2 describes 15% of the variance. Here, positive loadings were observed for human indicators, open landscape, TChl, and Bphe. OI and dryness (CC26 hydro index) have negative loadings. PC3 explains 12.6% of the variance and is dominated by vivianite. Also, Bphe, and clastic input show positive loadings. In contrast, production indicators are negatively associated with PC3. In the PC1-PC2 space we observe elevated Bphe, TChl, and P with a lower lake level. Catchment input (Ti, MAR) is anti-correlated with forest cover, Si/Ti, and (Fe/Ti)/Mn. Charcoal, vivianite, and summer temperature have no big impact on the variance. In the PC1-PC3 space vivianite is dominating PC3 and correlated with P and anoxia. MAR, human indicators, and higher lake levels are anti-correlated with anoxia, P, and forest cover. Summer temperature and charcoal have no big influence on the variance of the PCA.

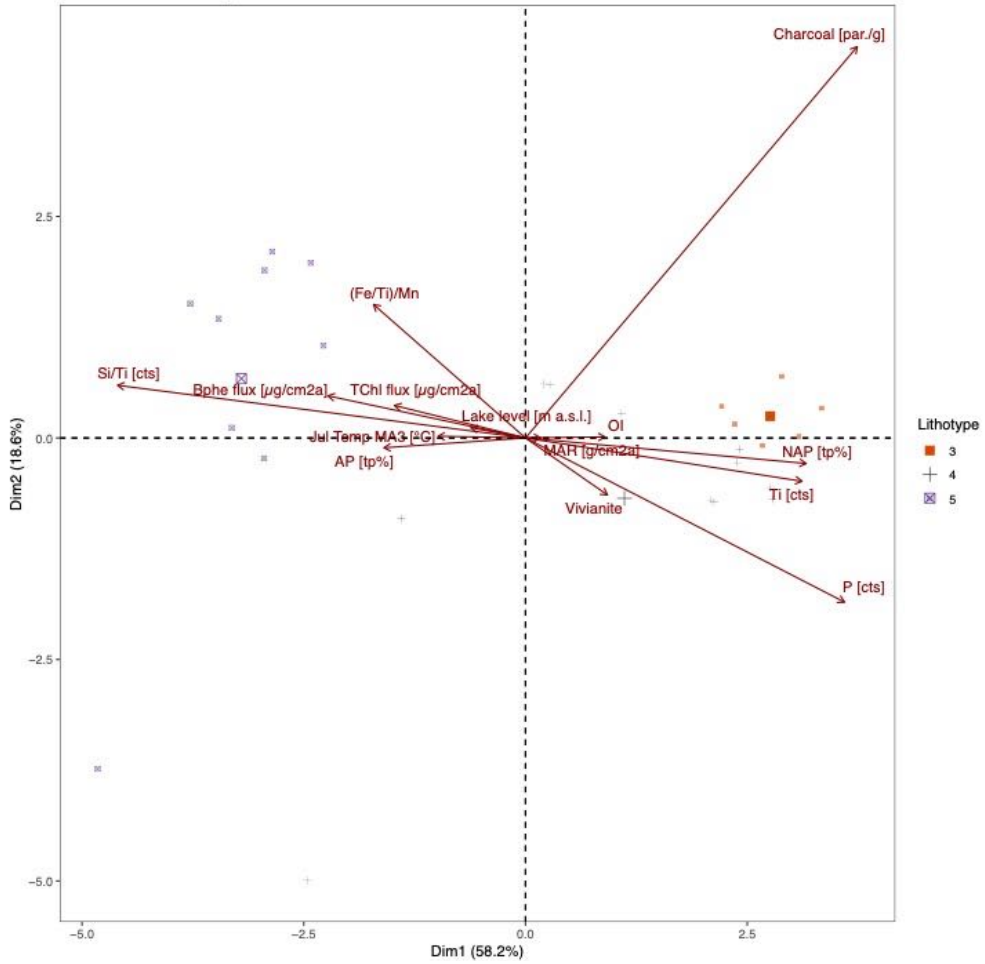

Fig. 10: PCA biplot (axis 1 and 2) on the natural time period based on the full multi-proxy data set.

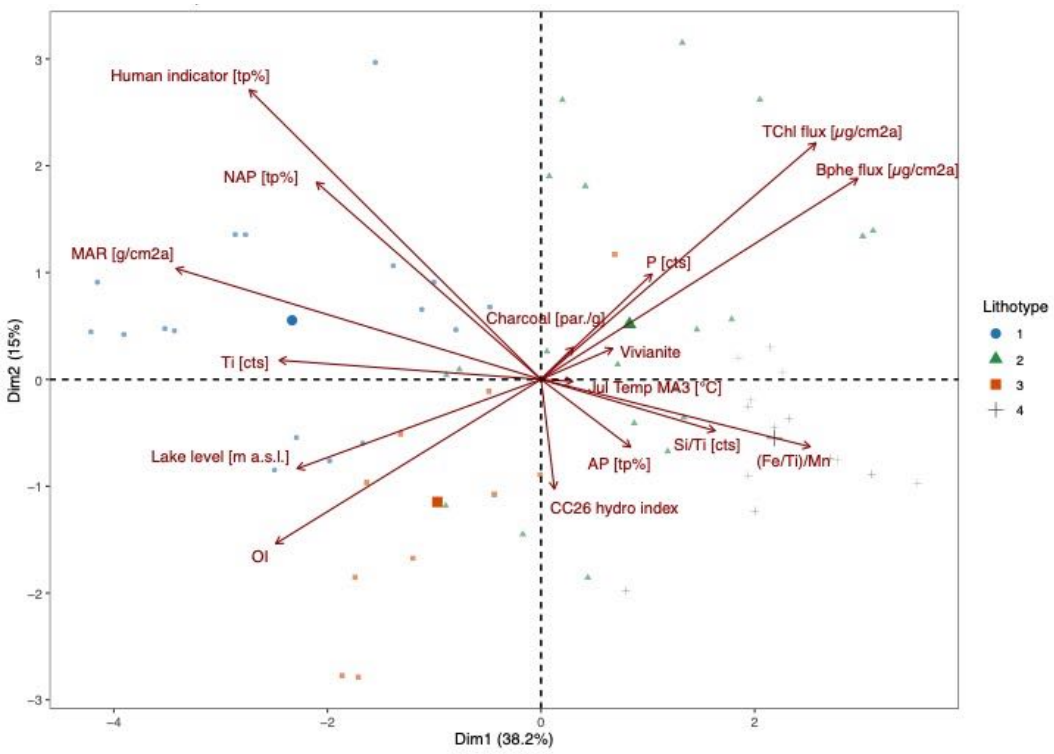

Fig. 11: PCA biplot (axis 1 and 2) on the human time period based on the full multi-proxy data set.

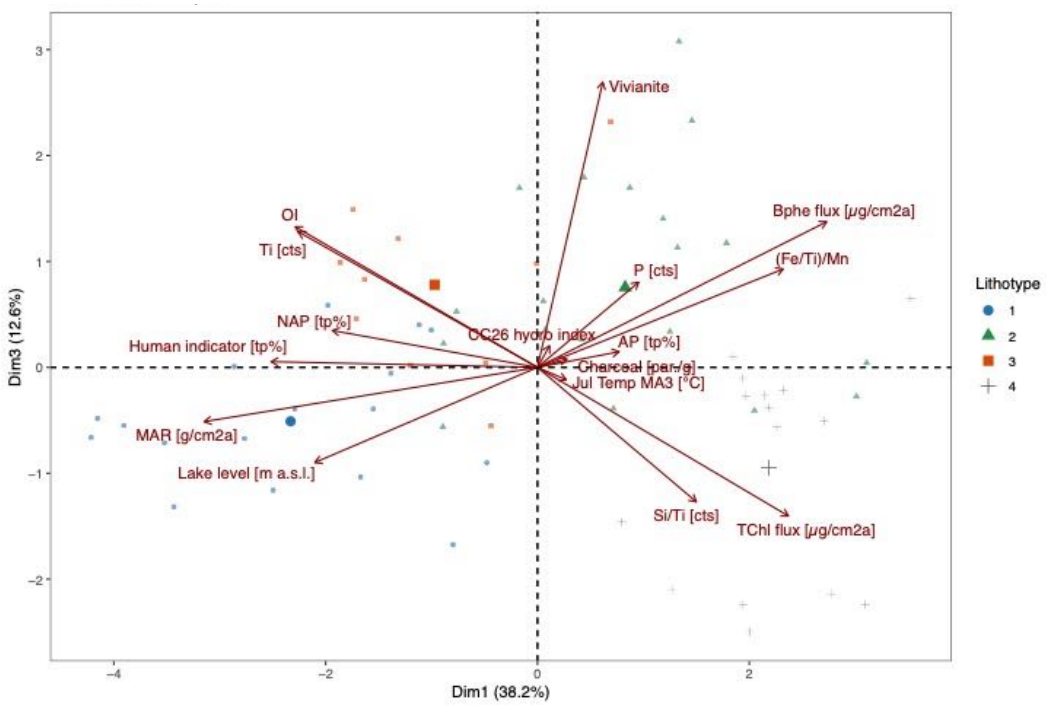

Fig. 12: PCA biplot (axis 1 and 3) on the human time period based on the full multi-proxy data set.

5.5 Lake response to landscape evolution and climate change

We identified the influence of erosion, hydrology, land cover, vegetation changes, fire dynamics, anthropogenic impact, and climate on the lake for the same two time periods using the same variables as in the above PCAs (chapter 5.4.2). The first redundancy analysis (RDA) shows that the catchment and climate variables explain 58.2% of the lake variance for the period with unlikely human interference (R^2_{adj} suggests an explained variance of 51.6%). The first two RDAs explain already 54.8% of the variance (RDA 1 = 46.1% and RDA 2 = 8.6%). Most important explanatory variables for RDA 1 are Ti (17.3%) and NAP (17.4%). Most of the variance of RDA 2 is explained by AP (19.8%), OI (19.7%) and lake levels (16.4%). The RDA 1-2 space groups the lithotypes in different areas. Lithotype 5 correlates with high temperatures, and high forest cover. Lithotype 4 is in between lithotypes 3 and 5.

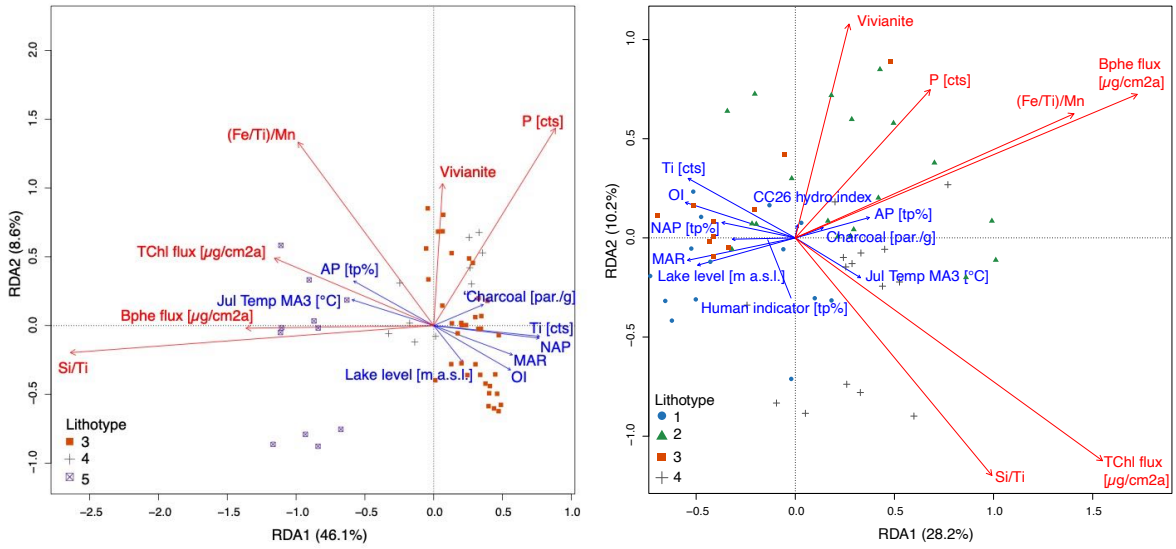

Fig. 13: RDA triplots of the natural time period (left panel) and the human time period (right panel). In blue are the explanatory variables and in red the dependent variables.

In the RDA for the human period, catchment and climate variables explain 49.6% of the variations in the lake properties (R^2_{adj} suggests an explained variance of only 39.8%). However, 38.4% are already explained by the two first RDAs (RDA 1 = 28.2% and RDA 2 = 10.2%). Catchment input (OI = 15.1%, MAR = 14.8%, Ti = 14.7%) and lake level change (13.4%) are the most important drivers of RDA 1. RDA 2 is dominated by catchment input (Ti =24.3%, OI = 12.5%) and summer temperature. The RDA 1-2 space shows a less pronounced grouping of the lithotypes. This is in line with the lower explained variance compared to the natural phase. Nonetheless, lithotype 1 is associated with high MAR, OI, and with lake levels. In contrast, lithotype 2 is correlated with low lake levels, closed forest, and rather dry climate. Lithotype 3 is like lithotype 1 but has slightly more clastic input whereas lithotype 4 is related to high temperatures and low catchment input.

5.6 Case-study sections

5.6.1 Neolithic lake-landscape evolution and interactions

We took a closer look at the lake-landscape evolution (Fig. A 12) in the Neolithic to better understand how interactions and dependencies work on a higher resolution (5 mm). The case-study section is dominated by lithotype 4 (see sediment description). In general, we observe low clastic input indicators (Ti) and elevated chemical weathering (Rb/K), productivity (TChl, Si/Ti), and anoxia indicators (Bphe, (Fe/Ti)/Mn). Arboreal pollen (AP) stay most of the time above 80%, indicating closed forest. Superimposed on that general image, we observe several time periods with higher clastic input, physical weathering (K/Al), and lower productivity indicators. Also, for these events, anoxia indicators are reduced under low sedimentation rates (SR<0.6 mm/a). At the same time, we observe lower AP pollen and increased human indicators. Interestingly, *Alnus* shows a peak at around 7 ka BP, disappears, and comes back at 6.5 ka BP.

A principal component analysis (Fig. A 13) revealed two significant PCs that describe the mean interactions over the Neolithic. PC1 explains 43.4% of the variance. Positive loadings were observed for Ti, non-arboreal pollen (NAP), P, and human indicators. Negative loadings are dominated by diatom production (Si/Ti), chemical weathering (Rb/K) and AP. PC2 explains another 20.9% of the variance. Here, elevated anoxia indicators, TChl flux, and SR show positive loadings and contribute most to PC2. Furthermore, the PC1-2 space shows a correlation of high NAP and human indicator pollen with clastic input indicators. High AP are correlated with high (Fe/Ti)/Mn as well as with Si/Ti. Pollen indicators show no correlation with the SR and Bphe fluxes.

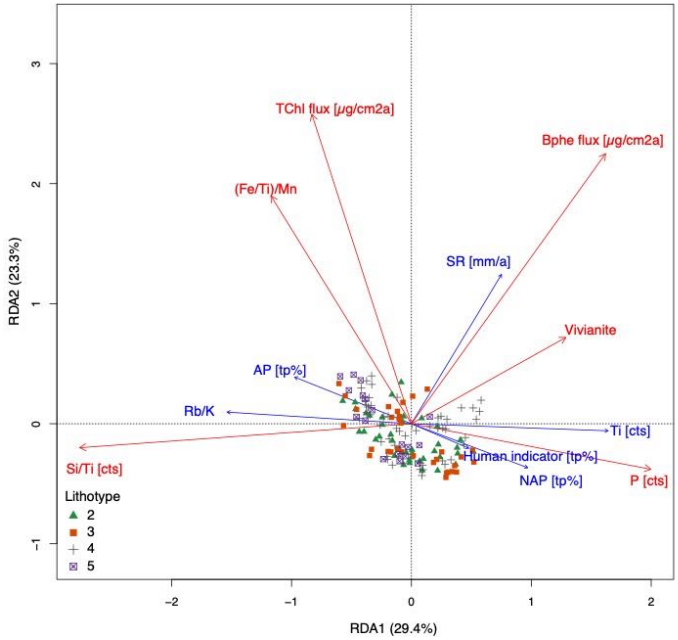

Fig. 14: RDA triplot of the Neolithic case-study section. In blue are the explanatory variables and in red the dependent variables.

We accessed the influence of the catchment on the lake properties (Fig. 14). The RDA shows that the catchment variables explain 56.7% of the lake variance (R^2_{adj} suggests an explained variance of 55.2%). The first two RDAs describe already 52.7% of the variance (RDA 1 = 29.4% and RDA 2 = 23.3%). Ti (25.8%), Rb/K (24.2%), AP (15.3%) and NAP (15.3%) are the most important variables for RDA 1. In contrast, most of the variance of RDA 2 is explained by SR (52.7%), AP (16.5%) and NAP (15.5%). Lithotype 4 dominates the Neolithic period and is placed at the centre of the RDA 1-2 space. Lithotype 5 is associated with high AP and chemical weathering whereas lithotype 3 shows high SR. High NAP, human indicator pollen, and Ti are associated with lithotype 4. Furthermore, variations in TChl flux are not well described by the explanatory variables but linked the most to AP and SR.

5.6.2 Bronze Age

The Bronze Age case-study section is completely laminated. However, shape, colour, and preservation vary a lot. Our, ultra-high-resolution scans (25 and 50 µm) suggest some sections to be varves. Indeed, Ramrath (1997) described the entire section as varved. We found two types of laminations which are differently preserved. A first lamination type (from 324 to 440 cm, see sediment description and Fig. 15) was described by Ramrath (1997) as varve type one and has a spring / summer layer formed by diatoms (Ramrath, 1997). This is clearly visible as the TChl peaks (and to a lesser degree in Si/Ti and Br). With or after the diatom bloom comes a peak in Bphe showing anoxic conditions. Next, we observe a higher clastic content (Ti and R850/R900) which we interpret as autumn/winter layer. A second lamination type (from 440 to 492 cm, see sediment description and Fig. 15) was described by Ramrath (1997) as varve type two. Here, the laminations are much brighter and have very low TChl concentrations. Likewise, Si/Ti and Br counts are lower. In contrast, Ti counts and the R850/R900 ratio are on a similar level as in the first lamination type. This confirms a lower biogenic component in these laminations as described by Ramrath (1997). Bphe concentrations remain below the detection limit. Because of the bad preservation of these lamina, we cannot distinguish different years.

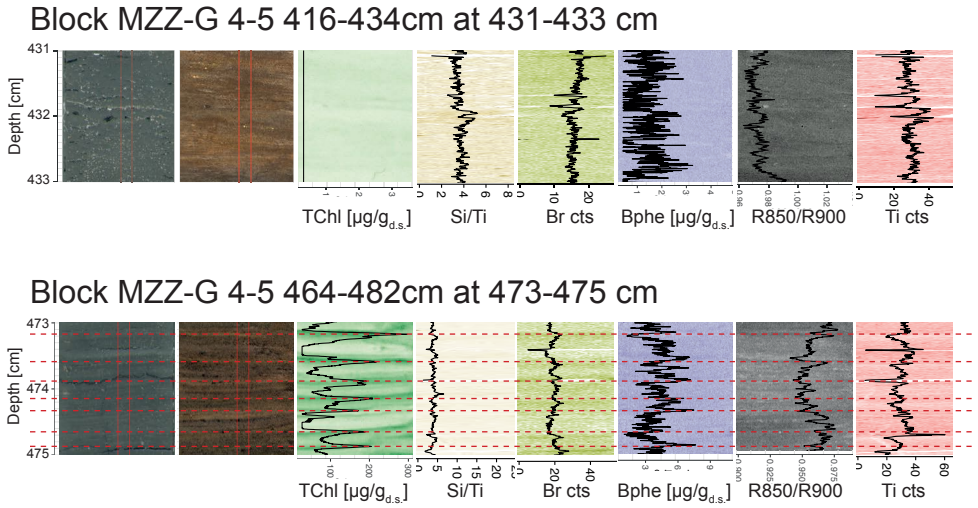

Fig. 15: Ultra-high-resolution HSI and µXRF scans for two segments of the Bronze Age case-study section. The upper panel shows worse preserved laminations (described as varve type 2 by Ramrath, 1997) whereas the lower panel shows better preserved laminations (described as varve type 1 by Ramrath, 1997). From left to right we see: SmartCIS colour image of the resin block, HSI colour image of the fresh block, TChl concentrations, Si/Ti, Br, Bphe concentrations, R850/R900, and Ti. The red lines in the lower panel show the potential spring/ summer layer of a respective year. The depth referes to the sediment depth of the master core (Masterdepth).

6 Discussion

6.1 Environmental reconstruction of Lago di Mezzano

In this section we present the environmental reconstruction of Lago di Mezzano. Eight units are numbered from the bottom to the top of the core and structure this chapter. The CONISS zones (units) are based on constrained clustering of the variables in the scanning-proxy data set (see chapter 3.3) and are the same as in Fig. 7. The discussed data are shown in Fig. 16. Processes are described in more detail in chapter 6.2.

Unit 1 (1191-993 cm, 18.4-14.1 ka BP)
Our sedimentary record starts at 18.4 ka BP (1191 cm) in the Pleistocene. The cold and dry glacial climate only supported *Artemisia* steppe (tundra). At that time, Lago di Mezzano had a lake level of 447-449 m a.s.l. (Giraudi, 2004). Since the lake only forms a natural outflow at a lake level of 454 m a.s.l. (Giraudi, 2004), this implies that Lago di Mezzano was endorheic. Sedimentation rates were very low and dominated by clastic inputs from the catchment. Ramrath et al. (1999a) reported very low organic matter and total organic carbon contents which are mostly of terrestrial origin (high OI; Wilkes et al., 1999). Also, only very low in-lake primary productivity was supported and probably restricted to the shallow beach areas as benthic diatoms are more common than planktonic groups (Ramrath et al., 1999a). Under low productivity aerobe respiration of organic matter is low and hence, oxygen use was low. This is in line with very low anoxic indicators. Therefore, we suggest the dominance of oxic conditions in the hypolimnion. The co-occurrence of iron-oxides, vivianite, pyrite, and siderite (formed under anoxia) can be explained by a diagenetic formation in the sediment.

At 15.4 ka BP *Pinus* trees expand into a landscape dominated by *Artemisia* and *Poacea*. Sadori (2018) interpreted this replacement of the *Artemisia* steppe as an increase in humidity. That can be explained by stronger westerlies due to a higher north-south temperature gradient (Francke et al., 2021). According to Francke et al. (2021), southern Europe got warmer while northern Europe's ice sheets lingered under the influence of the Heinrich event 1. As a result, the stronger westerlies carried more humid air masses to Italy and let the lake level of Lago di Mezzano rise to 458 m a.s.l. making it exorheic (Giraudi, 2004). Furthermore, increased humidity on the unstable slopes led to slightly increased erosion and detrital input. Also, a higher input of organic matter from terrestrial origin (high OI) was documented by Wilkes et al. (1999).

Unit 2 (993-879.5 cm, 14.1-11.2 ka BP)
With the onset of the Bølling/Allerød at 14.7 ka BP the climate ameliorated, got more humid (Francke et al., 2021), and vegetation cover increased. *Pinus* was replaced with *Quercus robur* and *Corylus* trees (Sadori, 2018). Increased vegetation cover stabilised the slopes in the catchment and reduced soil erosion, as indicated by clastic input indicators. At the same time, the warmer temperatures and increased nutrient supply, due to chemical weathering, stimulated a higher primary productivity. This is in line with an increased autochthonous (in-lake) origin of organic matter and the occurrence of planktonic diatoms living in the open water (Ramrath, 1997; Wilkes et al., 1999). Synchronously, we observe more extensive anoxic conditions at the lake bottom. This decrease of oxygen can be explained by different processes. First, lake stratification might have enhanced due to higher forest cover, higher lake levels, and summer warmth driving thermal stratification. Second, lower oxygen availability might be explained by the reduced solubility of oxygen in warmer water and higher aerobic respiration due to increased productivity. These processes are explained in detail in the next chapter (6.2).

Our production indicators show that this trend to increased productivity was interrupted from 13 ka BP to 11.5 ka BP with a return to a colder and drier climate (Francke et al., 2021). Indeed, this return to glacial conditions in the Younger Dryas led to a comeback of benthic diatoms and lower nutrient availability.

Furthermore, the lake level was probably lower as evidenced by a hiatus in the LMZ-G core at the lake shore and an erosion surface at 448 m a.s.l. (Giraudi, 2004; Ramrath, 1997). On land, *Artemisia* and *Poacea* increased suggesting open vegetation and soil erosion (Sadori, 2018). This is in line with our observed increase in clastic input and physical weathering. A documented higher dry density and a lower organic content of increasingly terrestrial source further support these findings (Ramrath et al., 1999a; 2000; Wilkes et al., 1999).

Unit 3 (897.5-812.5 cm, 11.2-9.4 ka BP)

Unit 3 is shaped by the early Holocene warming beginning at 11.5 ka BP. Interestingly, lake levels remained low (Giraudi, 2004). That can be explained by a continued lack of humidity due to a blocking of the westerlies in the Mediterranean and an increased summer insolation forcing (Laskar et al., 2004; Magny et al., 2013). The warmer climate supported a mixed deciduous oak forest, dominated by *Quercus robur* and *Corylus*. This vegetation cover increased soil stability and reduced erosion resulting in low clastic input. Also, the constantly rising temperatures and the connected increased nutrient input boosted primary production. Planktonic algae became abundant and biogenic material was of autochthonous origin (Ramrath et al., 1999a; 2000; Wilkes et al., 1999). At the same time, we observe a growing anoxic zone which certainly reached the photic zone in the Boreal (after 10.2 ka BP). The increase of purple sulphur bacteria is in phase with a reduction in phosphorus (P). This can be explained by an increased nutrient uptake by primary producers (Wetzel, 2001) as well as increased dissolution and P-recycling in the anoxic bottom waters (Tu et al., 2019, see chapter 6.2). That shift to high production and low oxygen is also reflected in the sediment which changes to a laminated diatomaceous ooze (biogenic matter > 50%).

Unit 4 (812.5-708.5 cm, 9.4-7.4 ka BP)

Around 9.4 ka BP the mixed deciduous oak forest gets dominated by *Fagus* (Sadori, 2018). This is also the time when stalagmites record an increasingly drier climate

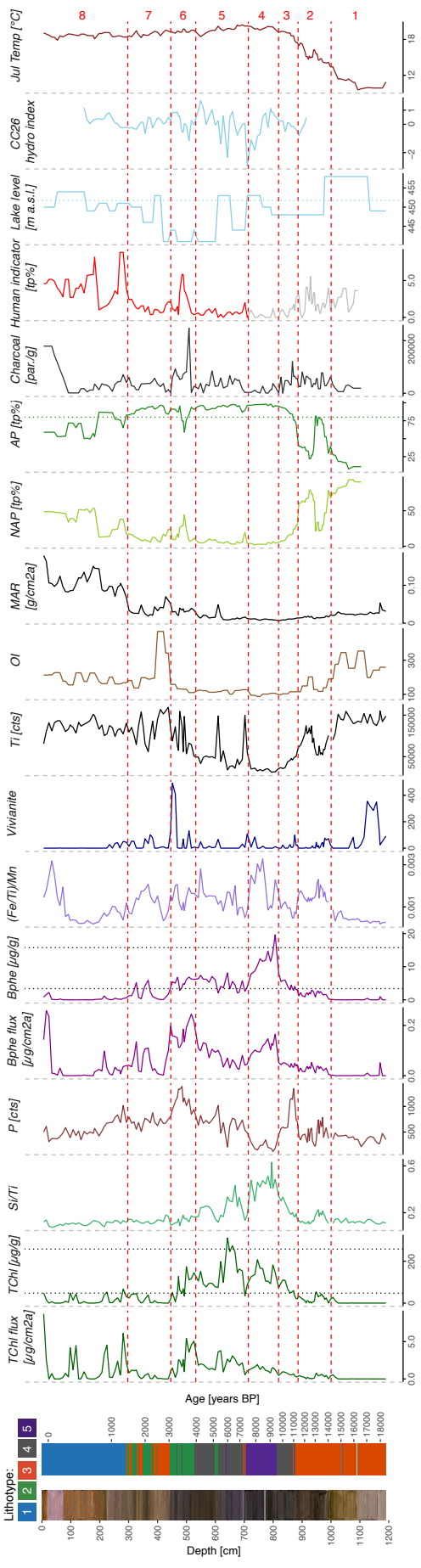

Fig. 16: Evolution of the variables from the full multi-proxy data set. Red numbers and red dashed lines indicate the unit. Black dotted lines show the TChl and Bphe calibration range. The green dotted line indicates 80% AP and the blue dotted line depicts a lake level of 452 m a.s.l. The invalid section of human indicator pollen is in grey. Ages are given in calibrated years BP (before 1950). The depth refers to the sediment depth of the master core (masterdepth).

(Regattieri et al., 2014) which might have reduced the lake level, similar to Lago dell'Accesa (Magny et al., 2007). However, such a change is not visible in the lake level record of Lago di Mezzano which has a lower temporal resolution and remained between 448 and 450 m a.s.l. (Giraudi, 2004). The landscape was very stable as evidenced by the lowest recorded clastic input values and the strongest chemical weathering. Production was high, and especially diatoms thrived with Si/Ti showing the highest values of the record. Our data supports the presence of a very extensive anoxic zone during that time. The increased presence of purple sulphur bacteria might not only be linked to a more extensive anoxic zone but also to a lower lake level. That might be the case because a lower lake level will lead to a lowered photic zone while anoxia stays at the same depth due to the unique morphology of Lago di Mezzano (see chapter 6.2 and Fig. 20). Furthermore, our 83 μm HSI record (full resolution), which potentially resolves seasonal variations due to the presence of laminations, shows that Bphe concentrations stayed above the detection limit most of the time. This implies that anoxia up to the photic zone was present in a large share of the year or even permanent. Hence, the lake had a very limited mixing behaviour. At 8.8 ka BP we find a highly clastic light brown clay layer that indicates an erosion event. That event might be linked to a very short wetter period at that time (Regattieri et al., 2014). Next, from 8.3 ka BP to 7.2 ka BP, stalagmite data indicates a wetter climate (Regattieri et al., 2014), a direct link to the 8.2 event in the north Atlantic could not be established (Finné et al., 2019; Magny et al., 2013). This increased humidity led to similar or higher lake levels than today (Giraudi, 2004). Reduced purple sulphur bacteria are evidence that the photic zone got at least intermittently elevated above the chemocline. On land, we observe the expansion of *Quercus ilex* (an evergreen oak), which changed the composition of the previously deciduous *Fagus* and *Quercus robur* forest (Sadori, 2018).

Unit 5 (708.5-528 cm, 7.4-3.9 ka BP)

From 7.3 to 5.2 ka BP our high-resolution pollen record provides more detailed insight into the Neolithic landscape development. Thus, we discuss that part of the mid-Holocene thermal maximum in more detail.

At 7.3 ka BP, the climate became drier (Regattieri et al., 2014) and the lake levels were lowered to around 444 m a.s.l. (Giraudi, 2004). Thus, the erosive base of the now endorheic lake dropped and led to a very high clastic input until 7.2 ka BP. Simultaneously, on land, *Fagus* declined and led to forest opening. Also, less water demanding *Quercus robur* and *Corylus* took over. That open landscape, as well as the lower lake depth, allowed a better oxygenation of the lake as is evidenced by reduced anoxia indicators. At the same time, productivity indicators waned. This might be linked to increased P trapping (less nutrients available), or simply worse preservation because of bioturbation (sediments are massive). Dilution effects can be excluded as we use flux rates. On top of the drier climate, human indicator pollen imply a first human presence in the catchment. This is reasonable as the neolithisation in central Italy started already around 7.9 ka BP (Palmisano et al., 2021; Stoddart et al., 2019). Thus, a drier climate may have been the reason why this early Neolithic farmers came to the Caldera di Latera. It is likely that they had a role in reducing the forest cover to make space for agriculture. A reduction in forest cover is not observed at other lakes in the region (Sadori, 2018), providing evidence that the local forest opening at Mezzano was driven by human activity. High-resolution data on charcoal (a fire proxy) will clarify this in the future.

At 7150 years BP, we observe an increase in anoxia and productivity simultaneously to a decrease in human indicator pollen and the formation of a closed forest (AP > 80%). Also, we observe, for the first time, the presence of *Alnus*. That wetland taxa might indicate an expansion of swampy area and, thus, a higher lake level. Both wind shielding and a deeper lake favour lake stratification. The higher productivity might be related to feedbacks related to the anoxic conditions (see next chapter 6.2) or by an increased nitrogen (N) availability thanks to the presence of N-fixing Alder (Devotta et al., 2021; Goldman, 1961). Furthermore, the higher lake level, and the accompanied expansion of wetlands, might have been the reason why people left the lake. Next, between 6800 and 6600 years BP we observe a reduction in *Alnus*, possibly because of a lower lake level. A drier climate is also documented by recent high-resolution stalagmite data (Isola et al.,

2019). However, we also observe a general forest reduction, especially by *Fagus*. At the same time, increased human indicator pollen are evidence for human presence and likely a co-author in that change. Again, we observe a higher clastic input and a more limited anoxic zone. Productivity slightly drops but keeps a general increasing trend. The comeback of *Alnus* at 6600 years BP suggest a lake level increase. Giraudi's (2004) data indicates a lake level of 453 m a.s.l. and hence, the formation of an outflow. This is in line with a wetter climate (Isola et al., 2019). 150 years later, reduced *Fagus* and increased human indicators suggest a short period of human presence until 6400 years BP. However, this time the forest stayed closed, and humans had less impact on the lake. We do not observe increased clastic input. In contrary, we find increased production and anoxia. Concurrently, nutrient enrichment from N-fixing *Alnus* is likely. For the next 600 years there is no sign of human presence. In this time TChl concentrations were very high and reached their maxima. Anoxia reached at least seasonally the photic zone.

At 5750 years BP humans were again impacting the catchment. As in the previous phase, *Fagus* was heavily reduced, whereas the forest stayed likely closed. However, this time we observe high clastic input into the lake and reduced production as in the phases with open forest. Also, the extent of the anoxic zone possibly got reduced. Somehow, that forest reduction must have been strong enough to enable more wind shear on the lake and to increase erosion. After 5500 years BP *Fagus* slightly recovered and we got back to a more stable ecosystem. The end of the Neolithic case-study section (5200 years BP) is marked by a massive peak in clastic input like the one 2000 years earlier at the beginning of this unit. We link that erosion event to a lowering of the lake level due to drier climate (Giraudi, 2004; Isola et al., 2019; Regattieri et al., 2014).

Thereafter, in the now endorheic lake, TChl remained on a lower level than before whereas diatoms return to a similar level after the erosion event at 5200 years BP. Furthermore, anoxia steadily built up and occupied a larger share of the photic zone; probably because of the reduced lake depth and the closed forest (see chapter 6.2). A reduced lake level is likely connected to drier climate between 4500 to 4100 years BP, the so-called 4.2 event (Drysdale et al., 2006; Isola et al., 2019; Regattieri et al., 2014; Zanchetta et al., 2016). Next, an increase in humidity lead to slightly higher lake levels of the still endorheic lake (Giraudi, 2004; Isola et al., 2019; Regattieri et al., 2014). Clastic input stayed low throughout these changes. That indicates the presence of a resilient system with stable slopes thanks to high vegetation cover. Here, a high-resolution pollen record is still missing. Hence, we cannot give information about short-term human impacts.

Unit 6 (528-442.5 cm, 3.9-3.0 ka BP)

Around 3800 years BP the Avellino tephra was deposited in a relatively humid phase. Here, high chemical weathering supported a high production. Also, a dense forest protected the lake from wind shear and allowed an extensive and persistent anoxic zone. This is evidenced by a very high Bphe flux. At 3700 years BP, the climate got drier and the lake level dropped slightly to 441 m a.s.l. (Giraudi, 2004; Isola et al., 2019; Regattieri et al., 2014). At the same time, early Bronze Age settlers occupied the free beaches as made evident by three submerged pile dwellings on the north eastern shore (Conti et al., 1993; Petitti, 2000; Petitti & Mitchell, 1993; Sadori et al., 2004). Using fire, as demonstrated by high charcoal concentrations, they cleared the mixed oak forest and started agriculture. An increase in some synanthropic pollen and *sporormiella* spores indicates pastureland. That anthropogenic impact and the lowered erosion base led to increased clastic input impacting the lake ecosystem. The open landscape allowed for wind shear to be active on the lake surface. This enhanced lake mixing and decreased the duration and extent of the anoxic zone. Furthermore, primary production was reduced. This might be connected to a decrease in chemical weathering and nutrient availability (because of increased P trapping and less N-fixing *Alnus*). A worse pigment preservation is unlikely as the sediment is laminated and anoxia conditions are present. After 3300 years BP, the middle Bronze age settlements were abandoned because of rising lake levels (Franco, 1982). This increase in lake level is supported by higher *Alnus* counts (Sadori, 2018; Sadori et al., 2004) and probably a result of elevated

precipitation (Isola et al., 2019; Ramrath et al., 2000). Furthermore, increased forest cover stabilised the slopes which reduced soil erosion and enhanced lake stratification due to wind protection.

Unit 7 (442.5-294.5 cm, 3.0-1.3 ka BP)

In Unit 7 a second phase of land use exists at 3050-2900 years BP, as suggested by human indicator pollen and higher clastic input. However, land use was less strong, and the forest stayed closed. Archaeological finds support a changed use of the settlement for ritual purposes (Pellegrini, 1993; Sadori, 2018; Sadori et al., 2004). This second settlement phase was again accompanied by low lake levels, indicating a drier climate (Giraudi, 2004).

At the end of that settlement period, geomorphological evidence indicates a rising lake level to 453 m a.s.l. (Giraudi, 2004). That made the lake exorheic and much larger in area. Tree pollen remained high and supported lake stratification. However, anoxic conditions prevailed only at the lake bottom and no longer reached the photic zone due to the higher lake level (see chapter 6.2). Production is very low and clastic input remained high. This might be connected to negative temperature anomalies from 2800-2600 years BP (Wanner et al., 2011). Archaeological evidence suggests that people settled on defensive positions north and south of the caldera avoiding the lake shore for the next centuries (Di Gennaro, 1986). Nonetheless, Sadori (2018) suggests that humans were still active in the region as documented by cultivated fruit trees. Forests were dominated by *Quercus robur* and *Alnus* with *Fagus* reduced.

At 2500 years BP Etruscans settled in the region as evidenced by historical and archaeological data (Luzi & Scipioni, 1994; Sadori, 2018). At that time, we observe increased cultivation of *Juglans* and *Olea*. A reduction in AP is evidence for deforestation as the Romans conquered the area in the third century BCE (Sadori, 2018). The Romans started lake regulation to drain the swamp (Giraudi, 2004; Sadori, 2018). According to Giraudi (2004), they lowered the lake level to at least 446 m a.s.l. which reduced the lake surface and, for the first time, the size of the catchment. That is because a large part of the former catchment area no longer discharged into the lake but directly into the Olpeta river (Giraudi, 2004). Exactly at that time, we observe a reduction of catchment input, which can be explained by the much smaller catchment which is now only fed by very small inlets and groundwater (Giraudi, 2004). Also, the shallower lake increased the relative depth promoting lake stratification and a lowering of the photic zone which increased the abundance of purple sulphur bacteria. That process is explained in chapter 6.2. In addition, our proxies indicate a higher lake production. This might be linked to the increased presence of *Alnus*, which may act as a nutrient source (Devotta et al., 2021; Goldman, 1961). Also, on land, we observe more frequent cultivation of *Castanea* and *Juglans* as well as elevated *sporormiella* spores, an indicator for animal presence. Thus, silvopasture might have been applied.

Geomorphological data suggests a lake level increase to 450 m a.s.l. by 100 CE, which flooded the previously drained swamp (Giraudi, 2004). The lake level increase led to a higher catchment input as the catchment was again larger and encompassed the entire Caldera di Latera. Also, the higher lake level lowered the relative depth promoting lake mixing and elevated the photic zone limiting purple sulphur bacteria and is potentially responsible for the lower lake production (see chapter 6.2). However, from 150 to 250 CE and from 300 to 450 CE, we have two phases of reduced catchment input, higher lake production, and elevated purple sulfur bacteria. A planned high-resolution pollen record of this time period may clarify the role of *Alnus* as a nutrient source. This is currently not possible with the overview pollen record of Sadori (2018). That overview record shows that forests remained closed until the end of the unit at 685 CE while human indicator pollen showed an upward trend. Interestingly, Luzi & Scipioni (1994) suggested that Lago di Mezzano could be the Lacus Statoniensis, on whose shores the Vandals burned Statonia in the 5th century CE, but in absence of archaeological evidence (Sadori, 2018). This phase of decreasing population (~400-

600 CE) was wetter and colder and is referred to as the migration period or the Late Antique Little Ice Age (Büntgen et al., 2011; 2016)

Unit 8 (294.5-0 cm, 685-2019 CE)
At 700 CE the forest opened. Elevated human indicator pollen and *sporormiella* show increased agriculture and animal husbandry. Also, at 750 CE *Castanea* peaked. With the added human activity erosion increased, as indicated by higher clastic input and sedimentation rates. Also, with the forest opening, anoxic indictors dropped, possibly because of amplified wind shear on the lake which eased lake mixing. In 900 CE, the fortified village of Mezzano was founded, and lasted until 1348 CE (Luzi, 1990; Sadori, 2018). Interestingly, human impact is reduced between 950 and 1150 CE. This is a phase of a slightly higher lake level and increased humidity (Giraudi, 2004; Regattieri et al., 2014). Furthermore, the forest closed again, and lake stratification was likely present. That environment supported a higher primary production and the stabilised slopes reduced clastic input and made the catchment more resilient against erosion and floods. Considering the uncertainty of Sadori's (2018) chronology, this confirms our hypothesis of a reduced human impact around that time.

At 1150 CE we observe a massive forest reduction to lower levels than today. That change was induced by increased human activity which led to an expansion of fruit trees, cereals, cannabis (for rope and cloth production), and pastureland (Sadori, 2018). Also, the open landscape increased wind shear on the lake surface which possibly favoured oxic conditions and holomixis. Furthermore, we see elevated erosion and sedimentation rates. At that time, the historically documented Tiber river floods occurred (Camuffo & Enzi, 1996) which probably affected the region of Lago di Mezzano as well. Hence, this highlights the susceptibility of a human transformed landscape to erosion and flooding under increased rainfall. In 1348 CE, after the abandonment of the village Mezzano, arboreal pollen increased but forests remained open and the landscape was used agriculturally. Also, the lake level of Lago di Mezzano increased by 3 m to 454 m a.s.l. (Giraudi, 2004). Thus, the greater lake surface might be the reason for the higher primary production observed during the Little Ice Age. In the 18th century, and during the beginning of the 20th century, reclamation works led again to a lowering of the lake to today's level of 452 m a.s.l. This lowering made the lake considerably smaller, and drained the swamps, making the land available for agriculture (Giraudi, 2004; Ramrath et al., 2000). In the following years, today's mesotrophic to oligotrophic lake formed.

6.2 Lake response to natural variability and human pressure

6.2.1 Effects on lake productivity

We further assessed the forcing factors of the lake ecosystem. Primary productivity is mainly guided by availability of macronutrients (N, P, K), light, and temperature (Wetzel, 2001). This is in line with our observations. Our statistical analyses (RDA on natural and human state, chapter 5.5) suggest a positive effect of warmer temperature on primary productivity (TChl and Si/Ti) over the entire record. A detailed look at the summer temperature – productivity relationship reveals a nonlinear relationship with a strong increase in productivity above 18°C (see Fig. 17). First, that can be related to a direct effect as warmer summer temperatures support a longer productive period as well as more rapid photosynthesis (Wetzel, 2001). Second, our data suggests another indirect effect over chemical weathering. We observed elevated productivity in warm phases with high chemical weathering (high Rb/K and low OI; PCAs and RDAs, chapter 5.4 and 5.5). This is because warmer temperatures do enhance chemical weathering (Li et al., 2016) which in turn provides nutrients (Hartmann et al., 2014) and enhances productivity.

As these nutrients come from the lake catchment, a small lake share on the catchment (smaller lake) increases the availability of nutrients and eutrophication (Heikonen, 2021; Lisi & Hein, 2019; Read et al., 2015). That might be an explanation for why we find high productivity connected with lower lake levels

(which increase the share of the catchment). However, that relationship between lake size and catchment size changed after Roman land reclamation works (Giraudi, 2004). In contrast, higher lake levels were associated with the abundance of *Alnus* which expanded into formed wetlands. That N-fixing plant may provide bioavailable nitrogen to the lake water (Devotta et al., 2021; Goldman, 1961).

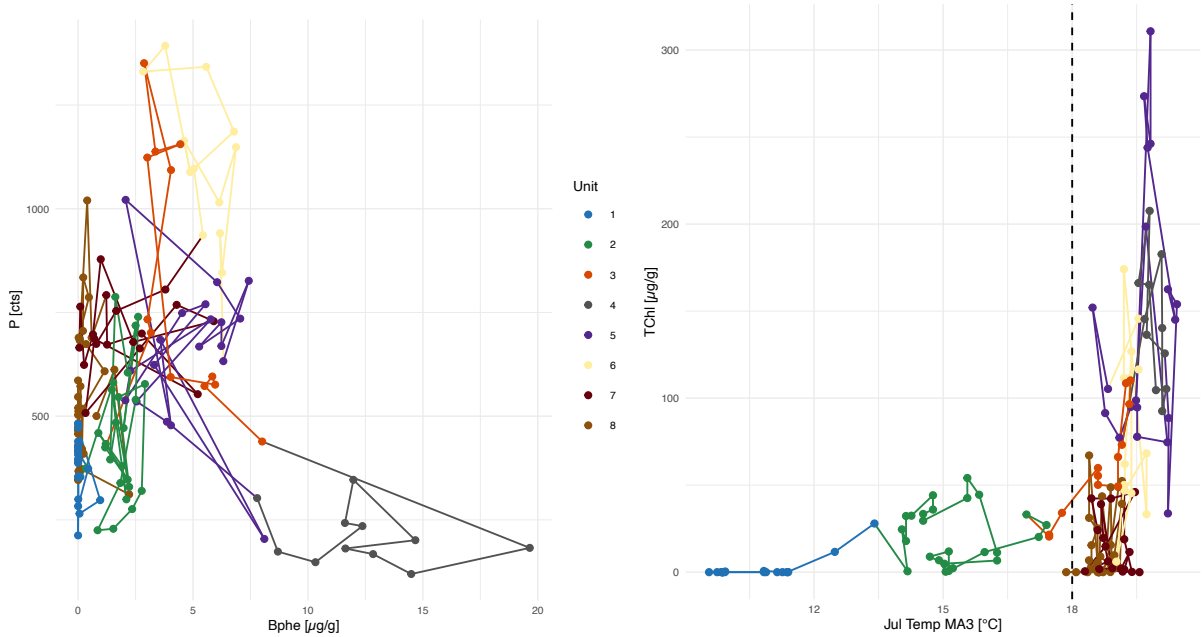

Fig. 17: Processes influencing nutrient availability and temperature. The left panel shows sedimentary P (y-axis) in contrast to anoxic conditions (x-axis, Bphe). With increasing Bphe, P gets recycled, and we only get little P trapped in the sediment. The right panel shows the relationship between production (y-axis = TChl) and temperature (x-axis = July temperature). At low temperatures we only have low TChl concentrations, whereas we get higher TChl concentrations at high temperatures.

Furthermore, we observed an overall positive correlation between the nutrient phosphorus and the productivity indicator TChl in our sediment. However, in phases of strong anoxia (early- and mid-Holocene, 11.0-3.5 ka BP) that relationship no longer holds. This can be explained by a change of the phosphorous source from allochthonous to autochthonous. An internal source of phosphorous comes from previously trapped sedimentary P which is released into the water column under anoxia (Tu et al., 2019). Indeed, we observe high concentrations of total carotenoids at that time span (see annex D2). For Italy they have been related to high phosphorous concentrations in the water column (Guilizzoni et al., 2011). Tu et al. (2019) had concerns that eutrophication restoration (a return to nutrient poor levels) might be inhibited by such P-cycling in deep monomictic lakes. Our data shows that human disturbance (landscape opening) can increase lake mixing (see chapter 6.2.2) and potentially reduce internal P loading. Hence, depending on the redox state P stays available for a prolonged time or is trapped into the sediment which has an influence on productivity. Thus, redox conditions and the mixing regime are another important indirect factor on lake productivity. This is in line with a very high correlation of Bphe and TChl. However, there are complex feedback loops, and higher productivity might also support anoxia or, in contrary, less purple sulfur bacteria (see chapter 6.2.2).

Based on these processes, we explain the increase in productivity in the Bølling / Allerød and early Holocene (until 9.0 ka BP) with the higher temperatures. Later, during the Holocene under stable summer temperatures the extent of anoxic conditions guides nutrient availability and variations in productivity. Hence, anoxia is positively correlated with high productivity whereas lake mixing is in phase with lower productivity. Drivers of anoxia will be discussed in chapter 6.2.2.

However, increased mixing and oxic conditions might also degrade organic matter and reduce pigment concentrations and hence, bias our result. That does not seem to be a big problem at Lago di Mezzano as Wilkes et al. (1999), who studied organic chemistry, highlighted the good preservation of organic matter in the sediment. Also, high sedimentation rates decrease concentrations due to the matrix effect. Therefore, we used pigment flux rates instead of concentrations for the statistical analysis.

According to Ramrath (1997), productivity in Lago di Mezzano is now mainly sustained by silica-limited diatoms. They use up all available silica, and likely nitrogen and phosphorous as well by early May (Ramrath, 1997). However, if silica is limiting, a succession of first green algae and later cyanobacteria is typically observed (Wetzel, 2001). As our HSI derived TChl estimates include diatoms, green algae and cyanobacteria, we cannot use that proxy to assess if there was such a succession in the productive phase of Lago di Mezzano. However, we also measured the total carotenoids (TC) using the spectrophotometer. These pigments are more abundant in cyanobacteria and are better preserved under anoxic conditions than TChl (Swain, 1985). Therefore, we used the TC/TChl ratio as an indicator for cyanobacteria or anoxia. That ratio was highest at times of elevated diatoms (see annex D2). Hence, we assume that that proxy does not reflect cyanobacteria but anoxic conditions at Lago di Mezzano. Also, Wilkes et al. (1999) only found evidence for cyanobacteria in the shallowest sample.

6.2.2 Effects on lake stratification

Important factors guiding the extent of anoxia are nutrient availability and related primary production, temperature, wind, and lake level changes (Boehrer et al., 2017; Boehrer & Schultze, 2008). We observed a high correlation of primary productivity indicators with anoxia indicators. This can be explained by a complex positive feedback mechanism linked to organic matter cycling (Boehrer et al., 2017; Wetzel, 2001). As mentioned in the last chapter, primary producers are assimilating nutrients, as well as dissolved inorganic carbon (DIC) in the epilimnion, at light availability thereby removing these nutrients from the water column. This lowers the density of the water, makes it fresher and elevates the pH. Dead biomass sinks to the bottom waters where its respiration consumes hypolimnic oxygen. Next, elevated CO_2 levels lower pH while the release of nutrients leads to an increase in bottom water density. Furthermore, in anoxic conditions, substances tend to go to their reduced form further enhancing density (Boehrer et al., 2017; Wetzel, 2001). Thus, these denser bottom waters establish chemical stratification with an anoxic hypolimnion. Therefore, lake production can increase oxygen depletion and stratification.

Temperature is another important driver of anoxic conditions and explains the close link of warmer temperatures to anoxic conditions in the natural period. This can be explained not only by increased productivity (see chapter 6.1). Especially in the mid-Holocene thermal maximum, where we observed strong anoxia, we expect an increased contribution of thermal stratification which makes lake mixing more difficult. That is when a warm and less dense epilimnion and a cooler and denser hypolimnion gets separated by the thermocline (Lerman, 1978). Furthermore, warmer water decreases the solubility of solutes and gases which precipitate from the epilimnion to the bottom or outgas into the atmosphere. Outgassing reduces the O_2 concentration whereas particulate matter may redissolve in the hypolimnion, adding to its density and creating a chemical stratification (Boehrer et al., 2017; Wetzel, 2001).

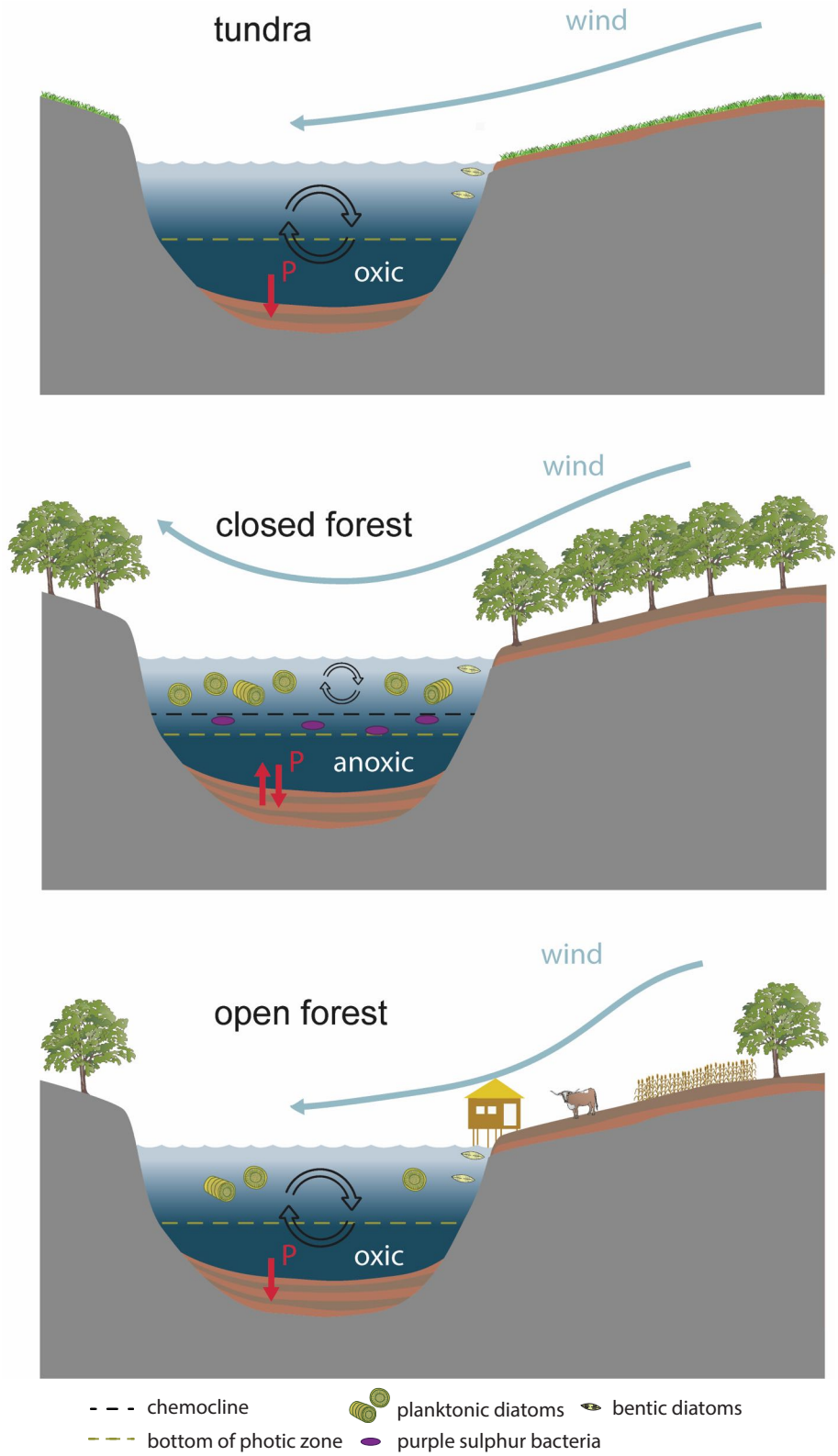

Fig. 18: Effect of forest cover on lake stratification, P trapping, and productivity. The top panel shows lake conditions during Late Glacial tundra, the middle panel depicts lake conditions during Holocene closed forests, and the bottom panel displays lake settings under Holocene open forests induced by human activity (since the early Neolithic).

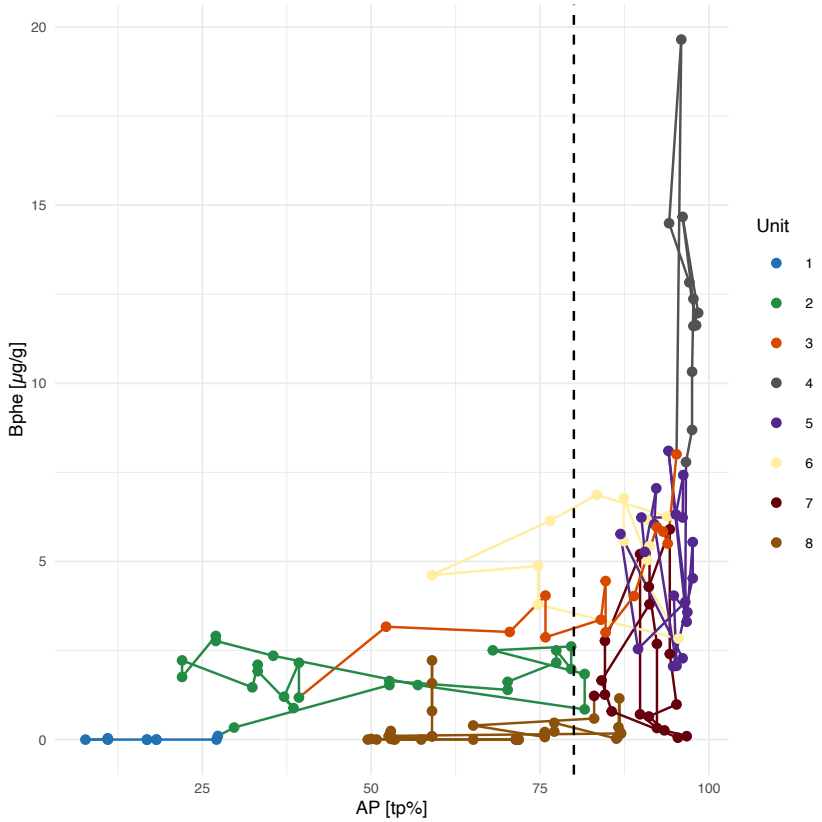

Fig. 19: Open forest prevents anoxia. High Bphe values are only reached in closed forests (AP > 80%).

To counter anoxic conditions in the hypolimnion, mixing is required to exchange oxygen, DIC and nutrients. Mixing in warm monomictic lakes (Hutchinson & Löffler, 1956) occurs in autumn / winter when lower temperatures lead to a uniform density throughout the water column and hence, to a breakdown of the thermocline (Wetzel, 2001). Additionally, wind or undercurrents can create internal waves that may propagate across the lake leading to diapycnical mixing (Imboden & Wüest, 1995). Wind induced mixing explains our observed relationship between arboreal pollen and anoxia, especially during the human influenced period where summer temperature was more stable (see chapter 6.2.1 or Fig. 11, Fig. 12, and Fig. 13).

Therefore, we investigated that relationship more closely. We found a nonlinear relationship between forest cover and Bphe concentrations. Fig. 19 shows that open landscapes (AP < 80%) have Bphe values below the detection limit whereas closed forest sustains high Bphe values. That observation can be explained by increased wind shielding of closed forest stands which prevents lake mixing whereas an open landscape allows for higher wind shear. Furthermore, we observed increasing erosion in open landscapes. Vegetation stabilises soils and slows flooding trough a multitude of factors. Forests intercept precipitation, increase evaporation (Schüler, 2006), increase soil moisture deficits (Lange et al., 2013), thereby increasing water capacity (Hegg et al., 2004), and improve the porosity and water up-take capacity of soils (Weingartner et al., 2003). Flood related erosion might support lake mixing by forming undercurrents creating internal waves (Boehrer et al., 2017). A look at our Neolithic case-study section confirms the mentioned influence of forest cover. Thus, these findings support our hypothesis that anoxia is related to closed forest stands because of reduced mixing. Similar relationships between forest cover and lake mixing have been observed for the Holocene in several small and deep temperate (Dräger et al., 2016; Lotter, 2001; Makri et al., 2020; Sanchini et al., 2020; Wienhues, 2019; Zander et al., 2021) and Mediterranean lakes (Gassner et al., 2020).

Moreover, we observed a high correlation of open landscape and human activity since the Neolithic (see chapter 5.5 or Fig. 11, Fig. 12, and Fig. 13). Precisely, a first event of forest opening under combined human and climatic influence can be dated to 7.2 ka BP. Thus, humans shaped the lake ecosystem at Lago di Mezzano since the Neolithic by inducing forest changes. This timing is in line with archaeological evidence that suggests the advent of the Neolithic in central Italy at similar times (Isern et al., 2012; Radi & Petrinelli Pannocchia, 2018).

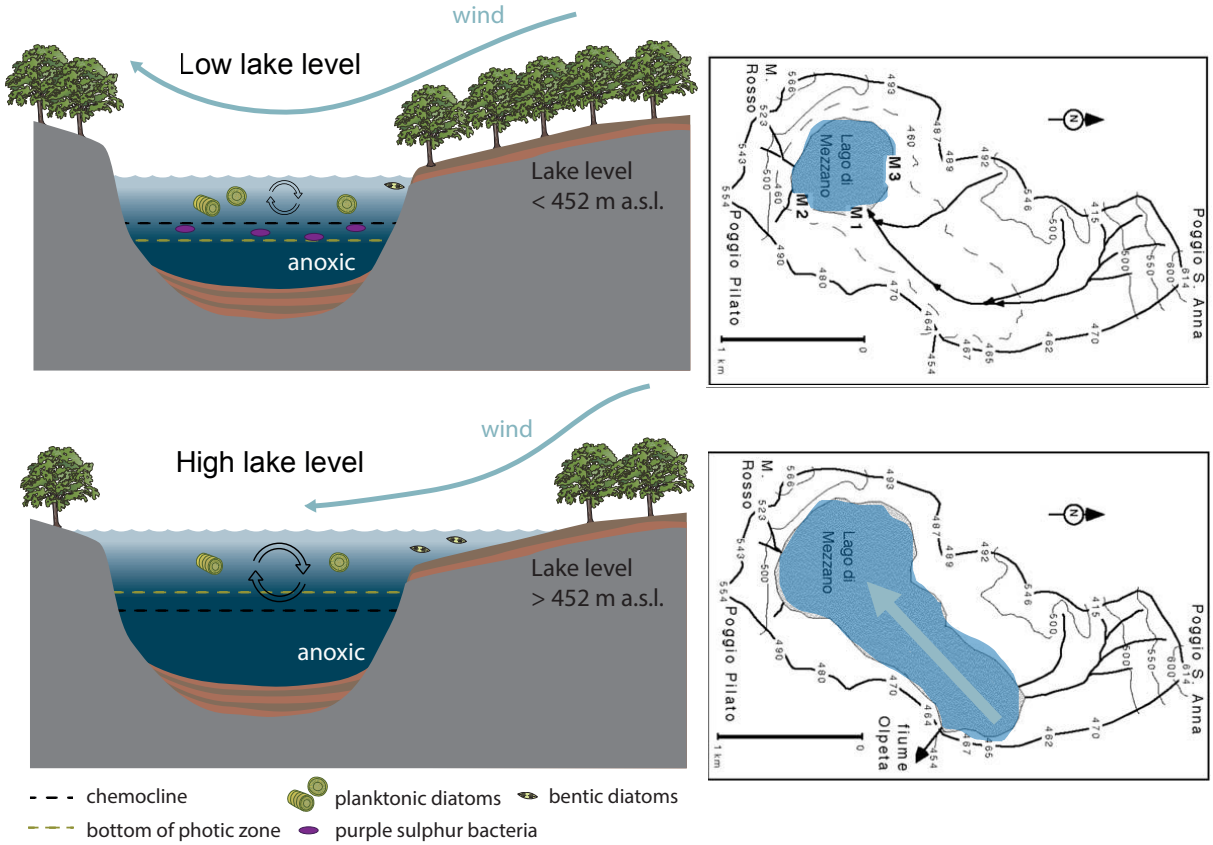

Fig. 20: Effect of lake level changes on lake stratification and anoxia. Left panel: process diagrams. Right panel: Map of the catchment with lake extent. M1-M3 denote the location of Bronze Age pile dwellings. Maps are modified from Giraudi (2004).

Additionally, lake level is an important factor guiding anoxia. We found a correlation of low lake levels and anoxic conditions. We interpreted this as evidence that a higher lake level promotes lake mixing thanks to the special geomorphology of Lago di Mezzano. At low lake levels, the lake has a high relative depth (deep and small surface area) which enhances the physical stability of the water column (Camacho et al., 2017). At higher lake levels, especially above 452 m a.s.l., the surface area increases exponentially while the lake is only slightly deeper. Thus, wind can increasingly act on the lake surface (light blue arrow on map and process diagram in Fig. 19), promoting mixing and eroding the chemocline (see Fig. 20). This process is tracked in our Bphe record as well, as purple sulphur bacteria (PSB) require light and anoxic conditions (Yurkov & Beatty, 1998). With a higher lake level, the lake becomes deeper, and the photic zone rises while the anoxic zone remains in the maar trough as wind mixing increases due to the larger lake surface. As a result, the anoxic hypolimnion and the photic zone no longer overlap (see process diagram, Fig. 19). Thus, PSB lose their habitat because of light limitation. In contrast, with a lower lake level the lake becomes shallower and the photic zone also reaches deeper areas (see process diagram, Fig. 19). The greater the overlap of the anoxic and the photic zone, the more space the PSB have to thrive. However, if the lake becomes too shallow, mixing reaches the bottom and anoxia ceases. To further analyse that effect, it would be interesting to model the lake depth over time based on the core depth and the lake level at a given time. With this

approach, the effect of lake filling would be omitted. Thus, a more direct link to the size of the photic-anoxic zone would be possible and potentially better explain a lake depth effect on PSB. Furthermore, a reconstruction of the potential surface area together with the lake depth might reveal further in-lake processes affected by this lake level effect. This could be especially relevant in attempts to reconstruct past lake levels based on biogeochemical properties.

If throughout several years no full mixing is possible, a lake is considered meromictic and forms a lower, denser monimolimnion with permanent anoxia and an upper, lighter, circulating mixolimnion. The chemically distinct layers with a strong density gradient are separated by the chemocline (Boehrer et al., 2017; Hutchinson, 1957). Such a phase of extensive and prolonged anoxia was potentially present in the mid-Holocene, when there were warmer summer temperatures and high Bphe concentrations throughout each year. Thus, an extended anoxic zone during the mid-Holocene thermal maximum supports model results that project most warm-monomictic lakes to become meromictic (Woolway & Merchant, 2019).

To summarise, until 9.4 ka BP, we explain shifts in anoxia by changing temperatures. Especially, the early Holocene warming as well as its resulting increase in primary production and feedbacks explained above led to the formation of strong anoxic conditions. Thereafter, anoxic conditions (lake stratification) are mainly driven by changes in forest cover and lake level. Since the Neolithic, forest openings can be related to human activity while lake level regulation only started with the Romans. Thus, Lago di Mezzano has been shaped by human activity for over 7000 years.

We found that forest density is promoting lake stratification in warm-monomictic Lago di Mezzano. Also, we know that closed forests are promoting stratification in different lake mixing regimes (Dräger et al., 2016; Gassner et al., 2020; Lotter, 2001; Makri et al., 2020; Sanchini et al., 2020; Wienhues, 2019; Zander et al., 2021). Thus, our finding adds to that research and highlights the importance to include landscape management in lake restoration. Forest cover is increasing in Europe (Forest Europe, 2015; Martín-Forés et al., 2020), especially in remote mountainous areas. This forest regrowth might have unexpected side effects on the mixing behaviour of lakes, and may not only alter biodiversity on land, but also change communities in lakes.

We could prove that summer temperature is an important factor in lake productivity and lake stratification. Thus, we expect an increase in hypoxia and lake productivity with ongoing climate change. However, landscape management and human impact can have an equally large impact on lake conditions.

6.3 Validation of high-resolution scanning data

We validated our high-resolution scanning proxies with previously published conventional biogeochemical data on Lago di Mezzano (Brandt et al., 1999; Ramrath et al., 1999a, 1999b, 2000; Wilkes et al., 1999; see data chapter).

To start, we observed a high agreement of all the catchment minerals (Fe, K, Si) and erosion proxies (Ti, R850/R900) with conventionally measured dry density and minerogenic matter. Thus, that supports our interpretation of these proxies as clastic input. Their terrestrial source is validated by a high correlation with the oxygen index (OI), which indicates a terrestrial source of organic matter (Wilkes et al., 1999). The physical weathering indicators (K/Ti and K/Al) have a similar meaning, and they also highly correlate with the OI. Interestingly, mass accumulation rate (MAR) and sedimentation rate (SR) are both highly correlated with clastic input. Thus, we suggest that higher clastic indicators show an erosive environment and true element composition. That is supported by the fact that smear slide analysis showed similar results as the

conventional biogeochemical analysis (see chapter 5.2), which in turn is highly correlated with our scanning proxies.

We further highlight, that the R850/R900 hyperspectral index shows a high agreement with catchment minerals and erosion proxies. Thus, that index developed for a volcanic catchment on sub-Antarctic Macquire Island in the Southern Ocean worked very well. Therefore, we recommend using the R850/R900 in other volcanic catchments as it can give information about erosion when no XRF-scans are available. Furthermore, HSI provides spatial maps at very high resolution, thus that index may potentially support varve counting.

The indicators of clastic input and physical weathering are in antiphase with chemical weathering, productivity, and anoxia indicators. First, the hydrogen index, indicating an aquatic source of organic matter, correlates well with the elemental ratio Rb/K, a chemical weathering proxy, indicating that chemical weathering is an important control on nutrient loading at Lago di Mezzano. In contrast, they have a high anticorrelation with physical weathering and OI. Thus, we observe a dichotomy of physical weathering with terrestrial organic matter and chemical weathering with aquatic organic matter. Therefore, we selected the independently acquired oxygen index as a proxy for these processes in our full-proxy dataset.

Second, our proxies for productivity (TChl, Si/Ti, Br) show a high correlation with total organic carbon (TOC), organic matter (LOI) and biogenic matter (BiM). Remarkable is the good performance of the Si/Ti elemental ratio as an indicator of diatoms. That elemental ratio has a high correlation with semi-quantitatively estimated benthic and planktonic diatoms as well as with measured biogenic opal. Biogenic opal is reported to represent diatoms at Lago di Mezzano (Ramrath, 1997; Ramrath et al., 2000).

Third, the HSI based anoxia indicator Bphe and the XRF based elemental ratio (Fe/Ti)/Mn show a high correlation over the entire core. That similar behaviour indicates that both proxies effectively track anoxic conditions. In contrast, the elemental ratio (Fe/Mn) is much more influenced by catchment input indicators which is in line with previous findings of a bad performance of this proxy under high erosion (Makri et al., 2021a). That element proxy works because Mn gets dissolved faster under anoxic conditions than Fe (Boyle, 2002). However, Marki et al. (2021a) described that Fe dissolves under strong anoxia as well, which explains a drop of the (Fe/Ti)/Mn ratio under very high Bphe concentrations. Therefore, a combined use of these HSI and XRF proxies allows for a higher certainty about the extent of the anoxic zone.

Finally, there are some minerals that are formed under anoxic conditions in the sediment or in the water column at the deposition or diagenetically. We found that their abundance is linked to the presence of certain substances. For pyrite (FeS_2), an iron sulphide, we found a correlation with total sulphur. In contrast, siderite ($FeCO_3$) forms only at very low Ca and S levels, and since sulphur abundance correlates with organic matter, siderite has been associated with clastic input. Indeed, total inorganic carbon represents exclusively siderite at Lago di Mezzano and no calcium carbonate ($CaCO_3$) is present (Ramrath, 1997). Vivianite, a hydrated iron phosphate, is correlated with P counts.

In summary, the validation confirms that all used proxies work well. As each lake and catchment is different, validation of scanning data by specific biogeochemical data is important to distinguish signal from noise.

6.4 Potential of high-resolution scanning data

Non-destructive HSI and XRF scanning are fast and cost-effective methods to provide continuous data at very high spatial resolution. HSI enabled us to reconstruct in-lake primary productivity and anoxia based on calibrated pigments (TChl and Bphe). First, the calibration has the advantage that we obtain quantitative pigment concentrations and not just a semi-quantitative index. Second, with a calibration we certainly know that a pigment is present, which in turn allows to infer the presence of associated target process. E.g. without a calibration of the $RABD_{845}$ index we do not know at what index value Bphe is present, whereas with a calibration we certainly know the presence of Bphe and hence, that anoxia is extending to the photic zone. However, this does not resolve the challenge that the absence of evidence is not the evidence of absence. Thus, to stay with the same example, if we do not detect any Bphe we do not know if, first, the pigment was present but then vanished. Or, second, if the target process (anoxia) was present without purple sulphur bacteria and hence, not detectable by this proxy. Such challenges can only be handled by using multiple lines of evidence. We used XRF scans to get proxies with similar interpretations as detected in HSI. For example, the elemental ratio (Fe/Ti)/Mn is another indicator of anoxia. Moreover, HSI enabled us to map the mineral vivianite semi-quantitatively. Its occurrence indicates anoxic conditions in the sediment and helps to better understand the mineralogy of the sediment. Furthermore, conventional biogeochemical data added an additional line of evidence. Thus, the comparison of different proxies and an understanding of the sediment increased our certainty that measured features were real.

Next, following a multi-proxy approach enabled us to link in-lake processes to catchment processes and climate variations. For example, we could demonstrate the influence of lake level variations and warmer temperatures on lake stratification on productivity. On sub-decadal scale, we could show that human-induced forest reduction enhanced lake mixing whereas a grow back promoted lake stratification and anoxia. Such insights into early human impacts are only possible in a holistic approach and with a high chronological certainty.

Furthermore, we could detect seasonal variations in our proxy record and verify the presence of annual laminations. As sedimentation rates are very low at Lago di Mezzano we achieved that by applying ultra-high-resolution HSI and μXRF scans (25 and 50 μm) to the Bronze Age case-study section. With an average varve thickness of around 1 mm per year we acquired 20-40 data points per year. That was sufficient to prove the annual character of the varves together with prior knowledge from microscope analyses. However, the varves were very badly preserved compared to what was reported from the 1995 core (work of Ramrath, 1997). Hence, we could not accomplish our goal of a continuous seasonal analysis. The unsatisfying preservation of the varves can have several reasons. First, we used a different coring location and another coring system to extract the sediment. Second, Ramrath (1997) used large-scale thin sections to microscopically analyse varves whereas we used resin blocks. Also, we have not done microscope analyses. Third, the extraction of the U-Channels as well as resin embedding can further degrade varves as we observed the formation of cracks in the process. And finally, varves could have deteriorated during transport as cooling could not be maintained throughout. However, a continuous seasonal scale record has huge potential and enables analysing in-lake and catchment interactions at seasonal scale. Hence, much needed long-term data at observational scale (Friedrich et al., 2014) could be provided by such an approach.

7 Conclusion and outlook

Our HSI and XRF based scanning records together with a high-precision chronology enabled us to reconstruct changes in lake productivity, mixing regime, erosion, and weathering at sub-decadal scale throughout the past 18,000 years. We could link these processes to the lake catchment's environmental history and postglacial climate change. In the Late Glacial, in a dry and cold tundra landscape, we found low productivity and frequent lake mixing. During the Bølling /Allerød warming, mixed oak forest expanded while production increased, and lake stratification was enhanced. After the Younger Dryas cooling, with a fall back to glacial conditions, the warm and dry early-Holocene led to a stable landscape, dominated by a mixed oak / beech forest with high lake production and extensive anoxia. Since the early Neolithic, humans periodically were present in the catchment and responsible for forest clearings. With the onset of the Bronze Age, human impact became more prominent and is confirmed by the presence of pile dwellings. Around 300 BC, the Romans stated lake regulations and changed the lake functioning completely. Finally, an open landscape with low productivity and oxic conditions established in the last centuries.

Before human presence, increased lake productivity and anoxia were mainly forced by elevated temperatures, supporting model projections of future lake mixing regime shifts in response to global warming. As a result, we may expect increased stratification of warm-monomictic lakes with ongoing climate change. High lake level stands of the highly variable Lago di Mezzano were associated to low lake productivity and increased mixing behaviour thanks to the special lake morphology. In the Holocene, likely human-induced forest openings promoted lake mixing and a cease of anoxia because of higher wind shear. These oxic conditions favoured sedimentary nutrient trapping and reduced the lake productivity whereas closed forest stands increased anoxia and nutrient recycling. Thus, a return to a natural forested state might lead to lake stratification. This process was observed now for the first time in a warm-monomictic lake and adds to previous research at other temperate and Mediterranean lakes. As forest are regrowing in Europe that might have unexpected side effects on the mixing behaviour of lakes and communities in these lakes. We, therefore, highlight that landscape management has an important role in how lake ecosystems react in ongoing climate change, and that it should be considered in lake restoration.

Proxy-proxy validation confirmed that inferences from non-destructive core-scanning proxies are valid. We could show that vivianite can be mapped, proved the validity of the R850/R900 spectral ratio as an indicator for erosion in volcanic catchments, and developed a new elemental ratio (Fe/Ti)/Mn for anoxia which is less prone to bias by erosional input. For the Bronze Age, we acquired an ultra-high-resolution (up to 25 μm) HSI and μXRF record and proved the presence of varves. However, varves were very badly preserved and we could not provide a continuous seasonal scale record. Such a record could enable the analysis of in-lake and catchment interactions at seasonal scale and provide much needed long-term data at observational scale.

Based on our record, ongoing palynological investigations on the Neolithic and Iron Age will give further insights about early human impacts on the lake ecosystem. Also, in the Iron Age and more recent time periods high-resolution climatological and historical data are available. Furthermore, work is planned to reveal lake responses to rapid climate changes in the Late Glacial. These results will make it possible to further contextualise the processes found here in different settings. Furthermore, a lake level reconstruction based on diatoms, grain size analysis or X-ray diffraction (analysation of the mineralogy) could provide detailed insights on how lake production and mixing respond to lake level changes. Research on other Mediterranean lakes in Greece is ongoing. Here, similar analyses should show if these lakes have a similar response to natural variability and human pressure. Moreover, analyses on longer time series could reveal how Mediterranean lakes reacted at other deglaciations with no human impact.

8 References

Abell, R., Thieme, M. L., Revenga, C., Bryer, M., Kottelat, M., Bogutskaya, N., Coad, B., Mandrak, N., Balderas, S. C., Bussing, W., Stiassny, M. L. J., Skelton, P., Allen, G. R., Unmack, P., Naseka, A., Ng, R., Sindorf, N., Robertson, J., Armijo, E., … Petry, P. (2008). Freshwater ecoregions of the world: A new map of biogeographic units for freshwater biodiversity conservation. *BioScience*, *58*(5), 403–414. https://doi.org/10.1641/B580507

Albert, P. G., Tomlinson, E. L., Lane, C. S., Wulf, S., Smith, V. C., Coltelli, M., Keller, J., Lo Castro, D., Manning, C. J., Müller, W., & Menzies, M. A. (2013). Late glacial explosive activity on Mount Etna: Implications for proximal-distal tephra correlations and the synchronisation of Mediterranean archives. *Journal of Volcanology and Geothermal Research*, *265*, 9–26. https://doi.org/10.1016/j.jvolgeores.2013.07.010

Appleby, P. G. (2001). Chronostratigraphic techniques in recent sediments. In *Tracking environmental change using lake sediments* (pp. 171–203). Springer.

Bennion, H., Battarbee, R. W., Sayer, C. D., Simpson, G. L., & Davidson, T. A. (2011). Defining reference conditions and restoration targets for lake ecosystems using palaeolimnology: A synthesis. *Journal of Paleolimnology*, *45*(4), 533–544. https://doi.org/10.1007/s10933-010-9419-3

Binford, M. W. (1990). Calculation and uncertainty analysis of 210Pb dates for PIRLA project lake sediment cores. *Journal of Paleolimnology*, *3*(3), 253–267. https://doi.org/10.1007/BF00219461

Blaauw, M., & Christen, J. A. (2011). Flexible paleoclimate age-depth models using an autoregressive gamma process. *Bayesian Analysis*, *6*(3), 457–474. https://doi.org/10.1214/11-BA618

Boehrer, B., & Schultze, M. (2008). Stratification of lakes. *Reviews of Geophysics*, *46*(2), 1–27. https://doi.org/10.1029/2006RG000210

Boehrer, B., von Rohden, C., & Schultze, M. (2017). Physical features of meromictic lakes: stratification and circulation. In *Ecology of meromictic lakes* (pp. 15–34). Springer.

Boyle, J. F. (2002). Inorganic geochemical methods in palaeolimnology. In *Tracking environmental change using lake sediments* (pp. 83–141). Springer.

Brai, A., Piro, M., & Trigila, R. (1979). Sudio geopetrografico del Complesso Vulcanico di Latera (Vulcani Vulsini). *Nota III: I Termini Lavici Dell'attività Intracalderica Finale: Periodico Di Mineralogia*, *48*, 205–254.

Brandt, U., Nowaczyk, N. R., Ramrath, A., Brauer, A., Mingram, J., Wulf, S., & Negendank, J. F. W. (1999). Palaeomagnetism of Holocene and late pleistocene sediments from Lago di Mezzano and Lago Grande di Monticchio (Italy): Initial results. *Quaternary Science Reviews*, *18*(7), 961–976. https://doi.org/10.1016/S0277-3791(99)00008-6

Büntgen, U., Myglan, V. S., Ljungqvist, F. C., McCormick, M., Di Cosmo, N., Sigl, M., Jungclaus, J., Wagner, S., Krusic, P. J., Esper, J., Kaplan, J. O., De Vaan, M. A. C., Luterbacher, J., Wacker, L., Tegel, W., & Kirdyanov, A. V. (2016). Cooling and societal change during the Late Antique Little Ice Age from 536 to around 660 AD. *Nature Geoscience*, *9*(3), 231–236. https://doi.org/10.1038/ngeo2652

Büntgen, U., Tegel, W., Nicolussi, K., McCormick, M., Frank, D., Trouet, V., Kaplan, J. O., Herzig, F., Heussner, K.-U., Wanner, H., Luterbacher, J., & Esper, J. (2011). 2500 Years of European Climate Variability and Human Susceptibility. *Science*, *331*(6017), 578–582. https://doi.org/10.1126/SCIENCE.1197175

Butz, C., Grosjean, M., Fischer, D., Wunderle, S., Tylmann, W., & Rein, B. (2015). Hyperspectral imaging spectroscopy: a promising method for the biogeochemical analysis of lake sediments. *Journal of Applied Remote Sensing*, *9*(1), 096031. https://doi.org/10.1117/1.jrs.9.096031

Butz, C., Grosjean, M., Goslar, T., & Tylmann, W. (2017). Hyperspectral imaging of sedimentary bacterial pigments: a 1700-year history of meromixis from varved Lake Jaczno, northeast Poland. *Journal of Paleolimnology*, *58*(1), 57–72. https://doi.org/10.1007/s10933-017-9955-1

Butz, C., Grosjean, M., Poraj-Górska, A., Enters, D., & Tylmann, W. (2016). Sedimentary Bacteriopheophytin a as an indicator of meromixis in varved lake sediments of Lake Jaczno, north-east Poland, CE 1891–2010. *Global and Planetary Change*, *144*, 109–118. https://doi.org/10.1016/j.gloplacha.2016.07.012

Camacho, A., Miracle, M. R., Romero-Viana, L., Picazo, A., & Vicente, E. (2017). Lake La Cruz, an Iron-Rich Karstic Meromictic Lake in Central Spain. *Ecological Studies*, *228*, 187–233. https://doi.org/10.1007/978-3-319-49143-1_8

Camuffo, D., & Enzi, S. (1996). The analysis of two bi-millennial series: Tiber and Po river floods. In P.

D. Jones, R. S. Bradley, & J. Jouzel (Eds.), *Climatic Variations and Forcing Mechanisms of the Last 2000 Years* (pp. 433–450). Springer Berlin Heidelberg.
Centore, P., Davis, G., & Davis, M. G. (2020). *Package ' munsellinterpol .'*
Conti, A. M., Mancini, B., Persiani, C., & Petitti, P. (1993). Ricerche nel territorio del Lago di Mezzano. *Vulcano a Mezzano-Insediamento e Produzioni Artigianali Nella Media Valle Del Fiora Durante l'et" a Del Bronzo. Comune Di Valentano-Museo Civico, Collana Di Studi, Testi e Cataloghi, Valentano*, 45–61.
Corella, J. P., Brauer, A., Mangili, C., Rull, V., Vegas-Vilarrúbia, T., Morellón, M., & Valero-Garcés, B. L. (2012). The 1.5-ka varved record of Lake Montcortès (southern Pyrenees, NE Spain). *Quaternary Research (United States)*, *78*(2), 323–332. https://doi.org/10.1016/j.yqres.2012.06.002
Davies, S. J., Lamb, H. F., & Roberts, S. J. (2015). Micro-XRF core scanning in palaeolimnology: recent developments. In *Micro-XRF studies of sediment cores* (pp. 189–226). Springer.
Dearing, J. A. (2013). Why Future Earth needs lake sediment studies. *Journal of Paleolimnology*, *49*(3), 537–545. https://doi.org/10.1007/s10933-013-9690-1
Del Carlo, P., Branca, S., & D'Oriano, C. (2017). New findings of Late Glacial Etna pumice fall deposits in NE Sicily and implications for distal tephra correlations in the Mediterranean area. *Bulletin of Volcanology*, *79*(7). https://doi.org/10.1007/s00445-017-1135-7
Del Carlo, P., Smedile, A., Petrelli, M., & Di Roberto, A. (2020). Evidence for an unknown explosive eruption of Mt. Etna volcano (Italy) during the Late Glacial. *Journal of Volcanology and Geothermal Research*, *402*, 106992. https://doi.org/10.1016/j.jvolgeores.2020.106992
Devotta, D. A., Fraterrigo, J. M., Walsh, P. B., Lowe, S., Sewell, D. K., Schindler, D. E., & Hu, F. S. (2021). Watershed Alnus cover alters N:P stoichiometry and intensifies P limitation in subarctic streams. *Biogeochemistry*, *153*(2), 155–176. https://doi.org/10.1007/s10533-021-00776-w
Di Gennaro, F. (1986). *Forme di insediamento tra Tevere e Fiora dal bronzo finale al principio dell'età del ferro* (Vol. 14). Olschki.
Dräger, N., Theuerkauf, M., Szeroczyńska, K., Wulf, S., Tjallingii, R., Plessen, B., Kienel, U., & Brauer, A. (2016). Varve microfacies and varve preservation record of climate change and human impact for the last 6000 years at Lake Tiefer See (NE Germany): *The Holocene*, *27*(3), 450–464. https://doi.org/10.1177/0959683616660173
Drysdale, R., Zanchetta, G., Hellstrom, J., Maas, R., Fallick, A., Pickett, M., Cartwright, I., & Piccini, L. (2006). Late Holocene drought responsible for the collapse of Old World civilizations is recorded in an Italian cave flowstone. *Geology*, *34*(2), 101–104. https://doi.org/10.1130/G22103.1
Dunnington, D. (2021). *tidypaleo: Tidy Tools for Paleoenvironmental Archives*.
Fan, Y., & van den Dool, H. (2008). A global monthly land surface air temperature analysis for 1948-present. *Journal of Geophysical Research Atmospheres*, *113*(1), 1–18. https://doi.org/10.1029/2007JD008470
Fiedor, J., Fiedor, L., Kammhuber, N., Scherz, A., & Scheer, H. (2002). Photodynamics of the Bacteriochlorophyll–Carotenoid System. 2. Influence of Central Metal, Solvent and β-Carotene on Photobleaching of Bacteriochlorophyll Derivatives. *Photochemistry and Photobiology*. https://doi.org/10.1562/0031-8655(2002)076<0145:potbcs>2.0.co;2
Finné, M., Woodbridge, J., Labuhn, I., & Roberts, C. N. (2019). Holocene hydro-climatic variability in the Mediterranean: A synthetic multi-proxy reconstruction. *Holocene*, *29*(5), 847–863. https://doi.org/10.1177/0959683619826634
Forest Europe. (2015). *State of Europe's forests 2015*. Ministerial Conference on the Protection of Forests in Europe.
Francke, A., Lacey, J. H., Marchegiano, M., Wagner, B., Ariztegui, D., Zanchetta, G., Kusch, S., Ufer, K., Baneschi, I., & Knödgen, K. (2021). Last Glacial central Mediterranean hydrology inferred from Lake Trasimeno's (Italy) calcium carbonate geochemistry. *Boreas*. https://doi.org/10.1111/bor.12552
Franco, M. C. (1982). *L'insediamento preistorico del Lago di Mezzano: risultati della campagna di ricognizione preliminare settembre 1973*. Edigraf.
Friedrich, J., Janssen, F., Aleynik, D., Bange, H. W., Boltacheva, N., Çagatay, M. N., Dale, A. W., Etiope, G., Erdem, Z., Geraga, M., Gilli, A., Gomoiu, M. T., Hall, P. O. J., Hansson, D., He, Y., Holtappels, M., Kirf, M. K., Kononets, M., Konovalov, S., … Wenzhöfer, F. (2014). Investigating hypoxia in aquatic environments: Diverse approaches to addressing a complex phenomenon. *Biogeosciences*, *11*(4), 1215–1259. https://doi.org/10.5194/bg-11-1215-2014
Gassner, S., Gobet, E., Schwörer, C., van Leeuwen, J., Vogel, H., Giagkoulis, T., Makri, S., Grosjean, M.,

Panajiotidis, S., Hafner, A., & Tinner, W. (2020). 20,000 years of interactions between climate, vegetation and land use in Northern Greece. *Vegetation History and Archaeobotany*, *29*(1), 75–90. https://doi.org/10.1007/s00334-019-00734-5

Giorgino, T. (2009). Computing and visualizing dynamic time warping alignments in R: The dtw package. *Journal of Statistical Software*, *31*(7), 1–24. https://doi.org/10.18637/jss.v031.i07

Giraudi, C. (2004). Le oscillazioni di livello del lago di mezzano (valentano -vt): Variazioni climatiche e interventi antropici. *Alpine and Mediterranean Quaternary*, *17*(1–2), 221–230.

Goldman, C. R. (1961). The Contribution of Alder Trees (Alnus Tenuifolia) to the Primary Productivity of Castle Lake, California. *Ecology*, *42*(2), 282–288. https://doi.org/10.2307/1932080

Guilizzoni, P., Marchetto, A., Lami, A., Gerli, S., & Musazzi, S. (2011). Use of sedimentary pigments to infer past phosphorus concentration in lakes. *Journal of Paleolimnology*, *45*(4), 433–445. https://doi.org/10.1007/s10933-010-9421-9

Gulati, R. D., Zadereev, E. S., & Degermendzhi, A. G. (2017). *Ecology of meromictic lakes* (Vol. 228). Springer.

Guyard, H., Chapron, E., St-Onge, G., Anselmetti, F. S., Arnaud, F., Magand, O., Francus, P., & Mélières, M. A. (2007). High-altitude varve records of abrupt environmental changes and mining activity over the last 4000 years in the Western French Alps (Lake Bramant, Grandes Rousses Massif). *Quaternary Science Reviews*, *26*(19–21), 2644–2660. https://doi.org/10.1016/j.quascirev.2007.07.007

Hartmann, J., Moosdorf, N., Lauerwald, R., Hinderer, M., & West, A. J. (2014). Global chemical weathering and associated p-release - the role of lithology, temperature and soil properties. *Chemical Geology*, *363*, 145–163. https://doi.org/10.1016/j.chemgeo.2013.10.025

Hegg, C., Badoux, A., Lüscher, P., & Witzig, J. (2004). Zur Schutzwirkung des Waldes gegen Hochwasser. *Schutzwald Und Naturgefahren. Forum Für Wissen 2004*, 15–20.

Heikonen, S. (2021). *The relationship between lake eutrophication and characteristics of the lake and its catchment*.

Hutchinson, G. E. (1957). *A Treatise on Limnology, Geography, Physics and Chemistry. 33*, 1–322. https://doi.org/10.1017/S0016756800062634

Hutchinson, G. E., & Löffler, H. (1956). The thermal classification of lakes. *Proceedings of the National Academy of Sciences of the United States of America*, *42*(2), 84. https://doi.org/10.1073/PNAS.42.2.84

Imboden, D. M., & Wüest, A. (1995). Mixing Mechanisms in Lakes. *Physics and Chemistry of Lakes*, 83–138. https://doi.org/10.1007/978-3-642-85132-2_4

IPCC. (2014). *Climate change 2014: synthesis report. Contribution of Working Groups I, II and III to the fifth assessment report of the Intergovernmental Panel on Climate Change (IPCC)* (R. K. Pachauri, M. R. Allen, V. R. Barros, J. Broome, W. Cramer, R. Christ, J. A. Church, L. Clarke, Q. Dahe, P. Dasgupta, & others (eds.)). Ipcc.

Isern, N., Fort, J., & Vander Linden, M. (2012). Space Competition and Time Delays in Human Range Expansions. Application to the Neolithic Transition. *PLoS ONE*, *7*(12), 1–9. https://doi.org/10.1371/journal.pone.0051106

Isola, I., Zanchetta, G., Drysdale, R. N., Regattieri, E., Bini, M., Bajo, P., Hellstrom, J. C., Baneschi, I., Lionello, P., Woodhead, J., & Greig, A. (2019). The 4.2 ka event in the central Mediterranean: New data from a Corchia speleothem (Apuan Alps, central Italy). *Climate of the Past*, *15*(1), 135–151. https://doi.org/10.5194/cp-15-135-2019

Jarvis, S., Croudace, I. W., & Rothwell, R. G. (2015). Parameter optimisation for the ITRAX core scanner. In *Micro-XRF Studies of Sediment Cores* (pp. 535–562). Springer.

Jeffrey, S. W., & Humphrey, G. F. (1975). New spectrophotometric equations for determining chlorophylls a, b, c1 and c2 in higher plants, algae and natural phytoplankton. *Biochemie Und Physiologie Der Pflanzen*. https://doi.org/10.1016/s0015-3796(17)30778-3

Jenny, J. P., Francus, P., Normandeau, A., Lapointe, F., Perga, M. E., Ojala, A., Schimmelmann, A., & Zolitschka, B. (2016). Global spread of hypoxia in freshwater ecosystems during the last three centuries is caused by rising local human pressure. *Global Change Biology*, *22*(4), 1481–1489. https://doi.org/10.1111/gcb.13193

Juggins, S. (2020). *Paquete "Rioja" V0.9-26*.

Kagalou, I., & Leonardos, I. (2009). Typology, classification and management issues of Greek lakes: Implication of the Water Framework Directive (2000/60/EC). *Environmental Monitoring and Assessment*, *150*(1–4), 469–484. https://doi.org/10.1007/s10661-008-0245-2

Kassambara, A., & Mundt, F. (2020). Package 'factoextra': Extract and visualize the results of multivariate data analyses. *CRAN- R Package*, 84. https://cran.r-project.org/package=factoextra

Kelly, K. L., & Judd, D. B. (1976). *Color: universal language and dictionary of names* (Vol. 440). Department of Commerce, National Bureau of Standards, Center for Building Technology.
Lange, B., Germann, P. F., & Lüscher, P. (2013). Greater abundance of Fagus sylvatica in coniferous flood protection forests due to climate change: Impact of modified root densities on infiltration. *European Journal of Forest Research*, *132*(1), 151–163. https://doi.org/10.1007/s10342-012-0664-z
Laskar, J., Robutel, P., Joutel, F., Gastineau, M., Correia, A. C. M., & Levrard, B. (2004). A long-term numerical solution for the insolation quantities of the Earth. *Astronomy and Astrophysics*, *428*(1), 261–285. https://doi.org/10.1051/0004-6361:20041335
Lee, M., Shevliakova, E., Malyshev, S., Milly, P. C. D., & Jaffé, P. R. (2016). Climate variability and extremes, interacting with nitrogen storage, amplify eutrophication risk. *Geophysical Research Letters*, *43*(14), 7520–7528. https://doi.org/10.1002/2016GL069254
Lerman, A. (1978). *Lakes: chemistry, geology, physics*. Springer-Verlag Berlin Heidelberg GmbH. https://doi.org/10.1007/978-1-4757-1152-3
Lerman, A., Imboden, D. M., Gat, J. R., & Chou, L. (1995). *Physics and chemistry of lakes*. Springer-Verlag Berlin.
Li, G., Hartmann, J., Derry, L. A., West, A. J., You, C. F., Long, X., Zhan, T., Li, L., Li, G., Qiu, W., Li, T., Liu, L., Chen, Y., Ji, J., Zhao, L., & Chen, J. (2016). Temperature dependence of basalt weathering. *Earth and Planetary Science Letters*, *443*, 59–69. https://doi.org/10.1016/j.epsl.2016.03.015
Lisi, P. J., & Hein, C. L. (2019). Eutrophication drives divergent water clarity responses to decadal variation in lake level. *Limnology and Oceanography*, *64*, S49–S59. https://doi.org/10.1002/lno.11095
Livingstone, D. M., & Lotter, A. F. (1998). The relationship between air and water temperatures in lakes of the Swiss Plateau: A case study with palaeolimnological implications. *Journal of Paleolimnology*, *19*(2), 181–198. https://doi.org/10.1023/A:1007904817619
Livingstone, D. M., Lotter, A. F., & Walkery, I. R. (1999). The Decrease in Summer Surface Water Temperature with Altitude in Swiss Alpine Lakes: A Comparison with Air Temperature Lapse Rates. *Arctic, Antarctic, and Alpine Research*, *31*(4), 341–352. https://doi.org/10.1080/15230430.1999.12003319
Lotter, A. F. (2001). The palaeolimnology of Soppensee (Central Switzerland), as evidenced by diatom, pollen, and fossil-pigment analyses. *Journal of Paleolimnology*, *25*, 65–79.
Luzi, R. (1990). Eine wahrscheinlich langobardische Siedlung bei Valentano (Prov. Viterbo, Italien). Ein Vorbericht. In F. M. Andraschko & W.-R. Teegen (Eds.), *Gedenkschrift für Jürgen Driehaus* (pp. 277–285).
Luzi, R., & Scipioni, A. (1994). Mezzano, Lago Preistorico. *Geos*, *6*, 111.
Maechler, M., Rousseeuw, P., Struyf, A., Hubert, M., Studer, M., & Hornik, K. (2021). *cluster: Cluster Analysis Basics and Extensions. R package version 2.1.2 — For new features, see the "Changelog" file (in the package source)*. https://cran.r-project.org/package=cluster
Magny, M., Combourieu-Nebout, N., De Beaulieu, J. L., Bout-Roumazeilles, V., Colombaroli, D., Desprat, S., Francke, A., Joannin, S., Ortu, E., Peyron, O., Revel, M., Sadori, L., Siani, G., Sicre, M. A., Samartin, S., Simonneau, A., Tinner, W., Vannière, B., Wagner, B., … Wirth, S. (2013). North-south palaeohydrological contrasts in the central mediterranean during the holocene: Tentative synthesis and working hypotheses. *Climate of the Past*, *9*(5), 2043–2071. https://doi.org/10.5194/cp-9-2043-2013
Magny, M., de Beaulieu, J. L., Drescher-Schneider, R., Vannière, B., Walter-Simonnet, A. V., Miras, Y., Millet, L., Bossuet, G., Peyron, O., Brugiapaglia, E., & Leroux, A. (2007). Holocene climate changes in the central Mediterranean as recorded by lake-level fluctuations at Lake Accesa (Tuscany, Italy). *Quaternary Science Reviews*, *26*(13–14), 1736–1758. https://doi.org/10.1016/j.quascirev.2007.04.014
Makri, S., Lami, A., Tu, L., Tylmann, W., Vogel, H., & Grosjean, M. (2021b). Holocene phototrophic community and anoxia dynamics in meromictic Lake Jaczno (NE Poland) using high-resolution hyperspectral imaging and HPLC data. *Biogeosciences*, *18*(5), 1839–1856. https://doi.org/10.5194/bg-18-1839-2021
Makri, S., Rey, F., Gobet, E., Gilli, A., Tinner, W., & Grosjean, M. (2020). Early human impact in a 15,000-year high-resolution hyperspectral imaging record of paleoproduction and anoxia from a varved lake in Switzerland. *Quaternary Science Reviews*, *239*, 106335. https://doi.org/10.1016/j.quascirev.2020.106335
Makri, S., Wienhues, G., Bigalke, M., Gilli, A., Rey, F., Tinner, W., Vogel, H., & Grosjean, M. (2021a). Variations of sedimentary Fe and Mn fractions under changing lake mixing regimes, oxygenation

and land surface processes during Late-glacial and Holocene times. *Science of the Total Environment*, *755*(xxxx), 143418. https://doi.org/10.1016/j.scitotenv.2020.143418

Martín-Forés, I., Magro, S., Bravo-Oviedo, A., Alfaro-Sánchez, R., Espelta, J. M., Frei, T., Valdés-Correcher, E., Rodríguez Fernández-Blanco, C., Winkel, G., Gerzabek, G., González-Martínez, S. C., Hampe, A., & Valladares, F. (2020). Spontaneous forest regrowth in South-West Europe: Consequences for nature's contributions to people. *People and Nature*, *2*(4), 980–994. https://doi.org/10.1002/pan3.10161

Massaferro, J. (1994). *Paleolimnologia di sei laghi vulcanici italiani e di un lago argentino di origine glaciale*. Dissertation, University of Parma.

Metzeltin, S., & Vezzoli, L. (1983). Contributi alla geologia del vulcano di Latera (Monti Vulsini, Toscana meridionale-Lazio settentrionale). *Memorie Della Società Geologica Italiana*, *25*, 247–271.

Mills, K., Schillereff, D., Saulnier-Talbot, É., Gell, P., Anderson, N. J., Arnaud, F., Dong, X., Jones, M., McGowan, S., Massaferro, J., Moorhouse, H., Perez, L., & Ryves, D. B. (2017). Deciphering long-term records of natural variability and human impact as recorded in lake sediments: a palaeolimnological puzzle. *Wiley Interdisciplinary Reviews: Water*, *4*(2), e1195. https://doi.org/10.1002/wat2.1195

Nappi, G., Renzulli, A., Santi, P., & Gillot, P.-Y. (1995). *Geological evolution and geochronology of the Vulsini Volcanic District (Central Italy)*.

Oksanen, A. J., Blanchet, F. G., Friendly, M., Kindt, R., Legendre, P., Mcglinn, D., Minchin, P. R., Hara, R. B. O., Simpson, G. L., Solymos, P., Stevens, M. H. H., & Szoecs, E. (2020). Vegan: Community Ecology Package. *Encyclopedia of Food and Agricultural Ethics*, 2395–2396. https://doi.org/10.1007/978-94-024-1179-9_301576

Ooms, J. (2021). *magick: Advanced Graphics and Image-Processing in R. R package version 2.7.3*. https://cran.r-project.org/package=magick

Palmisano, A., Bevan, A., Kabelindde, A., Roberts, N., & Shennan, S. (2021). Long-Term Demographic Trends in Prehistoric Italy: Climate Impacts and Regionalised Socio-Ecological Trajectories. In *Journal of World Prehistory* (Vol. 34). https://doi.org/10.1007/s10963-021-09159-3

Passariello, I., Albore Livadie, C., Talamo, P., Lubritto, C., D'Onofrio, A., & Terrasi, F. (2009). 14C Chronology of avellino pumices eruption and timing of human reoccupation of the devastated region. *Radiocarbon*, *51*(2), 803–816. https://doi.org/10.1017/S0033822200056113

Pedrotta, T., Gobet, E., Schwörer, C., Beffa, G., Butz, C., Henne, P. D., Morales, C., Salvatore, M., Jacqueline, P., Hendrik, F. N. V. L., Elias, V., Anselmetti, F. S., Grosjean, M., & Tinner, W. (2021). 8 , 000 years of climate , vegetation , fire and land - use dynamics in the thermo - mediterranean vegetation belt of northern Sardinia (Italy). *Vegetation History and Archaeobotany*. https://doi.org/10.1007/s00334-021-00832-3

Pellegrini, E. (1993). Aspetti della metallurgia nel comprensorio del lago di Mezzano e nella media valle del Fiora dal Bronzo Antico all'XI sec. aC. *AC In: Vulcano a Mezzano-Insediamento e Produzioni Artigianali Nella Media Valle Del Fiora Durante l'et" a Del Bronzo. Comune Di Valentano-Museo Civico, Collana Di Studi, Testi e Cataloghi*, 73–85.

Petitti, P. (2000). La Caldera di Latera: appunti su materiali di nuova scoperta e contatti a lunga distanza. *Preistoria e Protostoria in Etruria. Atti Del IV Incontro Di Studi. Milano*, 141–149.

Petitti, P., & Mitchell, E. (1993). Dati preliminari sulla topografia dell'abitato sommerso del Lago di Mezzano. *Vulcano a Mezzano-Insediamento e Produzioni Artigianali Nella Media Valle Del Fiora Nell 'Eta Del Bronzo. Museo Civico, Valentano*, 17–31.

Philippsen, B. (2013). The freshwater reservoir effect in radiocarbon dating. *Heritage Science*, *1*(1), 1–19. https://doi.org/10.1186/2050-7445-1-24

Pichler, H. (1989). *Italienische Vulkangebiete V*. Schweizerbart Science Publishers. http://www.schweizerbart.de//publications/detail/isbn/9783443150501/Bd_83_Sammlung_Geol_Fuhrer_Ital_Vulk

R Core Team. (2021). *R: A language and environment for statistical computing*. R Foundation for Statistical Computing, Vienna, Austria. https://www.r-project.org/

Radi, G., & Petrinelli Pannocchia, C. (2018). The beginning of the Neolithic era in Central Italy. *Quaternary International*, *470*, 270–284. https://doi.org/10.1016/j.quaint.2017.06.063

Ramrath, A. (1997). *Laminierte Sedimente des Lago di Mezzano (Latium, Italien) - Limnogeologie und Rekonstruktion von Umweltbedingungen der letzten 34.000 Jahre*. (p. 108). Unpub. thesis.

Ramrath, A., Nowaczyk, N. R., & Negendank, J. F. W. (1999a). Sedimentological evidence for

environmental changes since 34,000 years BP from Lago di Mezzano, central Italy. *Journal of Paleolimnology*, *21*(4), 423–435.

Ramrath, A., Sadori, L., & Negendank, J. F. W. (2000). Sediments from Lago di Mezzano, central Italy: A record of Lateglacial/Holocene climatic variations and anthropogenic impact. *Holocene*, *10*(1), 87–95. https://doi.org/10.1191/095968300669348734

Ramrath, A., Zolitschka, B., Wulf, S., & Negendank, J. F. W. (1999b). Late pleistocene climatic variations as recorded in two Italian maar lakes (Lago di Mezzano, Lago Grande di Monticchio). *Quaternary Science Reviews*, *18*(7), 977–992. https://doi.org/10.1016/S0277-3791(99)00009-8

Ramsey, C. B., Albert, P. G., Blockley, S. P. E., Hardiman, M., Housley, R. A., Lane, C. S., Lee, S., Matthews, I. P., Smith, V. C., & Lowe, J. J. (2015). Improved age estimates for key Late Quaternary European tephra horizons in the RESET lattice. *Quaternary Science Reviews*, *118*, 18–32. https://doi.org/10.1016/j.quascirev.2014.11.007

Read, E. K., Patil, V. P., Oliver, S. K., Hetherington, A. L., Brentrup, J. A., Zwart, J. A., Winters, K. M., Corman, J. R., Nodine, E. R., Woolway, R. I., Dugan, H. A., Jaimes, A., Santoso, A. B., Hong, G. S., Winslow, L. A., Hanson, P. C., & Weathers, K. C. (2015). The importance of lake-specific characteristics for water quality across the continental United States. *Ecological Applications*, *25*(4), 943–955. https://doi.org/10.1890/14-0935.1

Regattieri, E., Zanchetta, G., Drysdale, R. N., Isola, I., Hellstrom, J. C., & Dallai, L. (2014). Lateglacial to Holocene trace element record (Ba, Mg, Sr) from Corchia Cave (Apuan Alps, central Italy): Paleoenvironmental implications. *Journal of Quaternary Science*, *29*(4), 381–392. https://doi.org/10.1002/jqs.2712

Reimer, P. J., Austin, W. E. N., Bard, E., Bayliss, A., Blackwell, P. G., Bronk Ramsey, C., Butzin, M., Cheng, H., Edwards, R. L., Friedrich, M., Grootes, P. M., Guilderson, T. P., Hajdas, I., Heaton, T. J., Hogg, A. G., Hughen, K. A., Kromer, B., Manning, S. W., Muscheler, R., … Talamo, S. (2020). The IntCal20 Northern Hemisphere Radiocarbon Age Calibration Curve (0-55 cal kBP). *Radiocarbon*, *62*(4), 725–757. https://doi.org/10.1017/RDC.2020.41

Rinke, K., Keller, P. S., Kong, X., Borchardt, D., & Weitere, M. (2019). Ecosystem services from inland waters and their aquatic ecosystems. In *Atlas of Ecosystem Services* (pp. 191–195). Springer.

Rothwell, R. G., & Croudace, I. w. (2015). *Micro-XRF Studies of Sediment Cores: A Perspective on Capability and Application in the Environmental Sciences*. https://doi.org/10.1007/978-94-017-9849-5_1

Sadori, L. (2018). The Lateglacial and Holocene vegetation and climate history of Lago di Mezzano (central Italy). *Quaternary Science Reviews*, *202*, 30–44. https://doi.org/10.1016/j.quascirev.2018.09.004

Sadori, L., Giraudi, C., Petitti, P., & Ramrath, A. (2004). Human impact at Lago di Mezzano (central Italy) during the Bronze Age: A multidisciplinary approach. *Quaternary International*, *113*(1), 5–17. https://doi.org/10.1016/S1040-6182(03)00077-6

Samartin, S., Heiri, O., Lotter, A. F., & Tinner, W. (2012). Climate warming and vegetation response after Heinrich event 1 (16,700-16,000 cal yr BP) in Europe south of the Alps. *Climate of the Past*, *8*(6), 1913–1927. https://doi.org/10.5194/cp-8-1913-2012

Samartin, Stéphanie, Heiri, O., Joos, F., Renssen, H., Franke, J., Brönnimann, S., & Tinner, W. (2017). Warm Mediterranean mid-Holocene summers inferred from fossil midge assemblages. *Nature Geoscience*, *10*(3), 207–212. https://doi.org/10.1038/ngeo2891

Samartin, Stéphanie, Heiri, O., Kaltenrieder, P., Kühl, N., & Tinner, W. (2016). Reconstruction of full glacial environments and summer temperatures from Lago della Costa, a refugial site in Northern Italy. *Quaternary Science Reviews*, *143*, 107–119. https://doi.org/10.1016/j.quascirev.2016.04.005

Sanchini, A., Szidat, S., Tylmann, W., Vogel, H., Wacnik, A., & Grosjean, M. (2020). A Holocene high-resolution record of aquatic productivity, seasonal anoxia and meromixis from varved sediments of Lake Łazduny, North-Eastern Poland: insight from a novel multi-proxy approach. *Journal of Quaternary Science*, *35*(8), 1070–1080. https://doi.org/10.1002/jqs.3242

Saunders, K. M., Roberts, S. J., Perren, B., Butz, C., Sime, L., Davies, S., Van Nieuwenhuyze, W., Grosjean, M., & Hodgson, D. A. (2018). Holocene dynamics of the Southern Hemisphere westerly winds and possible links to CO2 outgassing. *Nature Geoscience*, *11*(9), 650–655. https://doi.org/10.1038/s41561-018-0186-5

Sayer, C. D., Davidson, T. A., Rawcliffe, R., Langdon, P. G., Leavitt, P. R., Cockerton, G., Rose, N. L., & Croft, T. (2016). Consequences of Fish Kills for Long-Term Trophic Structure in Shallow Lakes: Implications for Theory and Restoration. *Ecosystems*, *19*(7), 1289–1309. https://doi.org/10.1007/s10021-016-0005-z

Schnurrenberger, D., Russell, J., & Kelts, K. (2003). Classification of lacustrine sediments based on sedimentary components. *Journal of Paleolimnology*, *29*(2), 141–154. https://doi.org/10.1023/A:1023270324800

Schüler, G. (2006). Identification of flood-generating forest areas and forestry measures for water retention. *Forest Snow and Landscape Research*, *80*(1), 99–114.

Sevink, J., van Bergen, M. J., van der Plicht, J., Feiken, H., Anastasia, C., & Huizinga, A. (2011). Robust date for the Bronze Age Avellino eruption (Somma-Vesuvius): 3945 ± 10 calBP (1995 ± 10 calBC). *Quaternary Science Reviews*, *30*(9–10), 1035–1046. https://doi.org/10.1016/j.quascirev.2011.02.001

Smol, J. P. (2008). Pollution of Lakes and Rivers. In *Library*.

Stoddart, S., Woodbridge, J., Palmisano, A., Mercuri, A. M., Mensing, S. A., Colombaroli, D., Sadori, L., Magri, D., Di Rita, F., Giardini, M., Mariotti Lippi, M., Montanari, C., Bellini, C., Florenzano, A., Torri, P., Bevan, A., Shennan, S., Fyfe, R., & Roberts, C. N. (2019). Tyrrhenian central Italy: Holocene population and landscape ecology. *Holocene*, *29*(5), 761–775. https://doi.org/10.1177/0959683619826696

Swain, E. B. (1985). Measurement and interpretation of sedimentary pigments. *Freshwater Biology*, *15*(1), 53–75. https://doi.org/10.1111/J.1365-2427.1985.TB00696.X

Tu, L., Jarosch, K. A., Schneider, T., & Grosjean, M. (2019). Phosphorus fractions in sediments and their relevance for historical lake eutrophication in the Ponte Tresa basin (Lake Lugano, Switzerland) since 1959. *Science of the Total Environment*, *685*, 806–817. https://doi.org/10.1016/j.scitotenv.2019.06.243

Tylmann, W., Fischer, H. W., Enters, D., Kinder, M., Moska, P., Ohlendorf, C., Poreba, G., & Zolitschka, B. (2014). Reply to the comment by F. Gharbi on "Multiple dating of varved sediments fromLake Łazduny, northern Poland: Toward an improved chronology for the last150 years." *Quaternary Geochronology*, *20*, 111–113. https://doi.org/10.1016/j.quageo.2013.04.003

Wanner, H., Solomina, O., Grosjean, M., Ritz, S. P., & Jetel, M. (2011). Structure and origin of Holocene cold events. *Quaternary Science Reviews*, *30*(21–22), 3109–3123. https://doi.org/10.1016/j.quascirev.2011.07.010

Weingartner, R., Barbena, M., & Spreafico, M. (2003). Floods in mountain areas - An overview based on examples from Switzerland. *Journal of Hydrology*, *282*(1–4), 10–24. https://doi.org/10.1016/S0022-1694(03)00249-X

Wetzel, R. G. (2001). *Limnology: lake and river ecosystems* (3rd ed.). Academic Press.

Wickham, C. (2018). *munsell: utilities for using munsell colours*. https://cran.r-project.org/package=munsell

Wickham, H. V. (2016). ggplot2: Elegant graphics for data analysis. In *ggplot2 elegant graphics for data analysis*. Springer. https://ggplot2.tidyverse.org

Wienhues, G. (2019). *Multi-proxy reconstruction of Holocene environmental change from sediments of Lake Rześniki , Northeast Poland*. University of Bern.

Wilke, C. O. (2020). *cowplot: Streamlined Plot Theme and Plot Annotations for "ggplot2"*. 1–44. https://cran.r-project.org/web/packages/cowplot/index.html

Wilkes, H., Ramrath, A., & Negendank, J. F. W. (1999). Organic geochemical evidence for environmental changes since 34,000 yrs BP from Lago di Mezzano, central Italy. *Journal of Paleolimnology*, *22*(4), 349–365. https://doi.org/10.1023/A:1008051821898

Woolway, R. I., Kraemer, B. M., Lenters, J. D., Merchant, C. J., O'Reilly, C. M., & Sharma, S. (2020). Global lake responses to climate change. *Nature Reviews Earth & Environment*, *1*(8), 388–403. https://doi.org/10.1038/s43017-020-0067-5

Woolway, R. I., & Merchant, C. J. (2019). Worldwide alteration of lake mixing regimes in response to climate change. *Nature Geoscience*, *12*(4), 271–276. https://doi.org/10.1038/s41561-019-0322-x

Yurkov, V. V., & Beatty, J. T. (1998). Aerobic Anoxygenic Phototrophic Bacteria. *Microbiology and Molecular Biology Reviews*, *62*(3), 695–724. https://doi.org/10.1128/mmbr.62.3.695-724.1998

Zanchetta, G., Drysdale, R. N., Hellstrom, J. C., Fallick, A. E., Isola, I., Gagan, M. K., & Pareschi, M. T. (2007). Enhanced rainfall in the Western Mediterranean during deposition of sapropel S1: stalagmite evidence from Corchia cave (Central Italy). *Quaternary Science Reviews*, *26*(3–4), 279–286. https://doi.org/10.1016/j.quascirev.2006.12.003

Zanchetta, G., Regattieri, E., Isola, I., Drysdale, R. N., Bini, M., Baneschi, I., & Hellstrom, J. C. (2016). The so-called "4.2 event" in the central Mediterranean and its climatic teleconnections. *Alpine and Mediterranean Quaternary*, *29*(1), 5–17.

Zanchetta, G., Sulpizio, R., Roberts, N., Cioni, R., Eastwood, W. J., Siani, G., Caron, B., Paterne, M., &

Santacroce, R. (2011). Tephrostratigraphy, chronology and climatic events of the Mediterranean basin during the Holocene: An overview. *Holocene*, *21*(1), 33–52. https://doi.org/10.1177/0959683610377531

Zander, P. D., Żarczyński, M., Vogel, H., Tylmann, W., Wacnik, A., Sanchini, A., & Grosjean, M. (2021). A high-resolution record of Holocene primary productivity and water-column mixing from the varved sediments of Lake Żabińskie, Poland. *Science of the Total Environment*, *755*(xxxx). https://doi.org/10.1016/j.scitotenv.2020.143713

Zepner, L., Karrasch, P., Wiemann, F., & Bernard, L. (2021). ClimateCharts.net–an interactive climate analysis web platform. *International Journal of Digital Earth*, *14*(3), 338–356. https://doi.org/10.1080/17538947.2020.1829112

Appendix

A Sediment cores

Table A 1: Cores retrieved in 2019 and 2020 from Lago di Mezzano.

Core name	*Coordinates*		*Water depth*	*Core length*	*Coring date*	*Diameter*
MZZ-A	42°36'47.0" N	011°46'10.0" E	31.4 m	15 m	04.05.19	6 cm
MZZ-B	42°36'47.1" N	011°46'09.9" E	31.4 m	10 m	04.05.19	9 cm
MZZ-C	42°36'47.1" N	011°46'10.2" E	31.4 m	12 m	05.05.19	6 cm
MZZ-D	42°36'47.1" N	011°46'10.1" E	31.4 m	12 m	06.05.19	6 cm
Surface 2019	42°36'47.1" N	011°46'10.1" E	31.4 m	-	06.05.19	6 cm
MZZ-E	42°36'42.9"N	11°46'12.1"E	30.4 m	9 m	02.09.20	6 cm
MZZ-F	42°36'42.9"N	11°46'12.0"E	30.4 m	8 m	02.09.20	9 cm
MZZ-G	42°36'42.8"N	11°46'12.0"E	30.4 m	6 m	03.09.20	9 cm
MZZ-H	42°36'42.8"N	11°46'12.1"E	30.4 m	6 m	03.09.20	9 cm
Surface 2020	42°36'42.8"N	11°46'12.1"E	30.4 m	-	03.09.20	9 cm

Table A 2: Stratigraphic correlation of the master core and XRF scanning year and resolution. Cores in grey are not part of the master core but were scanned. A indicates the archive core half whereas W specifies the working core half.

Core segment name	*Master depth segment top*	*Master depth segment bottom*	*Core depth segment top*	*Core depth segment bottom*	*XRF scanning year & resolution*
MZZ_Sur_A_2019	0	21	0	21	2019, 5 mm
MZZ_Sur_W_2019	0	21	0	21	2021 2 mm
MZZ_Sur_2_W_2020	0	21	0	21	2021, 2mm
MZZ_A_0_1_A	21	73.985	20	72.985	2019, 5 mm
MZZ_A_1_2_A	73.985	174.618	0	100.633	2019, 5 mm
MZZ_A_2_3_A	174.618	202.618	0	28	2019, 5 & 1 mm
MZZ_G_1_2_A	202.618	225.289	32	54.671	2020, 5 mm
MZZ_G_2_3_A	225.289	281.289	0	56	2020, 5 mm
MZZ_F_2_3_A	281.289	310.289	34.5	63.5	2020, 5 mm
MZZ_F_3_4_W	310.289	399.289	0	89	2020, 0.2 mm
MZZ_G_4_5_W	399.289	492.289	0	93	2020, 0.2 mm
MZZ_F_4_5_W	492.289	514.889	42	64.6	2020, 0.2 mm
MZZ_F_5_6_A	514.889	609.889	0	95	2020, 5 & 0.2 mm
MZZ_B_6_8_Neolithic	609.889	699.889	62	152	2020, 5 & 0.2 mm
MZZ_C_7_5_8_5_A	699.889	770.68	29	99.791	2019, 5 mm
MZZ_C_8_5_9_5_A	770.68	799.18	0	28.5	2019, 5 mm
MZZ_D_8_5_9_5_W	799.18	879.68	11.5	92	2020, 5 mm
MZZ_A_9_10_A	879.68	926.68	21	68	2019, 5 mm
MZZ_C_9_5_10_5_A	926.68	991.639	30	94.959	2019, 5 mm
MZZ_C_10_5_11_5_A	991.639	1091.372	0	99.733	2019, 5 mm
MZZ_C_11_5_12_5_A	1091.372	1191.347	0	99.975	2019, 5 mm

Table A 3: Stratigraphic correlation of the U-channels in the Bronze Age case-study section.

Block number	*Block name*	*Distance from upper left corner of the resin block to the 2 mm scanning area [mm]*	*Zero block depth in the µXRF log [cm]*	*Block depth segment top [cm]*	*Block depth segment bottom [cm]*	*Core depth segment top [cm]*	*Master depth segment top [cm]*	*Length resin block [cm]*	*Length fresh block (µXRF) [cm]*	*Start of the fresh block in block depth (zero at start resin) [cm]*	*Length fresh block (HSI) [cm]*
1	MZZ_F_3_4_312	6.000	0.175	0	16.940	0.000	310.289	18.085	18.232	-0.073	18.590
2	MZZ_F_3_4_328	10.000	0.15	1.13	16.890	16.940	327.229	18.040	18.266	-0.113	18.590
3	MZZ_F_3_4_344	9.975	0.14	0.98	16.675	32.700	342.989	18.170	18.260	-0.045	18.580
4	MZZ_F_3_4_360	9.975	0.175	0.86	17.170	48.395	358.684	18.100	18.173	-0.037	18.538
5	MZZ_F_3_4_376	6.000	0.17	1.045	16.995	64.705	374.994	18.140	18.226	-0.043	18.598
6	MZZ_F_3_4_392	11.700	0.155	1.355	16.165	80.655	390.944	18.165	18.216	-0.026	18.508
7	MZZ_G_4_5_400	10.150	0.24	6.51	16.960	6.465	405.754	18.135	18.230	-0.047	18.530
8	MZZ_G_4_5_416	10.375	0.19	1.74	17.040	16.915	416.204	18.070	18.202	-0.066	18.620
9	MZZ_G_4_5_432	10.225	0.3	1.37	17.635	32.215	431.504	18.050	18.209	-0.079	18.633
10	MZZ_G_4_5_448	9.775	0.25	1.595	17.805	48.480	447.769	18.090	18.240	-0.075	18.588
11	MZZ_G_4_5_464	9.975	0.18	1.845	16.595	64.690	463.979	18.115	18.215	-0.050	18.540
12	MZZ_G_4_5_480	10.575	0.21	0.685	12.205	79.440	478.729	18.105	18.208	-0.051	18.590
13	MZZ_F_4_5_491	9.500	0.21	1.105	18.070	39.960	490.249	18.070	18.240	-0.085	18.460

B1 Chronology

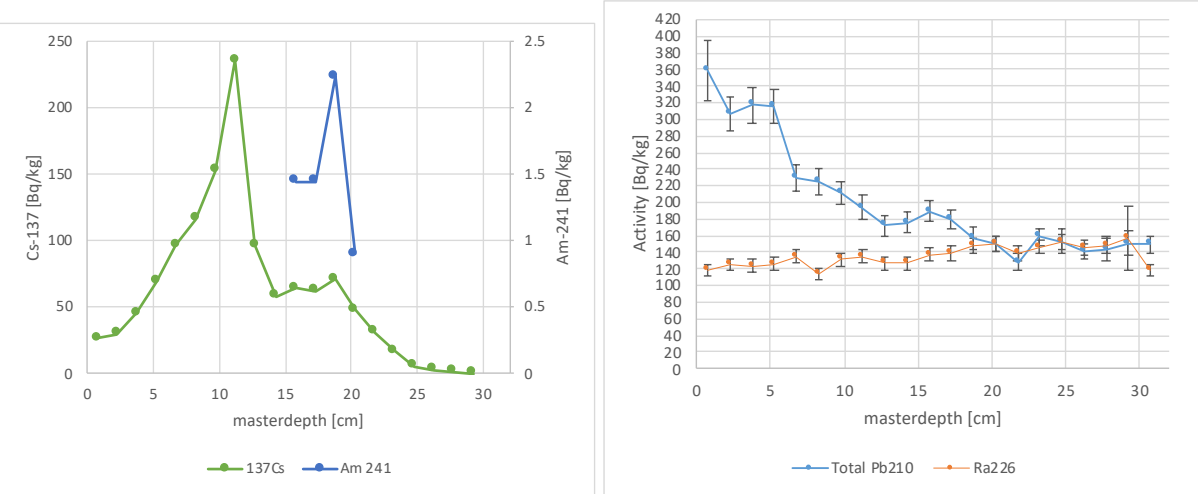

Fig. A 1: Radioisotope profiles of core MZZ Sur W 2019 (table A2). Left panel: Cs-137 and Am-241 activity profiles. Peak activities are connected to the Chernobyl accident (1986) and the peak fallout of nuclear weapons testing (1963). Right panel: total Pb-210 and Ra-226 activity.

Table A 4: Pb-210 CRS-model results. Model constrained to 1963 nuclear bomb peak. Note that the Chernobyl chrono marker is within the age uncertainty of the model.

Age			***Mass accumulation rate***			***Date***	***Masterdepth***	***Chrono marker***
t	*+/-*	*2*SD*	*MAR*	*+/-*	*MAR 2*SD*			
yrs	*yrs*	*yrs*	*g/cm2y*	*%*	*g/cm2y*	*year CE*	*cm*	*year CE*
0	0	0				2019.4	0	
4.697	1.370	2.740	0.119	15.869	0.019	2014.7	0.75	
9.393	1.993	3.987	0.137	13.918	0.019	2010.0	2.25	
13.977	2.344	4.687	0.111	13.942	0.015	2005.4	3.75	
19.155	2.776	5.552	0.096	15.104	0.015	2000.2	5.25	
24.214	3.254	6.509	0.166	21.586	0.036	1995.2	6.75	
27.317	3.577	7.153	0.129	18.992	0.024	1992.1	8.25	
31.184	4.033	8.066	0.159	23.403	0.037	1988.2	9.75	
35.264	4.575	9.150	0.188	30.205	0.057	1984.1	11.25	Chernobyl 1986
39.287	5.148	10.296	0.214	34.970	0.075	1980.1	12.75	
43.896	5.879	11.758	0.173	34.474	0.060	1975.5	14.25	
48.090	6.572	13.145	0.140	33.830	0.047	1971.3	15.75	
52.848	7.544	15.089	0.155	40.996	0.063	1966.6	17.25	
56.400	8.313	16.627	0.564	161.722	0.912	1963.0	18.75	Bomb peak 1963

Table A 5: Calibrated age dates used for the chronology. CC indicates if the age dates were calibrated here (1) using IntCal20 or if they were already calibrated before (0). All ages are given in years BP (before 1950).

Name	*Depth [cm]*	*Mean*	*Upper95*	*Lower95*	*cc*
Surface	0	-69.4	-68	-70	0
MZZ_Cs_Chernobyl	11.25	-36.0	-34	-38	0
MZZ_Cs_bombPeak	18.75	-13.0	-11	-15	0
BE-16311.1.1	290	1033.3	940	1171	1
BE-16312.1.1	292	1115.1	979	1256	1
BE-16313.1.1	489	3661.4	3510	3816	1
Avellino_Tehpra_Zanchetta_etal_2011	524	3802.4	3698	3932	1
Avellino_Tehpra_Passariello_etal_2009	524	3833.1	3731	3901	1
Avellino_Tehpra_Sevik_etal_2011	524	3838.0	3858	3818	0
BE-13846.1.1	600.5	5163.4	4991	5275	1
BE-13847.1.1	600.5	5162.9	4992	5275	1
BE-13845.1.1	602.5	5149.2	4981	5281	1
BE-13844.1.1	608.5	5160.0	5056	5290	1
BE-13843.1.1	611.5	5166.7	5051	5300	1
BE-13290.1.1	613	5162.7	5059	5299	1
BE-13841.1.1	614	5179.6	5063	5305	1
BE-13289.1.1	621	5406.3	5331	5557	1
BE-13840.1.1	622.5	5533.4	5478	5598	1
BE-13839.1.1	630	5757.9	5617	5885	1
BE-13838.1.1	636.5	5814.7	5693	5900	1
BE-13837.1.1	638.5	5845.8	5752	5975	1
BE-13836.1.1	641.5	5965.0	5925	6089	1
BE-13835.1.1	655	6233.7	6126	6290	1
BE-13834.1.1	658.5	6383.2	6312	6477	1
BE-13833.1.1	659.5	6414.3	6327	6481	1
BE-13832.1.1	661.5	6433.2	6359	6486	1
BE-13287.1.1	662.5	6461.9	6409	6534	1
BE-13288.1.1	662.5	6467.8	6410	6543	1
BE-13831.1.1	664.5	6524.3	6452	6616	1
BE-13830.1.1	665.5	6535.1	6444	6629	1
BE-13829.1.1	669	6635.6	6509	6738	1
BE-13286.1.1	682	6819.7	6735	6922	1
BE-13828.1.1	683	7028.2	6909	7151	1
BE-13285.1.1	684.5	7063.5	6957	7156	1
BE-13827.1.1	685	7161.5	6938	7395	1
BE-16570.1.1	699.75	7318.6	7198	7414	1
BE-16571.1.1	710.75	7524.9	7436	7616	1
BE-16572.1.1	718.25	7670.1	7609	7747	1
BE-16573.1.1	718.75	7650.4	7584	7744	1
BE-16574.1.1	722.25	7751.7	7670	7898	1
BE-16575.1.1	729.25	7824.8	7703	7929	1
BE-16576.1.1	736.25	7929.5	7833	8011	1
BE-16577.1.1	742.25	8079.4	7977	8170	1
BE-16578.1.1	742.75	8079.0	7988	8165	1
BE-16579.1.1	744.25	8100.2	8025	8170	1
BE-16580.1.1	749.25	8262.0	8077	8367	1
BE-16581.1.1	756.75	8398.2	8229	8530	1
BE-16314.1.1	811	9322.1	9045	9521	1
BE-16315.1.1	940	12940.9	12753	13153	1
Randazzo_Polverello_Tephra	1161	18106.0	18226	17986	0
BE-16316.1.1	1169	16959.2	16433	17433	1

B2 Mass accumulation rate (MAR)

Linear model results for dry density proxy based on Ti

```
# Call:
#   lm(formula = DD_g_cm3 ~ Ti, data = Data_full)
#
# Residuals:
#   Min        1Q    Median        3Q       Max
# -0.267759 -0.040706  0.001776  0.038591  0.311364
#
# Coefficients:
#   Estimate Std. Error t value Pr(>|t|)
# (Intercept) 1.488e-01  1.484e-02   10.03   <2e-16 ***
#   Ti          2.575e-06  1.458e-07   17.66   <2e-16 ***
#   ---
#   Signif. codes:  0 ‘***’ 0.001 ‘**’ 0.01 ‘*’ 0.05 ‘.’ 0.1 ‘ ’ 1
#
# Residual standard error: 0.07877 on 147 degrees of freedom
# Multiple R-squared:  0.6795,     Adjusted R-squared:  0.6774
# F-statistic: 311.7 on 1 and 147 DF,  p-value: < 2.2e-16
```

MAR proxy

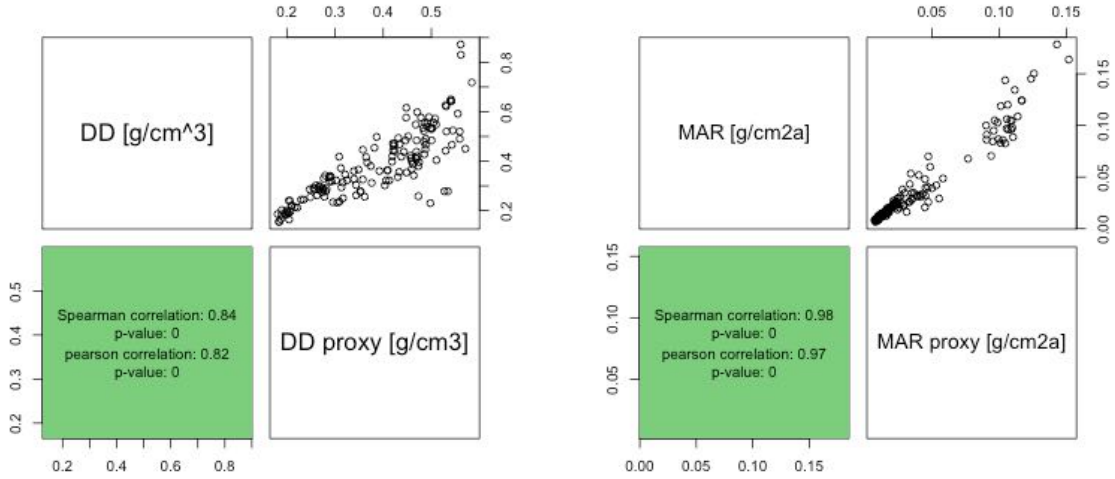

Fig. A 2: left panel: DD and DD proxy, right panel: MAR and MAR proxy

C Sediment description

Table A 6: Smear slides.

Nr	Name	Depth	Description Core	Percentage minerals	Percantage OM	Percantage Diatoms	Minerals description	Other notes
1	MZZ-A 0-1 20cm	21		50%: fine grained, clear clastic material rounded, subrounded <10µm	50%	10%	iron oxide (Hematite, abundant), Siderit (rare), Feldspar (dominant), Calcit (very rare, angular)	
2	MZZ-A 1-2 44.5cm	118	smear slide, 44.5, grey layer	70% fine grained <10µm, clear and dark clastic material rounded	30%	10%	iron oxide (abundant), Siderit (abundant), Feldspar (abundant)	
3	MZZ-A 1-2 46.5cm	120	smear slide, 46.5, light brown layer/ bright layer	80% fine grained <10µm, clear and dark clastic material rounded	20	10	iron oxide, Feldspar, Quarz,	Charcoal 10-20µm
4	MZZ-A 1-2 80cm	154	smear slide, 80, average massive	60%, dine grained <10µm, clear, rounded	40	15	iron oxide, Feldspar	
5	MZZ-A 2-3 28cm	202	smear slide of brown layer	50 fine grained <10cm, white colors	50	10	iron oxide, Feldspar, some glass shards	
6	MZZ-G 2-3 37.5cm	262	smearslide 37.5, light layer	50	50	7	iron, Fedspar, Siderit	
7	MZZ-G 2-3 53cm	278	Vivianite	50	50	7	iron, Vivianate (very abundant)	
8	MZZ-F 3-4 12.5cm	322	thick bed	50	50	30	iron, Feldspar	Sponge spicules
9	MZZ-F 3-4 36.5cm	346	36.5, one >dark< brown and one light brown layer of possibly varve	50	50	30	iron, Feldspar	Sponge spicules
10	MZZ-F 3-4 36.5cm	346	36.5, one dark brown and one >light< brown layer of possibly varve	40	60	20	dominant iron oxide, low Feldspar	Sponge spicules
11	MZZ-G 4-5 33.5cm	432	smear slide 33.5, dark and light layer (brighter lamina type)	80, <10µm, rounded, bright dminant, few dark minearls	15	5	Feldspar, no iron oxid	red mineral
12	MZZ-G 4-5 33.5cm	432	smear slide 33.5, dark and light layer (brighter lamina type)	80, <10µm, rounded, bright dminant, few dark minearls	20	20	iron oxide, pyrit, Feldspar	
13	MZZ-G 4-5 80cm	479	smear slide 80, dark layer, darker lamina type	40	60	40	Feldspar, low iron oxid	few charcoal, plant remains
14	MZZ-G 4-5 80cm	479	smear slide 80, light layer, darker lamina type	50	50	50	Feldspar	plant remains
15	-	524	light grey layer, Smear slide Giorgia at IPS, of light layer => ev. Avellino Tephra from Somma/Vesuv					
16	MZZ-F 5-6 50cm	565	smear slide, massive section	20	50	70	Few Calcite, Feldspar, iron oxide	Diatom tubes with chambers everywhere, Sponge spicules, plant remains
17	MZZ-B 7-8 19cm	606	smearslide of light layer, 19cm MZZ-B 7-8	60, <10µm, rounded, bright and dark	40	10	Calcite, Feldspar, iron axide	plant remains
18	MZZ-B 7-8 19cm	606	smearslide of dark layer, 19cm MZZ-B 7-8	70% many minerals over 20µm, but also fine grains	30	7	Feldspar, Iron oxide	plant remains
19	MZZ-C 7.5-8.5 52cm	722	smear slide, mix dark and light of dark lamina	10 few feldspar, 10-20µm, rounded	30	50	few Feldspar, iron oxide	plant remains
20	MZZ-C 7.5-8.5 78cm	748	light color, smear slide of thl light layer	10, few feldspar 20µm rounded	60	50	few Feldspar, iron oxide, maybe Calcite	plant remains
21	MZZ-C 8.5-9.5 9cm	778	smear slide of light brown clay layer	90, bright minerals <10µm	10	20	Feldspar, Quarz, few iron oxide	few plant remains
22	MZZ-A 9-10 40cm	898	smear slide, representive mud	50, Feldspar >10µm rounded	50	30	Feldspar, Quarz, iron oxide	plant remains
23	MZZ-C 9.5-10.5 87cm	983	Smear slide of dark dentritus layers	40	40	15	Feldspar, iron oxide	plant remains
24	MZZ-C 10-5-11.5 45cm	1036	smear slide	60 fine and >20µm Feldspar rounded	40	10	Feldspar, lot of iron oxide	plant remains
25	MZZ-C 11.5-12.5 70cm	1161	smearslide => Biancavilla thephra (Mt. Etna), volcanic glass confermed!	90	10	7	Glasshards, Feldspar, unknown shiny/ redish mineral	
26	MZZ-C 11.5-12.5 95cm	1187	smearsilde, representive bottom	80	20	10	Feldspar, Quarz, iron oxide	plant remains

D1 HSI - vivianite

Table A 7: Non-vivianite classes in the spectral angle mapper (SAM) classification. SAM classes from 1-13 were classified as vivianite if they are not too noisy. The too noisy classes (>0) as well as the unclassified class (0) are presented in this table as the non-vivianite classes.

Core segment name	*Non-vivianite classes*	*Qualitative assessment of visible vivianite and performance of SAM*
MZZ_F_2_3_A	0	
MZZ_F_3_4_W	0,3	vivianite everywhere
MZZ_C_7_5_8_5_A	0,2,3	
MZZ_A_0_1_A	0,2,3	no vivianite at all
MZZ_A_1_2_A	0	no vivianite at all
MZZ_A_2_3_A	0	very few dark undetected vivianites
MZZ_A_9_10_A	0	no vivianite at all
MZZ_C_8_5_9_5_A	0,2,3	no vivianite at all
MZZ_C_9_5_10_5_A	0	more vivianite to bottom
MZZ_C_10_5_11_5_A	0	one vivianite
MZZ_C_11_5_12_5_A	0	vivianite everywhere
MZZ_D_8_5_9_5_W	0,2,3	no vivianite at all
MZZ_F_4_5_W	0,2,3	very few dark undetected vivianites
MZZ_F_5_6_A	0,3	few vivianites, especially in brighter part
MZZ_G_1_2_A	0	only one vivianite
MZZ_G_2_3_A	0	very few undetected vivianites
MZZ_G_4_5_W	0	bellow 460 cm master depth at Rmean <0.06 classes 2,3 are bad
MZZ_Sur_2019_W	0	no vivianite at all
MZZ_Sur_A	0	no vivianite at all
MZZ-B-7-8W	0,2,3	black vivianite not detected

D2 HSI - calibration

Spectrophotometer results

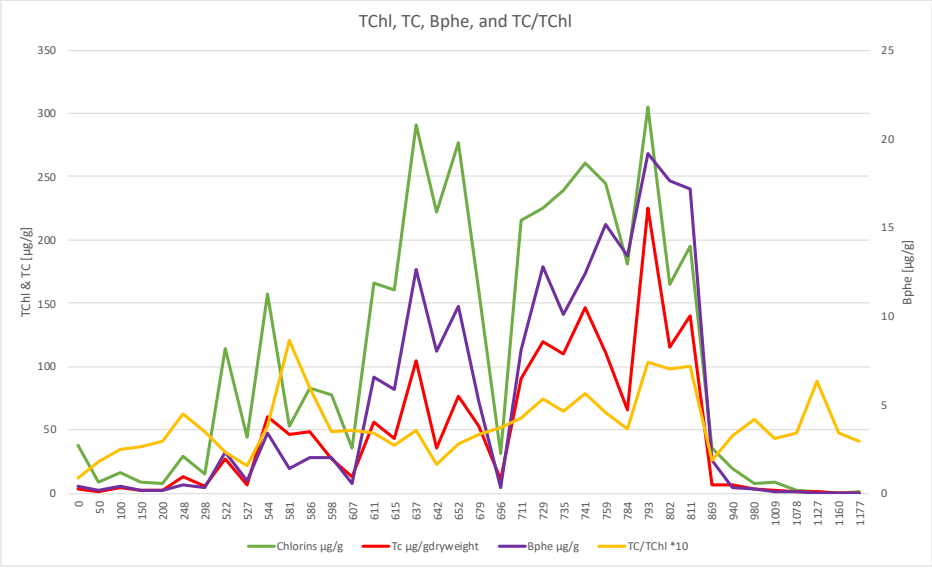

Fig. A 3: Spectrophotometer results.

The spectrophotometrically measured concentration of total carotenoids (TC) show a minimum of 0.1 $\mu g/g_{dry\ sediment}$ and a maximum of 225 $\mu g/g_{dry\ sediment}$. A study on Italian lakes related TC to phosphorous (P) concentration in the water column (Guilizzoni et al., 2011), thus high TC concentrations might show elevated P. In addition, we calculated the TC/TChl ratio which is an indicator for cyanobacteria or anoxia.

Linear model results

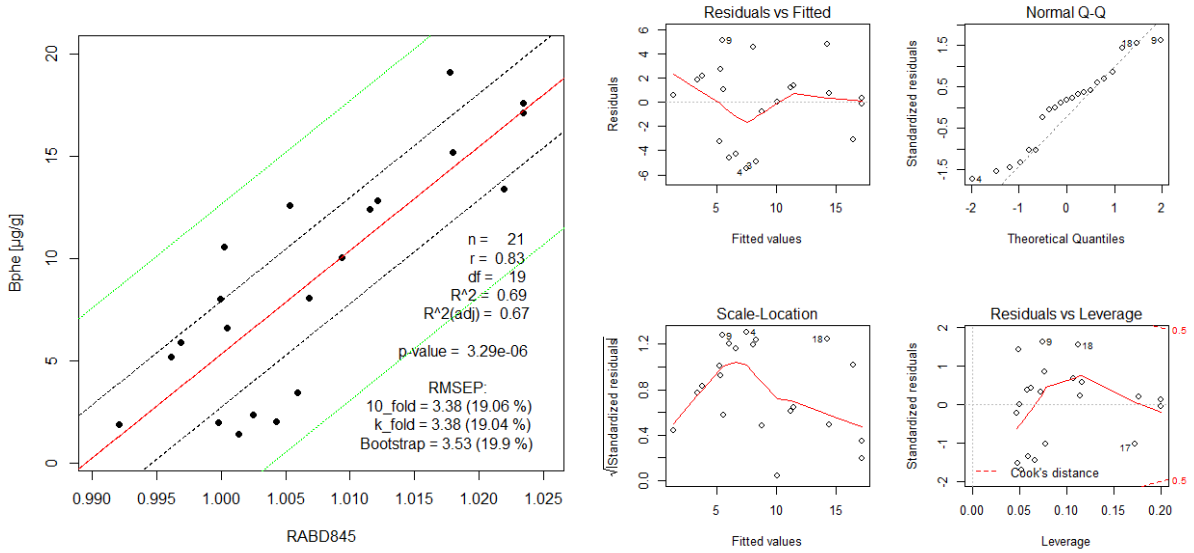

Fig. A 4: Bphe linear model results. Left panel: linear model, right panel: diagnostic plots for the validity of the residuals.

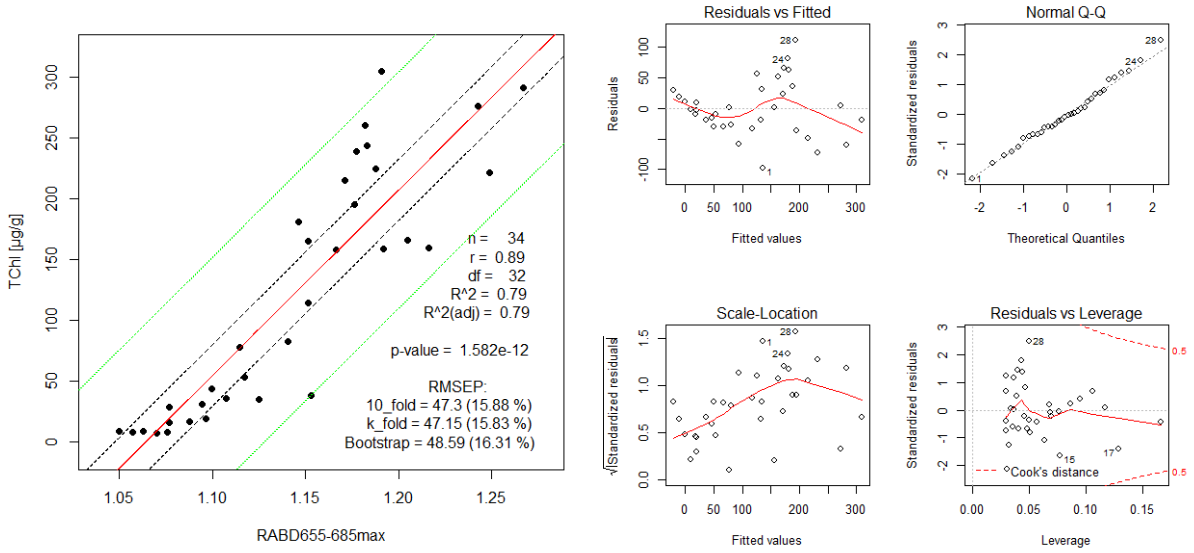

Fig. A 5: TChl linear model results. Left panel: linear model, right panel: diagnostic plots for the validity of the residuals.

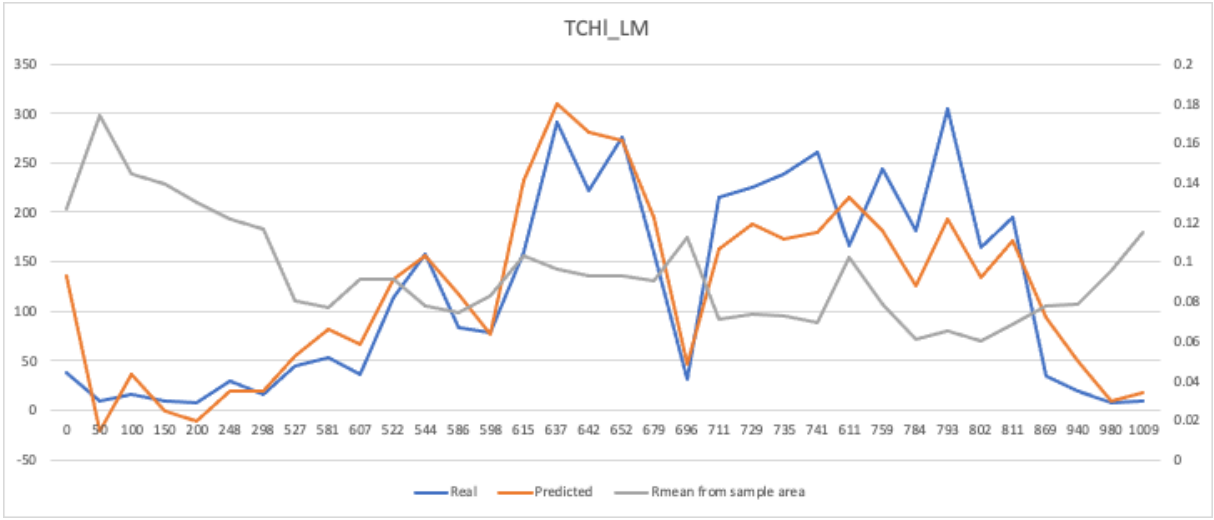

Fig. A 6: Linear model estimates compared to spectrophotometer measurements.

SCAM model results

The SCAM model was highly significant (R2adj. = 0.91). The following formula was used: Chlorins ~ s(RABD655685max, bs = "micx") + s(Rmean, bs = "mdcx"). The model had a GCV score of 1029.5, a scale estimate of 891.66 and used 34 sample points. The BFGS termination condition was 0.0006169623. P-values were highly significant ($p<0.01$). Further details in Fig. A 7. Model results were compared with spectrophotometer data (Fig. A 8). Note that the SCAM model does improve the results at a low Rmean compared to the linear regression model (Fig. A 6). However, the SCAM model does not perform better over the entire master depth (e.g. low values were estimated worse).

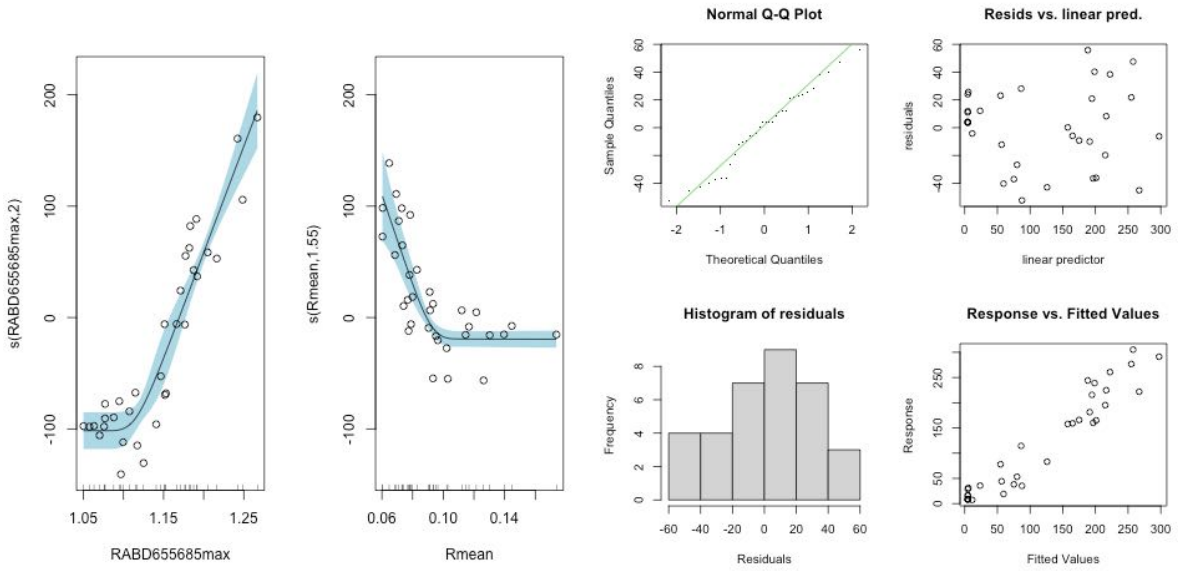

Fig. A 7: SCAM model results. Left panel: scam model. Right panel: diagnostic plots on residuals.

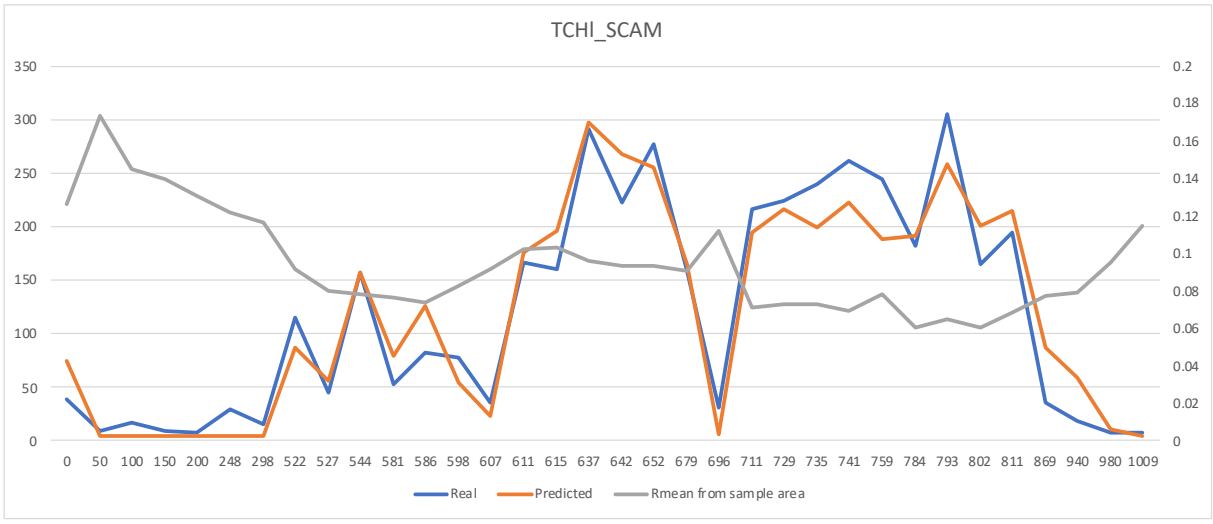

Fig. A 8: SCAM model estimates compared to spectrophotometer measurements.

E1 XRF - crack detection

Table A 8: Crack identification on XRF-scans.

Potential_cracks_coredepth	*Core*	*Crack class on optical images*	*Peak in Ar counts*
24	MZZ_A_1_2_A	0	0
35	MZZ_A_1_2_A	0	0
64	MZZ_A_1_2_A	0	0
71	MZZ_G_2_3_A	2	0
45.5	MZZ_F_2_3_A	1	0
52.5	MZZ_F_2_3_A	1	0
34	MZZ_F_3_4_W	1	0
67.5	MZZ_F_3_4_W	1	0
76.5	MZZ_F_3_4_W	0	0
13.5	MZZ_G_4_5_W	1	1
32	MZZ_G_4_5_W	2	1
49	MZZ_G_4_5_W	0	0
74	MZZ_F_5_6_A	2	1
82.5	MZZ_F_5_6_A	2	1
19.5	MZZ_C_7_5_8_5_A	0	1
45	MZZ_C_7_5_8_5_A	0	0
57	MZZ_C_7_5_8_5_A	0	0
79.5	MZZ_C_7_5_8_5_A	0	0
86.5	MZZ_C_7_5_8_5_A	0	1
10	MZZ_C_8_5_9_5_A	0	0
50	MZZ_C_8_5_9_5_A	0	0
54.5	MZZ_C_8_5_9_5_A	1	1
60	MZZ_C_8_5_9_5_A	1	0
71	MZZ_C_8_5_9_5_A	0	1
89	MZZ_C_8_5_9_5_A	0	1
32	MZZ_C_9_5_10_5_A	0	0
89	MZZ_C_10_5_11_5_A	0	0
27	MZZ_C_11_5_12_5_A	0	0
48	MZZ_C_11_5_12_5_A	0	0
51.5	MZZ_C_11_5_12_5_A	0	0

We classified cracks based on optical images (from SmartCIS and XRF) and Ar elemental counts (see chapter 3.2.4). In Table A 8 the column "crack class optical image" shows different numbers. Zero indicates cracks that are only visible in SmartCIS images acquired after XRF scanning, one designates thin cracks (< 1 mm) visible on the XRF optical image acquired directly before the scan, and two specifies thick cracks (> 1 mm) visible on the XRF optical image. The column "Peak in Ar counts" presents visible cracks that show an increase in Ar. Based on that classification we used the formula presented in chapter 3.2.4 to detect cracks. Cracks not fulfilling that argument were not influencing the XRF scan because they were eighter not in an area were the sensor measured or they were simply formed after the XRF scanning.

E2 XRF – influence of water content

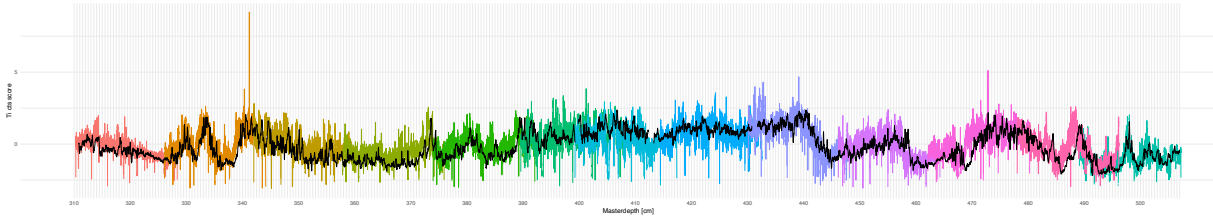

Fig. A 9: Ti scores from XRF (black) and µXRF data (colours) in the Bronze Age case-study section.

To check for the influence of water content (WC) we compared XRF scans on fresh sediment with µXRF scans on the resin blocks. The fresh sediment has a varying water content. This has been measured by Ramrath (1997) and covers, in the Bronze Age, nearly the entire spectra of WC variations in the sediments of Lago di Mezzano. On the other hand, the resin blocks contain no water as they were freeze dried before resin application. Fig. A 9 shows Ti scores (scaled Ti counts) from the XRF (fresh sediment) and µXRF scans (resin blocks). Both datasets are visually very similar. Hence, the influence of water content is negligible. The higher noise in the µXRF data is explained by its higher resolution and the shorter exposure time (see methods).

F1 Data – lake level

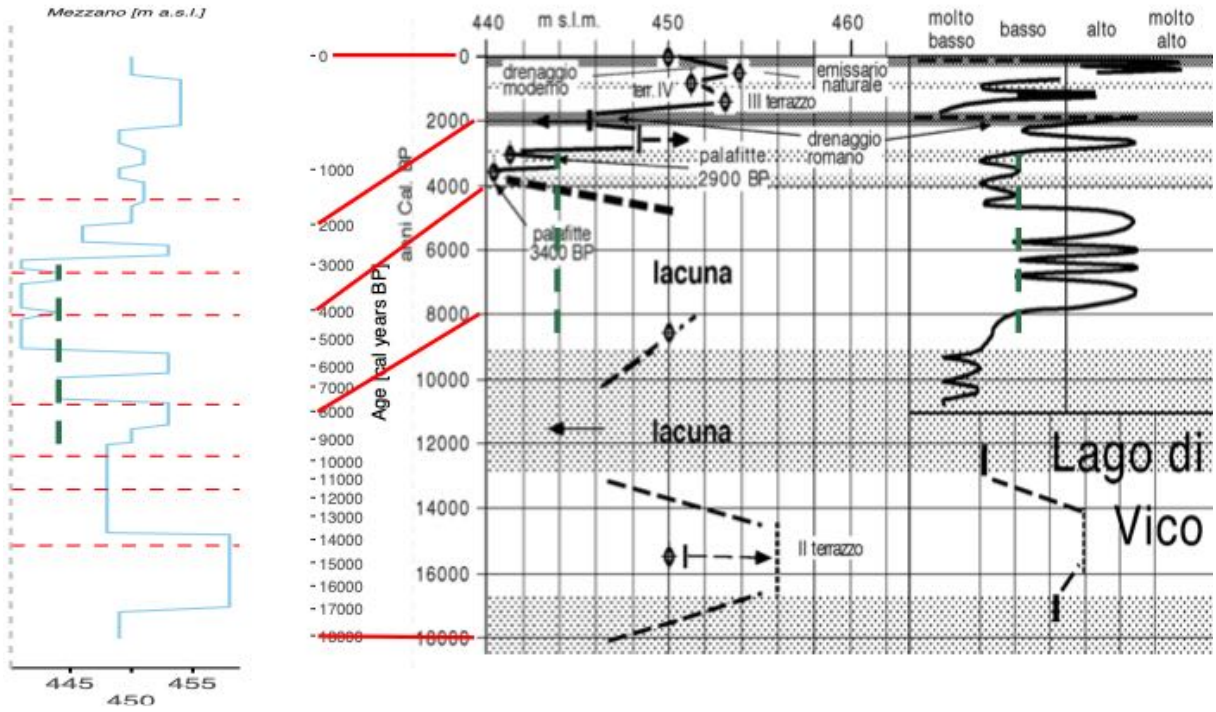

Fig. A 10: Compiled lake level record.

Fig. A 10 shows our compiled lake level record of Mezzano based on what is reported by Giraudi (2004) and Ramrath et al. (2000). Furthermore, we present the original plot of Giraudi on Mezzano and Lago di Fucino. At Mezzano gaps concerning the timings of lake level variations are obvious. We tried to fill some of these gaps with educated guesses based on the lake level record of Lago Fucino, which has a similar pattern, and on descriptions made by Ramrath et al. (2000). Also, in the section with the green, dashed line (Fig. A 10), low lake levels were just reported by Ramrath et al. (2000) without giving the lake level in meters a.s.l. Therefore, we assumed a similar pattern as in Lago Fucino. Timings match well with CONISS boundaries indicating that changes happened at that time.

F2 Data – pollen comparison

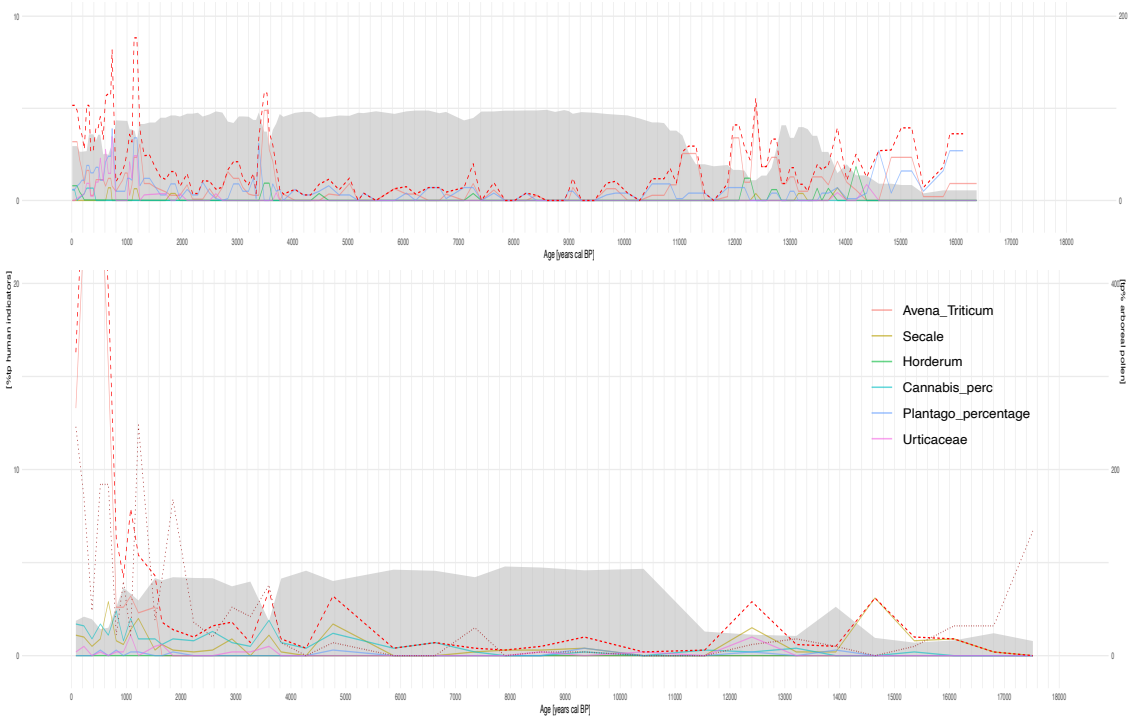

Fig. A 11: Overview pollen records from Giorgia Beffa (bottom panel) and Sadori (2018, upper panel). Grey area plot shows AP%. The AP% (respective to terrestrial pollen) are given on the right axis. The legend shows the colours and names of used taxa for the human indicator.

Both arboreal pollen percentage (AP%) profiles (Fig. A 11) show a similar behaviour. For the Pleistocene we can observe a low AP% in the Late Glacial, an increase in the Bølling–Allerød interstadial and again low AP% in the Younger Dryas. The Holocene has much higher AP%. In the Bronze Age we can observe in both datasets a clear impact of humans (human indicators) and a reduction in AP%. After a recovery, that impact increases in both profiles after around 1500 years BP. As the human indicator species do occur naturally, we only use them as an indicator since the Neolithic. There, we observe human induced reduction of beech (Giorgia, personal communication). Overall, both pollen records show the same trends and we are safe to use the higher resolution record of Sadori (2018).

F3 Data – Sadori-Ramrath age depth model

Table A 9: Sadori's (2018) age depth model with reference to Ramrath's (1997) depth

Depth Ramrath [cm]	***Age Sadori [years BP]***	***Source*** *(PAZ from Sadori, 2018)*
0	0	Sadori, 2018: Fig. 4
50	93	Sadori, 2018: Fig. 4
100	279	Sadori, 2018: Fig. 4
150	508	Sadori, 2018: Fig. 4
200	830	PAZ 1
250	1015	Sadori, 2018: Fig. 4
300	1473	Sadori, 2018: Fig. 4
312	1690	PAZ 2
350	1845	Sadori, 2018: Fig. 4
400	2216	Sadori, 2018: Fig. 4
450	2631	Sadori, 2018: Fig. 4
476	2990	PAZ 3
500	3038	Sadori, 2018: Fig. 4
550	3453	Sadori, 2018: Fig. 4
564	3710	PAZ 4
600	4061	Sadori, 2018: Fig. 4
650	5026	Sadori, 2018: Fig. 4
700	5991	Sadori, 2018: Fig. 4
732	6640	PAZ 5
750	6906	Sadori, 2018: Fig. 4
780	7480	PAZ 6
800	7650	Sadori, 2018: Fig. 4
850	8479	Sadori, 2018: Fig. 4
884	9180	PAZ 7
900	9358	Sadori, 2018: Fig. 4
950	10509	Sadori, 2018: Fig. 4
980	11440	PAZ 8
1000	11839	Sadori, 2018: Fig. 4
1052	13250	PAZ 9
1100	14530	PAZ 10
1150	14971	Sadori, 2018: Fig. 4
1200	15310	PAZ 11

G Neolithic case-study section

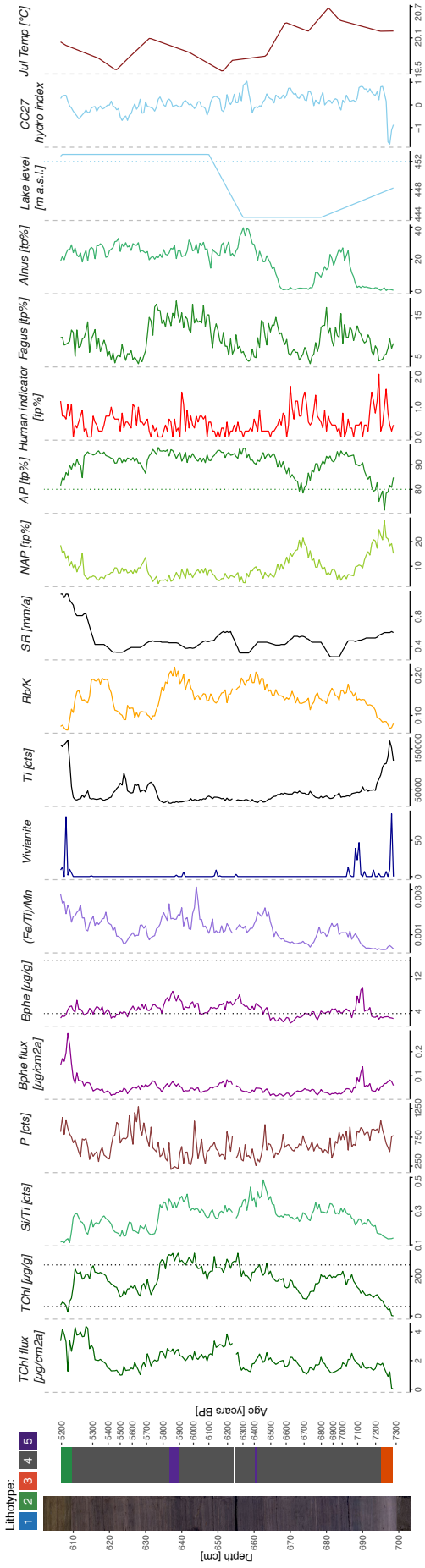

Fig. A 12: Evolution of proxies in the Neolithic case-study section.

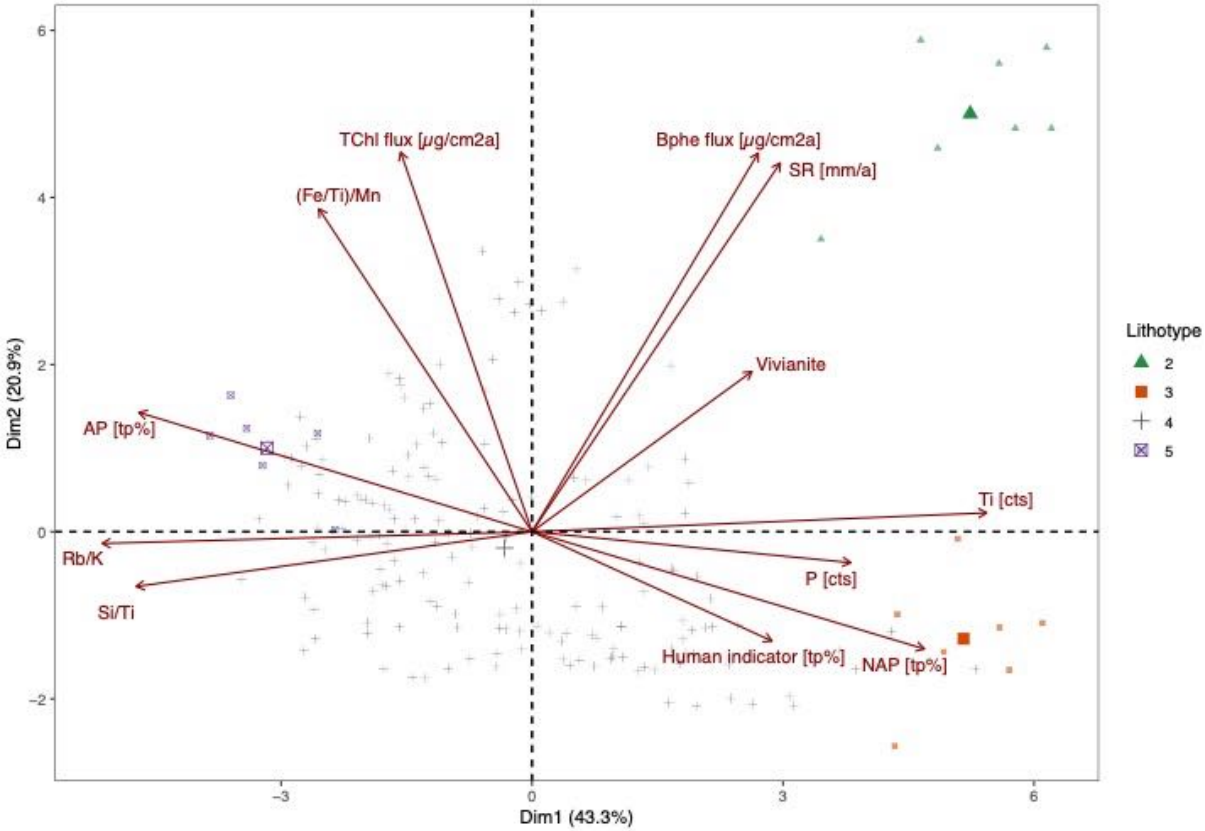

Fig. A 13: PCA Neolithic case-study section.

H1 Sediment description guidelines paleolimnology group

paleolim/06_LAB/Methods_SOPs/Catchment analysis and Initial core description/2017 Sediment description.docx

Lakes - background

The initial description of cores, and application of this classification system is based upon:

1) a general idea of the compositional variability of core material, which may hint at potential paleolimnological variability, influencing the choice of core material to study and sampling strategy;
2) the sedimentary composition of major lithologic units, which may assist multi-proxy projects to define what types of specialized studies can be done on which core sections; and
3) the recognition of potential sedimentary unconformities or bedding structures, such as turbidites, which can create spurious data points in specialized studies and must therefore guide core sampling strategy.

Results are best achieved by beginning any project with a multi-component, macro- and microscopic description and classification of the sediments (lithologic units).

The classification scheme

The sediment classification system employed at LRC relies on two primary types of observations:

1) the macroscopic structure of the sediment, i.e., sedimentary structures and textures (bedding features, texture, color) and
2) the identification of the major and minor components of the sediments, e.g., clay, carbonate mud, peat.

Core description

A principal task of the core lab sedimentologist is the bed-by-bed description of the sediments or sediment- ary rocks within the cores; this description is recorded on a Core Description form (template on server).

The sedimentologist first defines bedding on the basis of variations in sediment lithology, color, sedimentary structures, or other pertinent characteristics, and then proceeds to describe the four major characteristics of each bed: (1) lithology and color, (2) thickness and inclination, (3) sedimentary structures and bedding planes, and (4) degree of disturbance of the core stratigraphy by the coring process.

Macroscopic observation: bed color and texture

Bed color is determined by comparison with Munsell Soil Color Charts. Color should be determined as soon as the core is split and while still wet so that drying and oxidation do not alter its original color. Texture is noted by rubbing small quantities of sediment between the fingers or in the mouth. A rapid grain size estimator may be used to quantify sediment texture. Other aspects of sediment texture (e.g., roundness, sorting) may be estimated macroscopically in coarse-grained sediments or await microscopic smear slide study

Lamination / bed thicnkess and other features

Beds are defined as being .1 cm in thickness according to the following terms: **very thick bedded** (.100 cm), **thick bedded** (30–100 cm**), medium bedded** (10–30 cm thick), **thin bedded** (3–10 cm), and **very thin bedded** (1–3 cm) (McKee and Weir 1953**). Laminations** are less than 1 cm in thickness.

Sedimentary structures

These structures may be primary (formed during deposition) or secondary (formed after initial deposition of the sediments). Primary and secondary sedimentary structures may result from mechanical processes (e.g., graded bedding, water-escape structures) or may be biogenic (e.g., bioturbation structures, trace fossils) or chemical (e.g., salt) in origin.

Bedding planes

The nature of the bedding plane or contacts separating lithologic units holds important information con- cerning the

transition from under-to overlying beds (erosive vs. constant deposition). Bedding planes (contacts) may be described as **sharp** (change noted over less than 1 mm), **diffuse** (change noted over 1 mm – 1 cm) or **indistinct** (change noted over more than 1 cm). The contact between beds may be described as either planar or wavy to gradational, though this distinction may prove difficult in core material vs. outcrops.

Core disturbance

It is equally important to note evidence for disturbance of the core during the coring or drilling process.

Component-based analyses

The second major part of our sediment classification system involves the identity and estimated abundance of the various components of the sedimentary matrix. For rapid determination of sedimentary component abundance, we employ smear slide analysis. Description of sediment smear slides should be a routine analysis for sediment classification. Crystal morphologies and other optical properties allow the identification of different carbonate (aragonite versus calcite or dolomite), saline (gypsum and halite) and silicate (quartz, clay minerals, plagioclases, volcanic glass) minerals. Biogenic components (diatoms, organic matter, mollusk and so on) are also identified. The approximate percentages of the different components can be estimated. XRD analysis is often employed to identify uncommon minerals.

A composed-based sediment classification

Clastic sediments are composed of discrete grains of generally allocthonous (quartz grains, volcanic ash) origin deposited by physical processes of sedimentation (air fall, sub-aqueous currents).

Clastic sediment classification scheme

Clastic sediments are classified by designating a principal name describing the major textural component of the sediment (e.g., sand, silty clay; Figure 2) with the addition of major and minor modifiers to either describe less abundant components (e.g., diatomaceous clay) or to provide a more detailed description of the dominant components (e.g., vitric sand), or both.

H2 Extraction protocol for pigments (simplified for spectrophotometer)

Material and Instruments:

- Polypropylene centrifuge tube 50 mL (falcon tubes)
- Agate mortar and pestle
- Stainless steel spatula
- Glassware (i.e. glass pasteur, beakers, volumetric flask by 250 mL or 500 mL, cylinders, amber glass tubes) and glass wool
- Oven to bake glassware (i.e. glass pasteur, beakers, volumetric flask by 250 mL or 500 mL, cylinders, amber glass tubes) and glass wool
- Acetone (100%, HPLC grade)
- MQ
- Fume hood (for organic solvents)
- Aluminium foil
- Drying agents (DionexTM ASE TM Prep DE, DionexTM ASE TM Prep MAP)
- Oven to dry drying agents (max 50 degrees)
- Needles (to attach to the nirogen blow down system)
- Balances
- Small syringe (1 mL)
- Nitrogen
- Filter (0.2um Nylon Fisher Brand)
- Amber HPLC vials
- Vortex
- Sonication
- Centrifugation
- Glass columns (--> plastic piston)
- Ice bath
- Stands for holding the column
- Height-adjustable platform

Extraction step 1 (repeat until no colour, usually 3 times):

- Acetone (100 % HPLC grade)
- 2x 500mL glass bottles to store 100% Acetone
- Cylinder (100ml and 500ml)
- Glass wool
- Long glass Pasteur pipettes and silicon nipple
- Pipette (100-1000 µl) and blue tips
- Amber glass tubes, caps and septums (1st set)
- Vortex
- Ultrasonic bath
- Centrifuge
- Ice bath

Extraction step 3:

- Small amber HPLC vials
- Septum amber HPLC vials
- N_2 gas
- Acetone (100 % HPLC grade)
- Filter (0.2 µm, Nylon, Fisher Brand)
- Sample concentrator (i.e. nitrogen blow-down system)
- Heating plate
- Rack for amber vials

Preparation and Cleaning

Get 100% Acetone (HPLC grade)
Cleaning of amber glass tubes, beakers, cylinders, volumetric flasks

- Clean the glassware manually (brush) and put them in the washing machine
- Rinse them with MQ and Nanowater (3 times)
- Clean them with tech. acetone (3 times)
- Close them with aluminium foil (with tech. acetone cleaned)
- Bake them into the oven (292°C) over night or 12h

Cleaning of glass Pasteur pipettes and glass wool

- Put them in the oven over night (292°C) covered with Al foil

Cleaning of caps and membrane of amber glass tubes, needles of sample concentrator

- Rinse them with MQ and Nanowater
- Put them in a beaker filled with tech. acetone
- Sonificate 3 times
- Dry the materials in the clean oven

Dry agent

- Dry the dry agents in beakers covered with Al foil in the oven over night (50°C) and afterwards store it in a desiccator.

Prepare your working space

- Use the fume hood for organic solvents
- Clean the surface and cover it with acetone cleaned Al foil
- Put the ice bath in the upper corner of the fume hood

Samples

- 0.5 g of freeze dried and homogenized sediment (mortar and pestle, plus spatula) into 50mL falcon tubes (orange cap)
    - Use anti-static device to avoid static interference
    - Clean everything with technical acetone (spatula)
    - 0.25 g are also fine if not enough sediment available (only if the sediment is old 150 years)
    - LH used 1 g sediment because of very low Bphe concentrations, however that needs much more repetitions of step 1! Also I needed sometimes two amber vials to extract all pigments (2x 2mL Acetone)

* For reliable pigment data use relatively fresh sediment samples because pigments get degrade after long storage.

Pigment extraction

1. **Add 5ml of acetone (100%)** → repeat this step 3 times or more = until no colour visible in the extraction => up to 10 times (LH)
    - Vortex (~1min)
    - Sonication (~1min)
    - Centrifugation (10min/5000rpm)

    - Switch off the light whenever possible throughout the whole extraction procedure (especially in the fume hood)
    - Fill the 100% acetone into a clean beaker (don't pipette directly from the bottle)
    - Rinse the pipette first, before adding 5x 1ml of 100% acetone into the falcon tubes (take care that there are no bubbles in the pipette)
    - Vortex (~1min), Sonication (~1min), Centrifugation (10min/5000rpm) of the samples
    - Check if the supernatant is clear after centrifugation. If not, centrifuge it again or put some glass wool into the falcon tubes, press it a bit down. Normally, the glass wool is added in the second round of extraction. (Often not necessary at all)

- Remove the supernatant (greenish, yellowish, brownish) solvent carefully with the long glass pasteur pipette and transfer it into the labelled amber vials. All supernatant should be removed from the falcon tubes before adding 5 mL of acetone 100% again (second and third cycle)
- Store the amber vials with solvent in the ice bath, each vial can hold the respective glass Pasteur pipette. Cover the amber vials with Al-foil to provide shade and reduce Acetone evaporation.

*After this step the extract can be stored (-20°C) for a couple of days. For better pigment preservation we suggest to store the samples under nitrogen. Depending how many samples are extracted, it might make sense to first extract all samples with acetone 100% and then go on with the water removal from the supernatant and concentration steps.

3. Concentration and reconstitution of the solvent

- Use N_2 evaporator to blow down system
- Reconstitution with 2 mL of 100% acetone

- Set up the heating plate and the N_2 blow down system
- Use N_2 blow down system to preconcentrate the water-free supernatant extracts. Keep in mind to clean the needles before using this equipment
    - Place the amber vials containing the extracts on a rack on the heating plate (35°C) under the N_2 blow down system
    - Open the nitrogen stream (you should see a small flexion of the surface)
    - This step is finished when you have a dry crust of pigments in the amber tube (ca. after 30 min they start to dry out)
- Reconstitution and Filtration
    - Label the small HPLC vials and fill 100% acetone into a clean beaker.
    - Pipette 2 mL of 100% acetone into amber tube with the pigment crust using the 1000µl pipette. This step should be very precise. There should be no bubbles in the pipette. Otherwise use the balance and take note of the temperature
    - Check and homogenize the solvent with a glass Pasteur pipette
    - If some pigments are left (e.g. when very high concentrations or large samples => LH) you can use a second amber vial (b) with again 2mL Acetone. The concentrations of the pigments in the amber vials (a & b) can be summed up later.
    - Take a small syringe (1 mL) attach the filter (0.2um Nylon Fisher Brand) on it
    - Pipette directly with a glass pipette into the piston and pass the solvent through the filter into the small HPLC glass vials.

* To avoid the waste of N_2 gas, all places of a rack should be occupied with water-free extract samples. In addiction for a better pigment preservation, fill up the HPLC glass vials as much as you can in order to leave a very small head space.

Storage at -20°C until further analysis (maximal one month)

Sanchini, A., & Grosjean, M. (2020). Quantification of chlorophyll *a*, chlorophyll *b* and pheopigments *a* in lake sediments through deconvolution of bulk UV–VIS absorption spectra. Journal of paleolimnology. https://doi.org/10.1007/s10933-020-00135-z

H3 Spectrophotometer SOP for pigment analysis (proxy-to-proxy calibration)

paleolim/06_LAB/Methods_SOPs/Pigment analysis/lab protocols/SOP_Spectrophometer measurement_AS_GW 2021.docx

Material:

- Acetone 100% HPLC grade
- Different sizes of volumetric flasks (1ml, 5ml, 10ml, 25ml, 50, 100ml) – cleaned and baked
- Crimping tool for opening and closing small HPLC vials
- Pipettes and tips (blue (100-1000 µL) and red pipettes (50-250 µL))
- Long glass Pasteur pipettes and silicon nipple – cleaned and baked
- Beckers for acetone and waste – cleaned and baked
- Micro cuvettes and green caps (touch the cuvette only at the corners, check that no bubbles and particles are present inside cuvettes)
- Pigment extracts (please check the pigment extraction protocol)

Preparation and Cleaning: glassware

- Clean the glassware manually (brush) and put them in the washing machine
- Rinse them with MQ and Nanowater (3 times)
- Clean them with tech. acetone (3 times)
- Close them with aluminium foil (with tech. acetone cleaned)
- Bake them into the oven (292°C) over night or 12h

Measurement:

- Turn on the instrument and the PC wait 1 hour before to perform spectrophotometric analysis
- No password needed → enter
- Start UVProbe software (desktop)
- To connect the instrument with the PC press F4 and connect
- Set up the wavelength range from 900 to 350 (yellow button presents in the window bar; spectrum method), scan speed: fast, sampling interval 0.1 nm, scan mode: single-> press ok
- Pipette 400µl acetone 100% (HPLC grade) into cuvette to check if there is any contamination of the solvent (make sure that there are no bubbles in the tip of the pipette)-> this step is the blank
- Close the cuvette with the green cup
- Place the cuvette in the cell holder in the front. The V mark on the cuvette should be facing backwards.
- To make the autozero of the instrument, fill another cuvette with 400 µl acetone 100% (HPLC grade), close it and place it in the cell holder in the back (reference-side cell holder)-> press the button "baseline". After this step the absorption value shown by the instrument should be zero.
- The reference solvent in reference-side cell holder position remains for the whole measurement in the spectrophotometer.
- Make the autozero of the instrument, after each time that a sample extract is analysed.
- The sample extracts are diluted in such a way that the overall absorption is between between 0.2 and 1 abs (the reason is because limit of quantification of the instrument is linear in this range without the use of calibration curves).
- For example 1:10 (500µl sample extract in 5ml acetone)
    - Vortex the vial containing the sample extract
    - Pipette 2x 250ul into a 5ml flask and add acetone with a glass pasteur pipette up to the 5mL mark-> N.B. meniscus, is not flat; it is concave!!!
    - Mix the diluted sample with the glass pipette
    - Transfer 400 µl of the diluted sample with the small pipette into a cuvette
    - Close the cuvette with the green cap
    - Place the cuvette in the front cell holder
    - → start
- Once the analysis is finished a window rise where you can save the name of your file from the software. However, this step is not enough, and you have to resave the file pressing ->file->save as-> add the same name's file. Please make sure your file is saved properly. N.B. all this procedure is part of this article: Sanchini & Grosjean (2020)
- Calculate concentrations from absorption spectra

- (Must) Correct the absorption values in case you obtain absorption values below or above 0 between 720 and 900 nm in the way to scale the absorption values at around 0 abs in this range. If you have to quantify total carotenoids and chloropigments, and bacteriocloropigmnets are not present in your sample extract you can use the absorption values at 750 nm of wavelength to correct this. In presence of bacteriochloropigments, find a specific wavelength of absorption above 750 nm which you can use to scale the absorption values to zero.
- Calculate concentrations from the absorption spectra using the following formula:

$$c = A_\lambda / (\alpha_\lambda \cdot b)$$

Where b is the wide of the cuvettes (in our case 1 cm), A_λ is absorbance measured at a specific wavelength, α_λ is the specific molar extinction coefficient equal to 80.77×10^{-3} L cm^{-1} mg^{-1} for chloropigments *a* at 666 nm (Jeffrey and Humphrey, 1975) and 52.855×10^{-3} L cm^{-1} mg^{-1} for bacteriopheophytin *a* at 750 nm (Fiedor et al., 2002).

- The total carotenoids are expressed as mg TC per gram of organic matter (g_{LOI}), according to the following formula (Züllig 1981):

$$\mathrm{TC} = \frac{(E_{450\,\mathrm{nm}} - 0.8E_{665\,\mathrm{nm}})V \cdot 10}{E^{1\%}_{1\,\mathrm{cm}} \cdot \mathrm{gLOI}}$$

where E is the measured optical density in a 1 cm path-length cuvette at 450 and 665 nm, both corrected by optical density at 750 nm, V is volume of solution (mL), E1% 1 cm is the average extinction coefficient of a 1% solution of extract of sediment (by weight) of the carotenoids with a path length of 1 cm layer equal to 2,250, (Züllig 1981; Leavitt and Hodgson 2001), E_{450nm} is the main absorption of carotenoids in the visible light portion of pigment extractions, E_{665nm} is the approximate correction of absorption of chlorophylls and chlorophyll derivatives at 665 nm, and g LOI is the loss-on-ignition equivalent content of the wet sediment calculated
using the water content and LOI g dry weight.

Fiedor, J., Fiedor, L., Kammhuber, N., Scherz, A., Scheer, H., 2002. Photodynamics of the Bacteriochlorophyll–Carotenoid System. 2. Influence of Central Metal, Solvent and β-Carotene on Photobleaching of Bacteriochlorophyll Derivatives. Photochem. Photobiol. https://doi.org/10.1562/0031-8655(2002)076<0145:potbcs>2.0.co;2

Jeffrey, S.W., Humphrey, G.F., 1975. New spectrophotometric equations for determining chlorophylls a, b, c1 and c2 in higher plants, algae and natural phytoplankton. Biochem. und Physiol. der Pflanz. https://doi.org/10.1016/s0015-3796(17)30778-3

Leavitt PR, Hodgson DA (2001) Sedimentary pigments. In: Smol JP, Birks HJB, Last WM (eds) Tracking environmental change using lake sediments, vol 3: terrestrial, algal, and siliceous indicators. Kluwer, Dordrecht, pp 295–325

Sanchini, A., & Grosjean, M. (2020). Quantification of chlorophyll a, chlorophyll b and pheopigments a in lake sediments through deconvolution of bulk UV–VIS absorption spectra. Journal of paleolimnology. https://doi.org/10.1007/s10933-020-00135-z

Züllig H (1981) On the role of carotenoids stratigraphy in lake sediments for detecting past developments of phytoplankton. Limnol Oceanogr 26:970–976

Declaration of consent

on the basis of Article 30 of the RSL Phil.-nat. 18

Name/First Name: Hächler, Luc

Registration Number: 15-109-812

Study program: Master of climate sciences

Bachelor ☐ Master ☑ Dissertation ☐

Title of the thesis: High-resolution record of primary productivity and anoxia in the context of the environmental history of Lago di Mezzano, Central Italy, since the Late Glacial

Supervisor: Prof. Dr Martin Grosjean

I declare herewith that this thesis is my own work and that I have not used any sources other than those stated. I have indicated the adoption of quotations as well as thoughts taken from other authors as such in the thesis. I am aware that the Senate pursuant to Article 36 paragraph 1 litera r of the University Act of 5 September, 1996 is authorized to revoke the title awarded on the basis of this thesis.

For the purposes of evaluation and verification of compliance with the declaration of originality and the regulations governing plagiarism, I hereby grant the University of Bern the right to process my personal data and to perform the acts of use this requires, in particular, to reproduce the written thesis and to store it permanently in a database, and to use said database, or to make said database available, to enable comparison with future theses submitted by others.

Bern, 18.11.2021

Place/Date

Signature